AALBORG UNIVERSITET

STUDENTERRAPPORT

JOINT CLUTTER AND TARGET TRACKING FOR MULTI-RADAR SYSTEMS: A NOVEL DISTRIBUTED BAYESIAN ALGORITHM

May 28, 2025

Astrid Holm Filtenborg Kitchen
Marie Saugstrup Jensen
Mikkel Sebastian Lundsgaard Brøndt

Master's Thesis
Mathematical Engineering
Aalborg University

Title:

Joint Clutter and Target Tracking for Multi-Radar Systems: A Novel Distributed Bayesian Algorithm

Theme:

Radar Signal Processing

Project:

Master's Thesis

Project Period:

Spring Semester 2025

Project Group:

MT10-02

Participants:

Astrid Holm Filtenborg Kitchen
Marie Saugstrup Jensen
Mikkel Sebastian Lundsgaard Brøndt

Supervisors:

Anders Malthe Westerkam
Troels Pedersen
Christophe Ange Napoléon Biscio

Total number of pages: 84
Of which is appendix: 3

Date of completion: May 28, 2025

Abstract:

Drones are an increasing concern in both public and private sectors due to privacy and safety issues. They are difficult to track due to their small size, low radar cross-section, slow speed, and high manoeuvrability. This project focuses on tracking a target and clutter using multiple 2×4 monostatic multiple-input and multiple-output frequency modulated continuous wave radars. Therefore, the signal model of the radar system at hand and the mean field approximation has been presented. The mean field approximation is used for approximating an intractable posterior probability distribution using surrogate functions. Bayesian networks are used for the visualisation of this and in the discussion of the system setup. An experiment has been conducted on consumer-grade hardware using data simulated in MATLAB. A clutter tracking algorithm and a target tracking algorithm has been combined to create a multiple radar clutter and target Bayesian localisation and tracking algorithm which operates in Cartesian coordinates. This leads to an estimated trajectory of a target manoeuvring in a clutter environment, with low SINR. By simulating different tracks, it seems likely that the algorithm works well in a low SINR setting.

Preface

This project is written in the period from February to May 2025 by the tenth semester group MT10-02, studying Mathematical Engineering at Aalborg University. The focus of this project is centred around joint tracking and localisation of a drone and clutter using multiple monostatic MIMO FMCW radars.
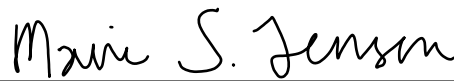
Note that all figures, graphs, etc. are produced by the group using MATLAB, `Python`, the TikZ package in LaTeX, or hand-drawn in Microsoft OneNote, unless otherwise stated. Furthermore, all references in this project are given by the Harvard method and will be placed in the beginning of each chapter or where they are used. If the cite is placed behind a period, it refers to the previous paragraph.

It is assumed that the reader of this project has an understanding of the topics studied on the bachelor of Science in Mathematical Engineering and the first three semesters of the master in Mathematical Engineering.

The group would like to thank supervisors Ph.D. student Anders Westerkam, Associate Professor Troels Pedersen, and Associate Professor Christophe Biscio for their invaluable guidance and endless patience. A further thanks to supervisor Anders Westerkam for providing us with a MATLAB file used for simulations.

Astrid Holm Filtenborg Kitchen
akitch20@student.aau.dk

Marie Saugstrup Jensen
marije19@student.aau.dk

Mikkel Sebastian Lundsgaard Brøndt
mbrand20@student.aau.dk

Abbreviations

If an abbreviation is in plural, there is added "s" at the end when the abbreviation consists of upper-case letters and " 's" if the abbreviation consists of lower-case letters.

Abbreviation	Meaning
FOV	Field of view
RCS	Radar cross section
MIMO	Multiple-input multiple-output
BLaT	Bayesian localisation and tracking
MRBLaT	Multiple radar Bayesian localisation and tracking
MRCaTBLaT	Multiple radar clutter and target Bayesian localisation and tracking
FMCW	Frequency modulated continuous wave
SNR	Signal-to-noise ratio
SINR	Signal-to-interference-plus-noise ratio
IF	Intermediate frequency
FDM	Frequency division multiplexing
TDM	Time division multiplexing
KL	Kullback-Leibler
pdf	Probability density function
CF1T	Clutter-free environment with one target
C0T	Clutter environment with no target
C1T	Clutter environment with one target
DFT	Discrete Fourier transform
FFT	Fast Fourier transform

Table 1. List of abbreviations used in the project.

Nomenclature

Symbol	Meaning
P_r	Power of received signal
P_I	Power of interference
P_N	Average noise power
λ	Wavelength
τ	Two-way time delay
r	Range
θ	Angle
α	Path loss
c	Speed of light
N_T	Number of transmitters
N_R	Number of receivers
m	Transmitter
j	Receiver
k	Radar
$\mathcal{X}^{(m,k)}(t)$	Emitted signal from the mth transmitter on radar k
$u^{(m,k)}(t)$	Complex baseband signal from the mth transmitter on radar k
ω_c	Angular carrier frequency
f_c	Carrier frequency
$\mathcal{Y}^{(j,k)}(t)$	Received signal on the jth transmitter on radar k
$s_{n,\text{target}}^{(j,k)}(t)$	Target signal
$s_{n,\text{clutter}}^{(j,k)}(t)$	Clutter signal
$w_t^{(j,k)}(t)$	Noise unrelated to the radar signal
$z^{(m,j,k)}$	Match filtered signal in the time domain
$Z^{(m,j,k)}$	Match filtered signal in the frequency domain
$\boldsymbol{Z}_n^{(k)}$	Vectorised match filtered signal in the frequency domain
$\boldsymbol{S}_n^{(k)}$	Vectorised match filtered target signal in the frequency domain
$\boldsymbol{M}^{(k)}\boldsymbol{\Gamma}_n^{(k)}$	Vectorised match filtered clutter signal in the frequency domain

Table 2. List of important symbols used in the project.

Symbol	Meaning
$\boldsymbol{W}_n^{(k)}$	Vectorised noise unrelated to the radar signal
$*$	Complex conjugate
$\boldsymbol{\phi}$	Kinematic parameters
$\boldsymbol{\Gamma}$	Vectorised expansion coefficients for the clutter field
$\boldsymbol{\mu}_C$	Mean of clutter field
$\boldsymbol{\Lambda}_C$	Precision of clutter field
$\boldsymbol{\Lambda}_a$	Precision of acceleration
$\hat{\cdot}$	Estimate
$\bar{\cdot}$	Mean
$\bar{\bar{\cdot}}$	Variance
ε	Message
$\gamma^{(l)}$	Expansion coefficients
$\psi^{(l)}$	Deterministic basis functions
$\langle \cdot, \cdot \rangle$	Inner product
δ	Kronecker delta function
N_B	Number of retained basis functions
Ψ	Complete set of basis functions
Ψ_{N_B}	Subset of basis functions containing N_B basis functions
E_{N_B}	Error between two clutter fields
$C_n^{(k)}$	Clutter field
$\mathrm{D_{KL}}$	Kullback-Leibler divergence
κ	Scaling factor
σ_w^2	Variation of noise
A	Steering matrix
$(\cdot)_{0:n}$	$(\cdot)_0, (\cdot)_1, \ldots, (\cdot)_n$

Table 3. List of important symbols used in the project.

Contents

Introduction to the Problem 1

Drones are a versatile and accessible tool, due to their wide range of sizes and use cases. They have been employed in many different industries, including law enforcement, military, photography, and agriculture. In recent years, drones have become more accessible to the public, leading to a significant increase in private ownership and their presence in both public and private spaces. In Denmark alone, 20 000 drones are being sold each year [Thaysen, 2023].

Due to the increasing number of drones in active use, it has become necessary to tighten the restrictions concerning drones and their fly zones [Trafikstyrelsen, 2023a]. In Denmark, it is illegal to operate a drone within 2 km to 5 km of an airport no matter the intentions [Trafikstyrelsen, 2023b]. These restrictions were implemented after multiple instances in which airports were forced to shut down due to drones operating near runways [Døssing, 2025b; Witten, 2024]. Illegal drone flights in air routes are a global problem, having led to rerouted landings, delays, flight groundings, and airport closures [Lu et al., 2021, p. 1].

Despite restrictions, a record high number of drone flights near Danish airports occurred in 2024, as shown in Figure 1.1, with the number of incidents more than tripled from the year before [Døssing, 2025a]. As the number of incidents continues to rise, airport security systems must be able to detect and localise unauthorised drone activity, since an undetected drone can have fatal consequences [Lu et al., 2021, p. 11]. For small areas, manual observations may suffice, but several problems can arise due to poor visibility caused by weather conditions and darkness. Furthermore, manual observation is not ideal for bigger areas, such as airports, due to the high labour and resource costs.

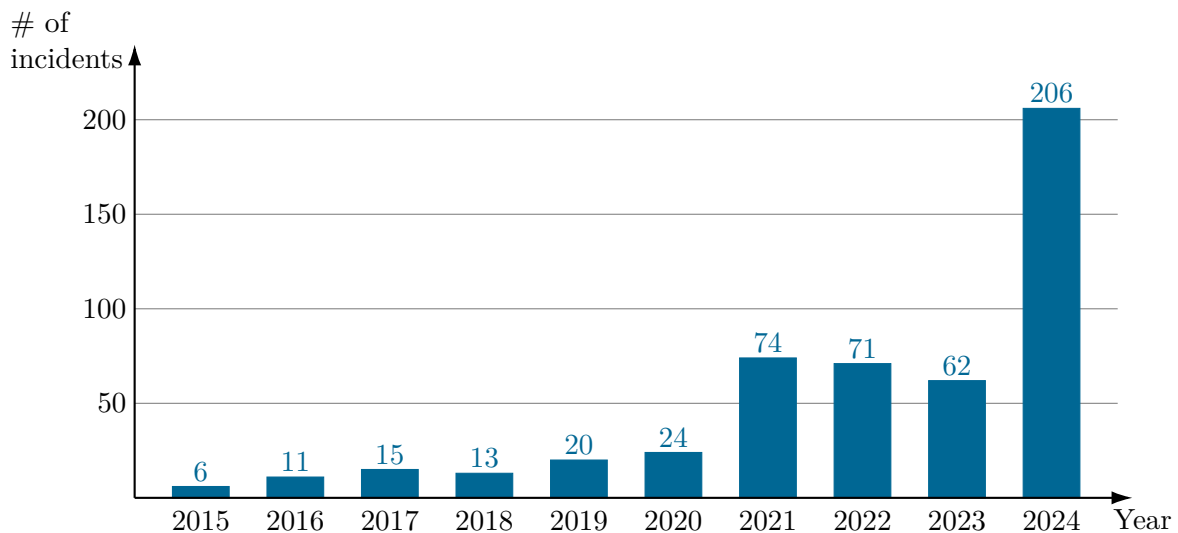There is a wide variety of drone detection and tracking methods relying on sensors such

Figure 1.1. Number of drone flights near Danish airports through the years. Data from [Døssing, 2025a].

as radars or cameras. Radars are ideal for detection and tracking, as they operate in all-day, all-weather conditions. The fundamental concept of radar involves a transmitter emitting an electromagnetic wave that scatters upon objects in its field-of-view (FOV). The scattered waves reflect back and are captured by a receiver, where they induce a measurable signal. This concept is depicted in Figure 1.2. Reflections from objects other than the drone interfere with the desired signal, where these unwanted reflections are referred to as clutter signals. The clutter signals are represented as grey dashed lines in Figure 1.2. Apart from the reflected waves, a noise signal is added at the receiving end, arising primarily from thermal noise. Consequently, the received signal $y(t)$ is a sum of the clutter signal $c(t)$, the target signal from the drone $s(t)$ and the noise signal $w(t)$ from the receiver:

$$y(t) = s(t) + c(t) + w(t). \tag{1.1}$$

In perspective to tracking a drone using radars, the clutter and noise signals can mask the signal from the drone, resulting in unreliable tracking, false detections, and missed detections. [Kingsley and Quegan, 1992, pp. 1, 38, 40, 63]

Drones are generally difficult to track using radars due to their low radar cross section (RCS) and high manoeuvrability. Multiple-input multiple-output (MIMO) radars have proved to overcome some of these challenges as they can obtain continuous observations within the whole FOV with a fine angular resolution [Grove, 2022, p. 3]. Several papers have presented their work on how to enhance tracking performance in low SNR conditions using MIMO radars. In [Huang et al., 2023], a sequential Monte Carlo method was presented, jointly detecting and tracking a target with constant velocity using a 4D MIMO radar. For localisation and tracking in a noncoherent MIMO radar system, [Niu et al., 2012] derived the maximum-likelihood estimate for the target location and velocity. In [Westerkam et al., 2023], a MIMO radar was utilised along with a Bayesian localisation and tracking (BLaT) algorithm to effectively track and localise a small RCS target with high manoeuvrability. We have expanded upon this algorithm in [Kitchen et al., 2025], developing a distributed algorithm that operates on multiple communicating radars.
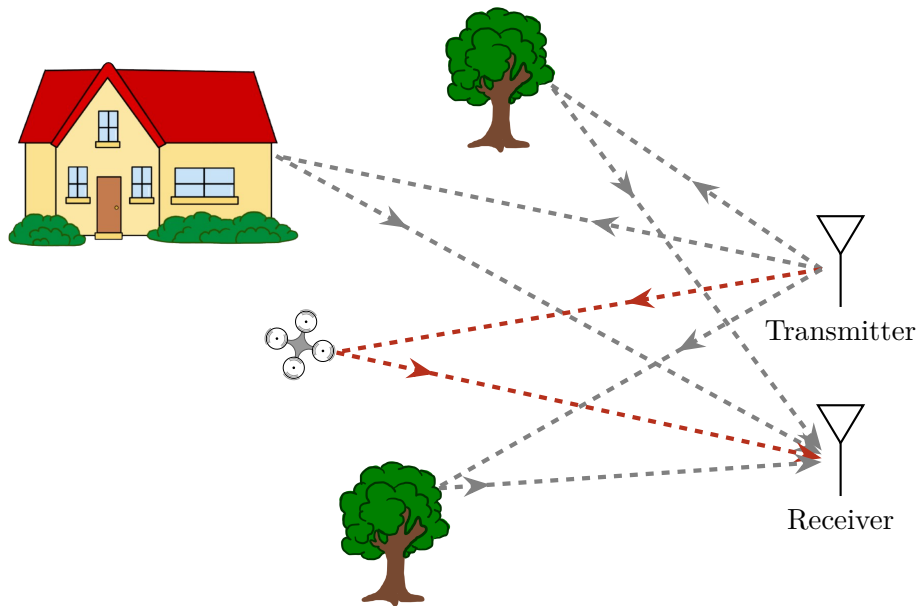

Figure 1.2. Fundamental concept of a radar, showing how a transmitted signal reflects on objects before being received. The red dashed line represents the desired signal while the grey dashed lines represents the clutter signals.

This variant of the algorithm is called multiple radar BLaT (MRBLaT). Both papers are able to track and localise a small RCS target in low SNR conditions. They evaluate their algorithms through simulations conducted in clutter-free environments with one target present. However, in a real-world setting, clutter signals are nearly always present with reflections arising from hills, buildings, and vegetation [Kingsley and Quegan, 1992, p. 38]. Thus, it is of great interest to model and track clutter.

Clutter can be modelled and tracked with various methods depending on the application and it is often tailored to the clutter type. A key distinction is made between sea clutter and ground clutter [Kingsley and Quegan, 1992, pp. 106-107]. This project focuses on ground clutter, as it aligns with the scenario of drone tracking in an airport environment. The characteristics of ground-clutter signals vary widely due to the diversity of ground clutter objects which include plants, trees, bare ground, rocks, buildings, other human-made structures, and ground snow [Hubbert et al., 2009].

As the clutter within the FOV changes over time, it is common to model it using a stochastic process, where each resolution cell is assigned a reflectivity drawn from a specific distribution. The choice of distribution for a specific circumstance relies on empirical distributions and physical reasoning [Kingsley and Quegan, 1992, p. 106]. In the Gamma model [Barton, 1985], the parameters of the distribution are derived from measurements of similar terrain along with the grazing angle for the area under surveillance. This approach requires prior knowledge of the area within the FOV. In [Westerkam and Pedersen, 2025], the clutter is modelled as a random field defined on a set of orthonormal separable basis functions. This enables clutter tracking by using message passing on a Bayesian network to learn the parameters of the random field. An advantage of this method is that it provides a general framework which does not make assumptions about the specific type of clutter present in the FOV.

Typically, tracking algorithms are tested in clutter environments by modelling clutter and incorporating it as noise or interference in simulations without explicitly tracking the clutter [Barton, 1985; Capraro et al., 2007; Musicki and La Scala, 2008]. Instead, we aim to implement the algorithm in [Westerkam and Pedersen, 2025] and combine it with the MRBLaT algorithm to propose a multiple radar clutter and target Bayesian localisation and tracking (MRCaTBLaT) algorithm.

1.1 Problem Statement

How can MRBLaT be expanded to take clutter into account? How does a combined clutter and tracking algorithm perform?

1.1.1 Scope of the Problem

The scope of the problem is restricted by a set of assumptions that limit the boundaries of the scenario under consideration. These assumptions enables an initial performance evaluation of the method under controlled conditions. The assumptions are as follows:

Two-Dimensional Setting
A two-dimensional setting is considered, with the radars detecting signals along the x- and y-axes. This is depicted in Figure 1.3.

(a) Example of a clutter environment observed by a radar. The red line indicates the plane that will be modelled.

(b) Clutter environment modelled as a two-dimensional plane.
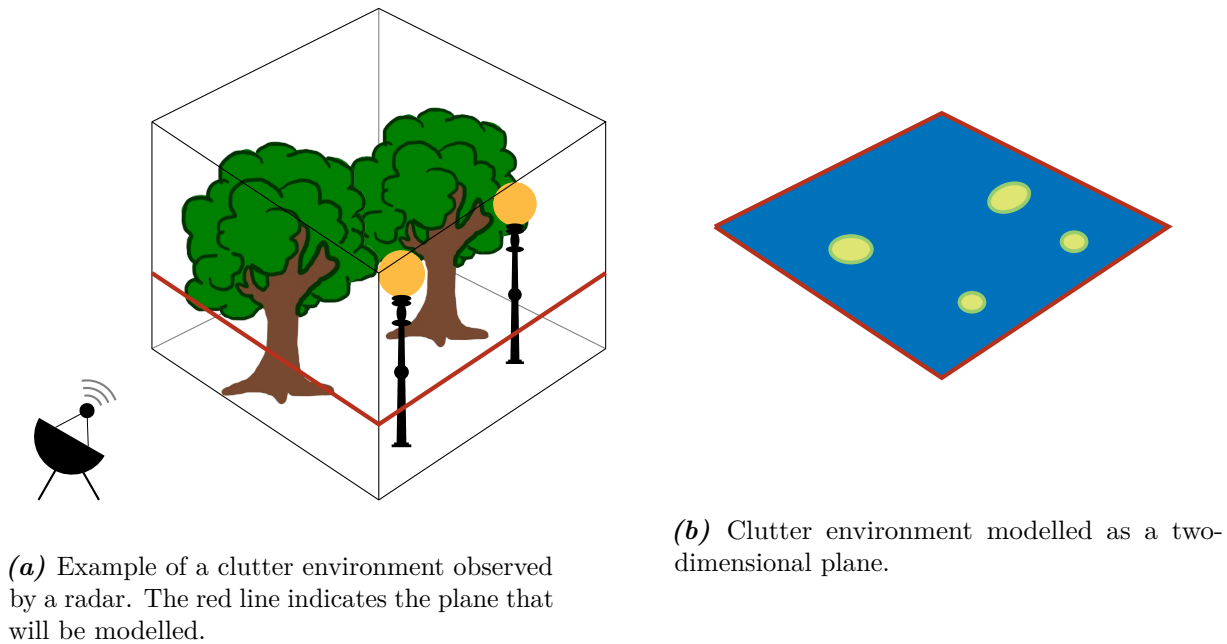
Figure 1.3. Visualisation of two-dimensional setting assumption.

Scattering Environment
The clutter signals are assumed to be from point clutter, that is clutter signals from individual reflective surfaces such as trees, buildings, and birds. It is assumed that at most one target is present in the environment and that it can be modelled as a point target. Additionally, only single-bounce reflections are considered, meaning the signals reflect off objects only once.

Monostatic MIMO Radars
It is assumed that all radars are monostatic MIMO radars, where the transmitted signal from a radar is only collected by the receivers on the radar it originated from. Additionally, it is assumed that the radars do not interfere with each other. It is assumed that the elements of the radar system are placed close enough such that the received signals are identical up to a small time delay, also assuming the target is in the far-field.

No Doppler Information
The objects are assumed to be slow moving, allowing the "stop-and-hop" approximation to be used. As a result, velocity effects are neglected and no Doppler information is available.

Target
It is assumed that the target is high-manoeuvring and has a small RCS to mimic a drone. Furthermore, it is modelled as a single reflected signal. It is assumed that only one target is present.

1.2   Structure of the Report

The remainder of the report is structured as follows:

Chapter 2 - Radar Principles introduces basic radar principles for MIMO FMCW radars. It focuses on the structure of transmitted and received signals, which forms the basis for developing the signal model for a radar.

Chapter 3 - Signal Model presents the signal model for the received signal of a MIMO FMCW radar for both the target signal and the clutter signal, which will be used to simulate data. As the clutter field is modelled as a random field, the chapter also includes an introduction of random fields and how to represent the field using orthogonal expansions.

Chapter 4 - Estimation of Signal Model Parameters derives how the parameters of the signal model are estimated using variational message passing. Thus, the chapter starts with an introduction to variational message passing using the mean field approach. The MRCaTBLaT algorithm is presented in the end of the chapter.

Chapter 5 - Prototype Implementation of Algorithm provides insight into how the algorithm is implemented and how the simulation setup is implemented in order to evaluate the performance of the algorithm.

Chapter 6 - Target and Clutter Tracking using Bayesian Inference presents the results from the simulations and evaluates the MRCaTBLaT algorithm through a Monte Carlo Simulation.

Chapter 7 and 8 - Discussion and Conclusion discusses the results from Chapter 6 and at last, conclusions are drawn in Chapter 8.

Radar Principles 2

In this chapter, based on [Kingsley and Quegan, 1992, pp. 11-13], the radar equation is presented first, followed by an introduction to MIMO FMCW radars.

Target detection is fundamentally limited by the strength of the received target signal, quantified by the signal-to-interference-plus-noise ratio (SINR). To this end, the radar equation is used to calculate the power of the received target signal P_r. As the transmitted signal travels through space, the power density is attenuated according to the inverse square law, which is dependent on the distance the signal travels. The radar equation for a single point target is given as

$$P_r = \frac{P_t G_t G_r \rho \lambda^2 L_s}{(4\pi)^3 r^4}, \tag{2.1}$$

where P_t is the power of the transmitted signal, G_t and G_r is the gain of the transmitter and receiver antennas, respectively, ρ is the RCS of the target, λ is the wavelength of the transmitted signal, L_s is the loss factor, and r is the range to the target. The SINR is defined as the power of the received target signal divided by the sum of the interference power and the power of the noise at the receiver:

$$\text{SINR} = \frac{P_r}{P_I + P_N} = \frac{P_t G_t G_r \rho \lambda^2 L_s}{(4\pi)^3 r^4 (P_I + P_N)}, \tag{2.2}$$

where P_I is the interference power and P_N is the average noise power. If there is no interference present in the signal, then the SINR reduces to the SNR given as

$$\text{SNR} = \frac{P_r}{P_N} = \frac{P_t G_t G_r \rho \lambda^2 L_s}{(4\pi)^3 r^4 P_N}. \tag{2.3}$$

The reduction in signal strength as it travels from the transmitter to the receiver is captured by the path loss α. The power path loss is defined as the ratio between the received and transmitted power:

$$\alpha_P = \frac{P_r}{P_t} = \frac{G_t G_r \rho \lambda^2 L_s}{(4\pi)^3 r^4}. \tag{2.4}$$

The amplitude path loss is defined as

$$\alpha_A = \sqrt{\alpha_P}. \tag{2.5}$$

2.1 MIMO Frequency Modulated Continuous Wave Radar

This section is based on [Klauder et al., 1960], [Jankiraman, 2018, Section 2], [Richards et al., 2010, p. 395], [Kingsley and Guerci, 2022, p. 193], [Brooker et al., 2005], [Steer, 2019, p. 187], and [Grove, 2022, p. 43, 57].

A MIMO radar consists of multiple transmitting and receiving antennas to increase the level of information. It transmits separate signals from each transmitter, and the received signals from the multiple receivers are processed together. This creates a virtual array consisting of $N_T N_R$ virtual channels, where N_T is the number of transmitter and N_R is the number of receivers. In a MIMO radar, the elements of the radar system are placed close enough such that the received signals are identical up to a small time delay, assuming the target is in the far-field. Figure 2.1a shows the MIMO principle and Figure 2.1b shows how the positions of the virtual channels are determined by the location of the physical channels.

An FMCW radar continuously transmits an electromagnetic wave with a frequency that changes over time within a given bandwidth. One of the simplest signal patterns is a sawtooth function which consists of chirps. Figure 2.2 shows the frequency and amplitude of a chirp. A chirp is a sinusoid where the frequency increases linearly with time, and it is characterised by a start frequency f_c, bandwidth B_c, and duration T_c. The slope of the chirp is defined as $S = B_c/T_c$. Thus, the instantaneous frequency of the transmitted baseband chirp is expressed as:

$$f(t) = St \quad \Leftrightarrow \quad \omega(t) = 2\pi St, \tag{2.6}$$

where ω is the angular frequency. Given that $\omega(t) = \frac{\mathrm{d}\varphi(t)}{\mathrm{d}t}$, it follows that

$$\varphi(t) = \int 2\pi St \, \mathrm{d}t \tag{2.7}$$

$$= \pi St^2 + \varphi_0, \tag{2.8}$$

where φ is the phase. This implies that the instantaneous amplitude of the chirp including the

(a) Side-view.   *(b)* Top-view.
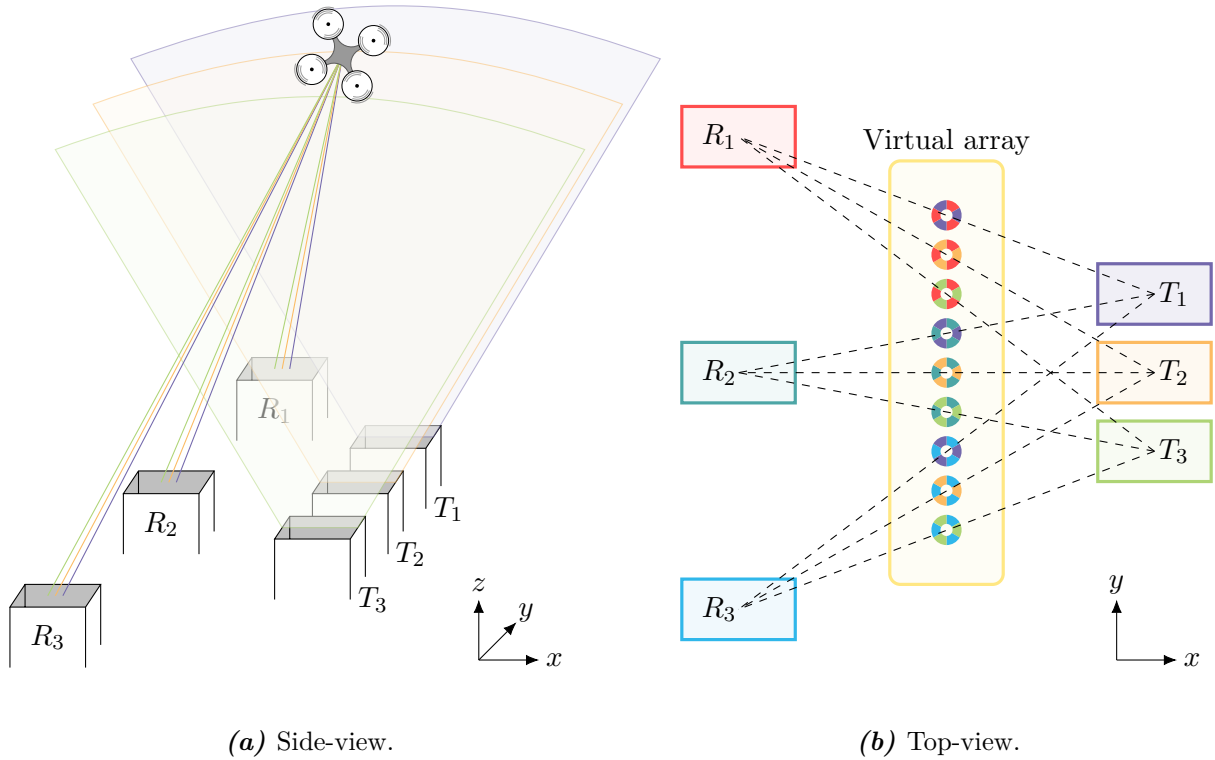
Figure 2.1. The MIMO principle showing the physical and virtual channel positions when assuming the target is in the far-field. The colours indicate each transmit and receive channel and their combination.

(a) Frequency-time plot.   **(b)** Amplitude-time plot.
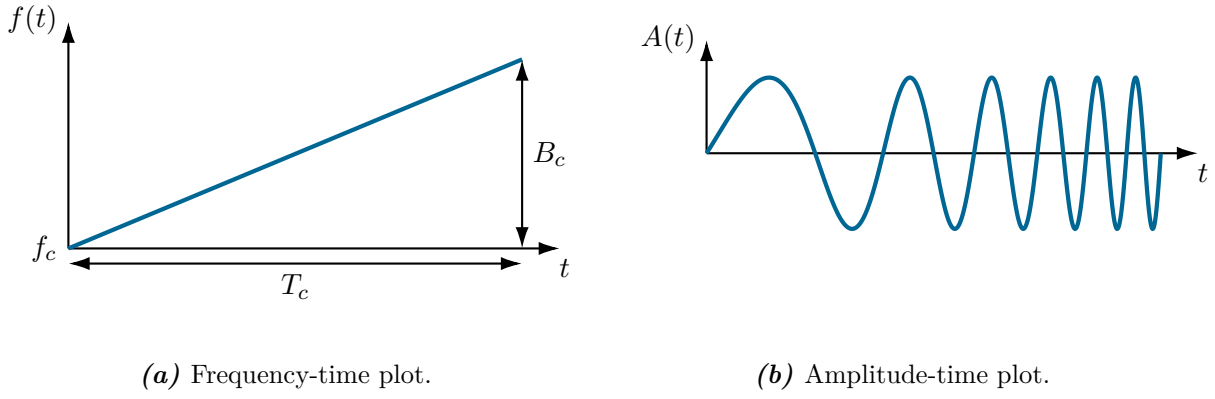
Figure 2.2. Illustration of a chirp.

angular carrier frequency can be expressed as

$$A(t) = A_0 \sin\left(\pi S t^2 + \omega_c t + \varphi_0\right) \quad \text{for } 0 < t < T_c, \tag{2.9}$$

where A_0 is the peak amplitude of the chirp.

Consider the FMCW radar setup in Figure 2.3. Here, a generated chirp is emitted by the transmitter. The chirp is then reflected on an object and the reflected chirp is received at the receiver, where a mixer is used to downconvert the received chirp. An ideal mixer is a multiplier that multiplies two input signals and gives the mixed signal as an output. Consider the two sinusoids

$$f_1(t) = \sin(\omega_1 t + \varphi_1) \qquad \text{and} \qquad f_2(t) = \sin(\omega_2 t + \varphi_2) \tag{2.10}$$

as inputs. Then, the mixed signal is

$$f_{\text{out}}(t) = f_1(t) \cdot f_2(t) \tag{2.11}$$

$$= \sin(\omega_1 t + \varphi_1) \cdot \sin(\omega_2 t + \varphi_2) \tag{2.12}$$

$$= \frac{1}{2}\Big(\cos\left((\omega_1 - \omega_2)t + (\varphi_1 - \varphi_2)\right) - \cos\left((\omega_1 + \omega_2)t + (\varphi_1 + \varphi_2)\right)\Big). \tag{2.13}$$

This has two components: one at the radian frequency $(\omega_1 - \omega_2)$ with phase $(\varphi_1 - \varphi_2)$ and the other at the radian frequency $(\omega_1 + \omega_2)$ with phase $(\varphi_1 + \varphi_2)$. If the frequencies of the two input signals are similar, then the component at $(\omega_1 - \omega_2)$ will be much lower than both the input signals, and the component at $(\omega_1 + \omega_2)$ will be almost twice the input frequencies. Thus, a bandpass filter is needed to sort away the unwanted component. In an FMCW radar, the
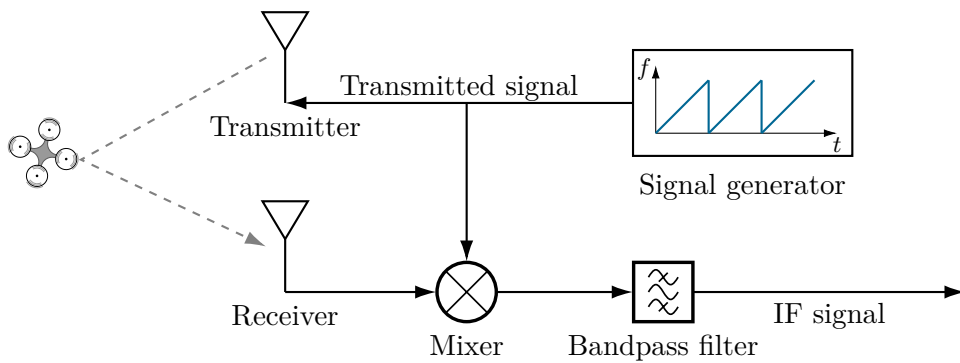
Figure 2.3. FMCW radar setup.
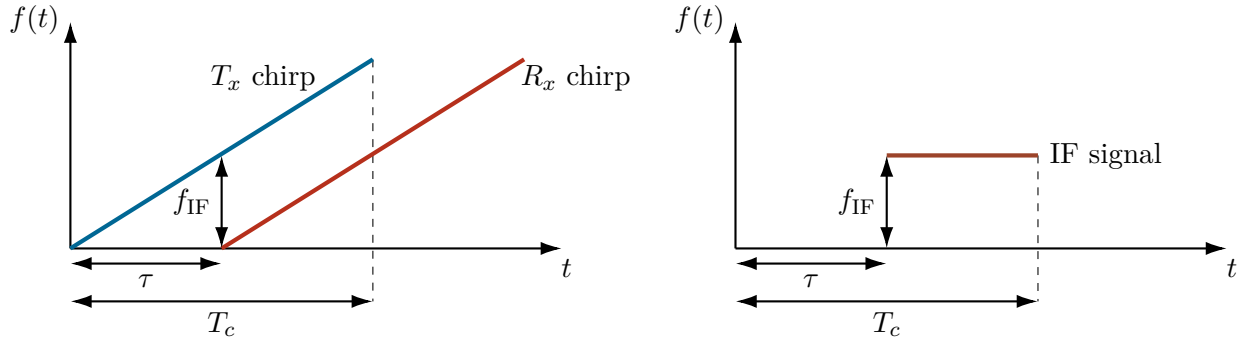
(a) Frequency of transmitted and received chirp.   **(b)** Frequency of the IF signal.

Figure 2.4. IF for a SISO FMCW radar with the transmitted chirp being reflected on a single object.

two inputs in the mixer are the transmitted and received signals, and the output is called an intermediate frequency (IF) signal.

To gain a better understanding of the IF signal, consider a single-input single-output (SISO) radar where the transmitted signal is reflected on a single object. The frequency of a transmitted and received chirp in this scenario is illustrated in Figure 2.4a. Note that, the received chirp is just a delayed version of the transmitted chirp, where τ denotes the two-way time delay between the radar and the object. Typically, τ is a small fraction of the total chirp time, thus the non-overlapping segments of the chirps are usually negligible. The frequency of the corresponding IF signal is shown in Figure 2.4b which is constant since it is the difference of the instantaneous frequency of the transmitted and received chirp. The frequency of this constant wave is

$$f_{\text{IF}}(t) = f_{T_x}(t) - f_{R_x}(t) = St - S(t - \tau) = \frac{2Sr}{c}, \tag{2.14}$$

where $f_{R_x}(t)$ and $f_{T_x}(t)$ are the frequency of the received and transmitted signal, respectively, since $\tau = 2r/c$, where r is the range to the object and c is the speed of light. In an amplitude-time
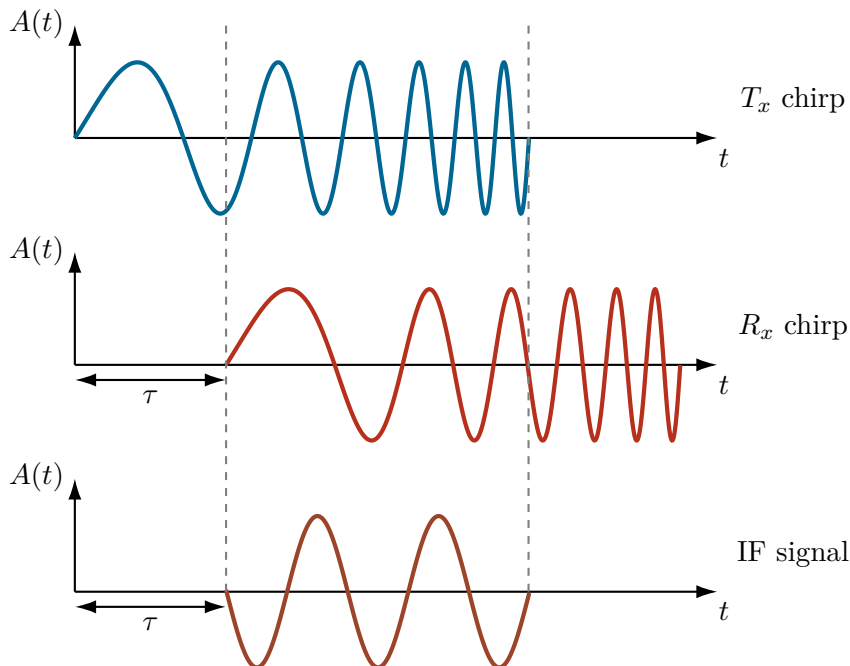
Figure 2.5. Amplitude of a transmitted chirp, a received chirp, and the corresponding IF signal.

(a) Frequency of the transmitted and received signals.
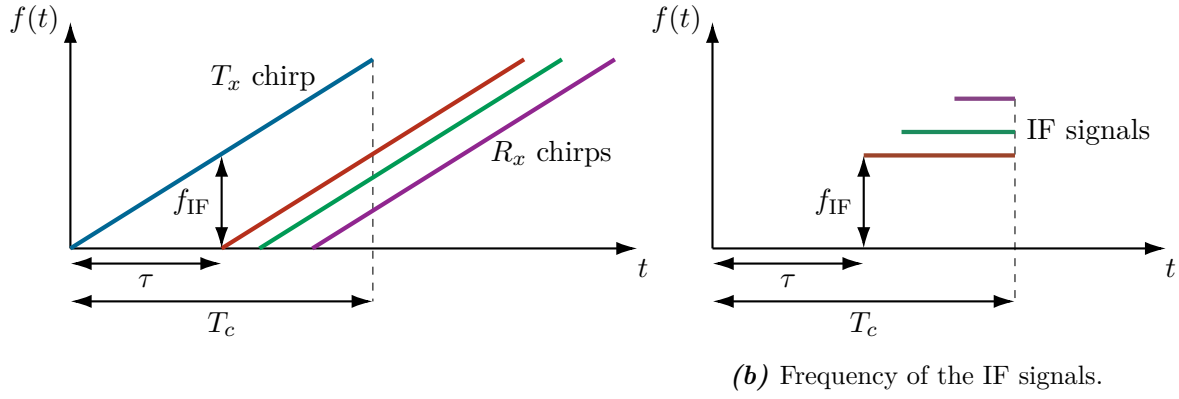
(b) Frequency of the IF signals.

Figure 2.6. IFs for a SISO FMCW radar with the transmitted signal being reflected on multiple objects.

plot, the amplitude of the transmitted and received chirp with the corresponding amplitude of the IF signal is seen in Figure 2.5. Here, the IF signal ends up being a sinusoid with constant frequency.

When multiple objects reflect the transmitted signal, the received signal is composed of all the reflected signals due to the superposition principle. The frequency of a single transmitted chirp and the multiple received chirps is illustrated in Figure 2.6a. The resulting IF signal is composed of multiple signals with different frequencies as shown in Figure 2.6b.

When using a MIMO FMCW radar, the contributions from each transmitter on each receiver must be separated. For this, the transmitted signals should ideally be orthogonal to ensure that there is no correlation between the signals, but this is not a strict requirement. One simple approach to obtain separable signals is through frequency division multiplexing (FDM). Here, the total bandwidth is divided into a number of sub-bands that do not overlap in frequency depending on the number of transmitters. Each transmitter is then allocated a certain sub-band, as depicted in Figure 2.7. [Li and Stoica, 2009, p. 67]
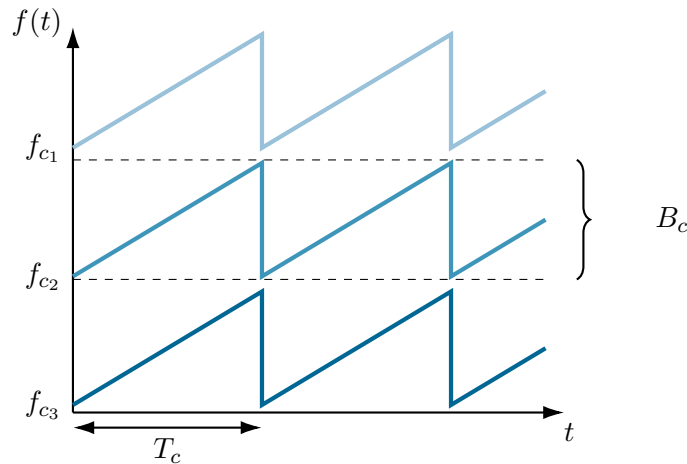
Figure 2.7. Illustration of the FDM principle for sawtooth patterns.

Another approach to obtain separable signals is to use time division multiplexing (TDM) where each transmitter sends out a signal during a specific frame. The signal transmitted in one frame is called a pulse. After the frame for one transmitter ends, the next transmitter transmits the same signal during its allocated frame. This sequence, repeated for all transmitters, forms a

MIMO cycle. Figure 2.8 illustrates this principle for four transmitters. [Zwanetski and Rohling, 2012]
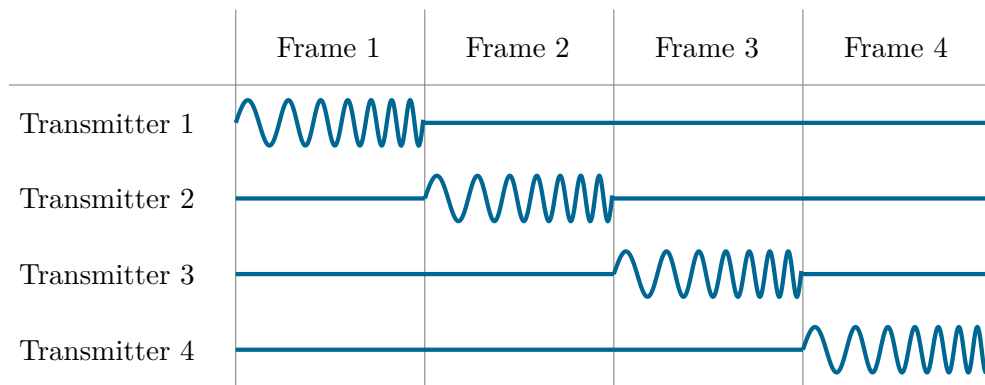
Figure 2.8. Illustration of the TDM principle with four transmitters.

Signal Model 3

In this chapter, a signal model will be derived for the signals received by the N_{radar} MIMO FMCW radars, each equipped with N_T transmitters and N_R receivers, considering a clutter environment containing one target.

Consider the setup in Figure 3.1. Here, transmitter m on radar k emits a signal

$$\mathcal{X}^{(m,k)}(t) = \text{Re}\left\{u^{(m,k)}\text{e}^{i\omega_c t}\right\}, \tag{3.1}$$

where $u^{(m,k)} \in \mathbb{C}$ is the complex baseband signal, i is the imaginary unit, and $\omega_c = 2\pi f_c$ is the angular carrier frequency. The transmission is repeated with an interval Δt. The transmitted signal propagates throughout, reflects on the environment, and is collected by each receiver on the radar it originated from.

The environment is assumed to be slow moving compared to the total transmission time across all transmitters, hence the "stop-and-hop" approximation is employed. Therefore, the model parameters are considered time invariant between pulses. The reflected signals induce a signal $\mathcal{Y}_n^{(j,k)} \in \mathbb{C}$ in receiver j on radar k, where n is the MIMO cycle index. The induced signal is seen as a sum of the received signals from the target and the received signals from the clutter environment:

$$\mathcal{Y}_n^{(j,k)}(t) = s_{n,\text{target}}^{(j,k)}(t) + s_{n,\text{clutter}}^{(j,k)}(t) + w_n^{(j,k)}(t), \tag{3.2}$$

where $s_{n,\text{target}}^{(j,k)}(t)$ is the received target signal, $s_{n,\text{clutter}}^{(j,k)}(t)$ is the received clutter signal, and $w_n^{(j,k)}(t)$ is the thermal noise unrelated to the received signal given as complex circularly symmetric white Gaussian noise with zero mean and variance σ_w^2. This allows for finding an expression for the target signal and the clutter signal separately, and joining them later to get the total signal model.

The received signals are matched filtered to obtain the signal for each individually reflected signal. This results in $N_T N_R$ signals for each radar, each of which is described as

$$z_n^{(m,j,k)}(t) = \mathcal{Y}_n^{(j,k)}(t) * \left(u^{(m,k)}\right)^*(t) \tag{3.3}$$

$$= s_{n,\text{target}}^{(j,k)}(t) * \left(u^{(m,k)}\right)^*(t) + s_{n,\text{clutter}}^{(j,k)}(t) * \left(u^{(m,k)}\right)^*(t) + w_n^{(j,k)}(t) * \left(u^{(m,k)}\right)^*(t) \tag{3.4}$$

$$= s_{n,\text{target}}^{(m,j,k)}(t) + s_{n,\text{clutter}}^{(m,j,k)}(t) + w_n^{(m,j,k)}(t), \tag{3.5}$$

where $\left(u^{(m,k)}\right)^*$ denotes the complex conjugate of $u^{(m,k)}$.
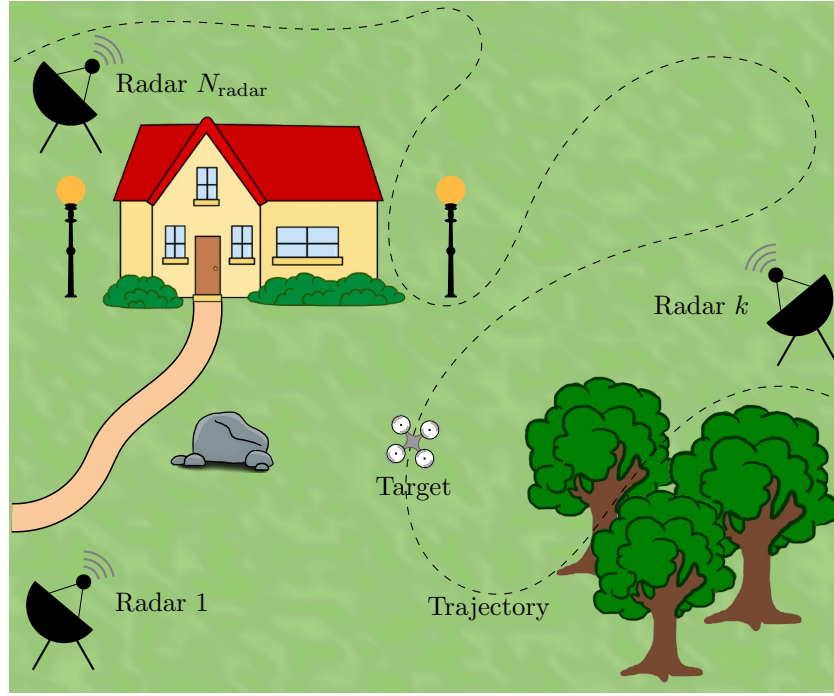
Figure 3.1. Setup of radars illuminating a clutter environment containing one target.

3.1 Target Signal Model

Start by considering one target in a clutter-free environment as depicted in Figure 3.2 to model $s_{n,\text{target}}^{(j,k)}$ in (3.2). The target is described by its kinematic parameters

$$\phi(t) = \begin{bmatrix} x(t) & y(t) & v^{(x)}(t) & v^{(y)}(t) \end{bmatrix}^{\top}, \tag{3.6}$$

where $[x(t)\ y(t)]^{\top}$ denotes the position of the target in a global Cartesian coordinate system while $v^{(x)}(t)$ and $v^{(y)}(t)$ denote the velocities along the x- and y-axes, respectively. Each radar observes the kinematic parameters of the target in local coordinates. The relation between the local coordinate system $[x^{(k)}\ y^{(k)}]^{\top}$ and the global coordinate system $[x\ y]^{\top}$ is seen in Figure 3.3.

As the "stop-and-hop" approximation is utilised, the kinematic parameters are considered time invariant between pulses, meaning $\phi(t) = \phi_n$ for $n\Delta t \leq t < (n+1)\Delta t$. As a result, it is assumed that the Doppler shift is zero.

The target signal model is modelled as a single reflected signal from each transmitter. By assuming single-bounce, the target signal for radar k is given as

$$s_{n,\text{target}}^{(j,k)}(t) = \sum_{m=1}^{N_T} \tilde{\alpha}_n^{(m,j,k)} u^{(m,k)}\Big(t - \tau_n^{(m,k)} - \tau_n^{(j,k)}\Big) \mathrm{e}^{i\omega_c\left(t - \tau_n^{(m,k)} - \tau_n^{(j,k)}\right)}, \tag{3.7}$$

where $\tilde{\alpha}_n^{(m,j,k)}$ is the path loss between transmitter m and receiver j on radar k, calculated by (2.5). Furthermore, $\tau_n^{(m,k)}$ is the time delay from transmitter m on radar k to the target and $\tau_n^{(j,k)}$ is the time delay from the target to receiver j on radar k. [Li and Stoica, 2009, p. 156]

Figure 3.4 shows the notation used for the transmitter array, where the notation for the receiver array is denoted similarly. The total two-way time delay from transmitter m to the
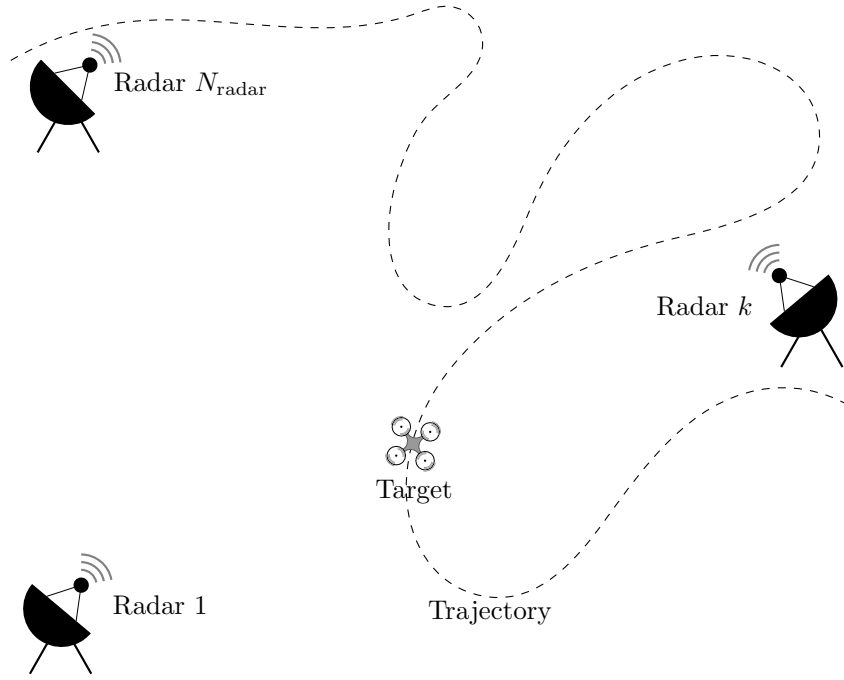
Figure 3.2. Setup of radars illuminating a clutter-free environment containing one target.
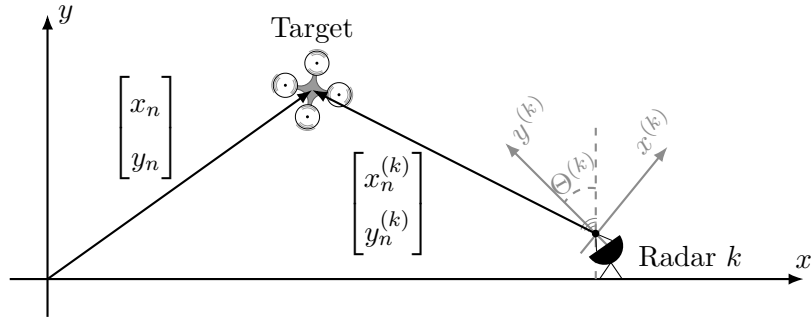
Figure 3.3. The relation between the local coordinate system $[x^{(k)} \ y^{(k)}]^\top$ and the global coordinate system $[x \ y]^\top$ which the algorithm runs in.
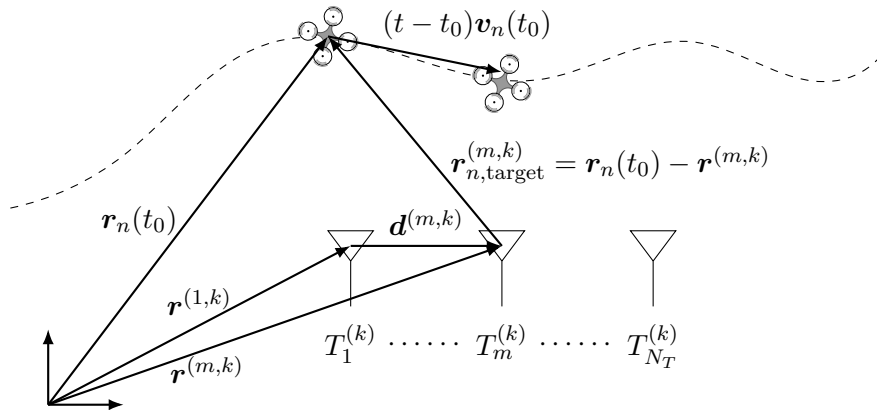
Figure 3.4. Transmitter array and target in a single coordinate system, including their position vectors and corresponding notation. The notation for the receiver array is denoted similarly.

target and back to receiver j is expressed as

$$\tau_n^{(k)} = \tau_n^{(m,k)} + \tau_n^{(j,k)} = \frac{1}{c}\left(\left|\boldsymbol{r}_n(t) - \boldsymbol{r}^{(m,k)}\right| + \left|\boldsymbol{r}_n(t) - \boldsymbol{r}^{(j,k)}\right|\right), \tag{3.8}$$

where $\boldsymbol{r}_n(t) = [x_n(t)\ y_n(t)]^\top$ denotes the position vector of the target, and $\boldsymbol{r}^{(m,k)} = [x^{(m,k)}\ y^{(m,k)}]^\top$ and $\boldsymbol{r}^{(j,k)} = [x^{(j,k)}\ y^{(j,k)}]^\top$ denotes the position vector of transmitter m and receiver j on radar k, respectively. By assuming that the positions of the radar and target are described with a single coordinate system, the position vector of a moving target is estimated as a first order Taylor series around t_0:

$$\hat{\boldsymbol{r}}_n(t) = \boldsymbol{r}_n(t_0) + (t - t_0)\boldsymbol{v}_n(t_0), \tag{3.9}$$

where $\hat{\boldsymbol{r}}_n(t) \approx \boldsymbol{r}_n(t)$ and $\boldsymbol{v}_n(t_0) = [v_n^{(x)}(t_0)\ v_n^{(y)}(t_0)]^\top$ denotes the velocity vector of the target at time t_0. Inserting (3.9) into (3.8) yields

$$\tau_n^{(k)} \approx \frac{1}{c}\left(\left|\boldsymbol{r}_n(t_0) + (t - t_0)\boldsymbol{v}_n(t_0) - \boldsymbol{r}^{(m,k)}\right| + \left|\boldsymbol{r}_n(t_0) + (t - t_0)\boldsymbol{v}_n(t_0) - \boldsymbol{r}^{(j,k)}\right|\right). \tag{3.10}$$

The first term in the parenthesis is now looked upon. By the triangle inequality:

$$\left|\boldsymbol{r}_n(t_0) + (t - t_0)\boldsymbol{v}_n(t_0) - \boldsymbol{r}^{(m,k)}\right| \leq \left|\boldsymbol{r}_n(t_0) - \boldsymbol{r}^{(m,k)}\right| + (t - t_0)|\boldsymbol{v}_n(t_0)| \tag{3.11}$$

By assuming that the changes in distance due to the velocity vector are small compared to the initial distance over short time intervals, the inequality is seen as an approximation. Denoting the distance between transmitter m on radar k and the target at time t_0 as $\boldsymbol{r}_{n,\text{target}}^{(m,k)}$, the corresponding unit vector is

$$\bar{\boldsymbol{r}}_{n,\text{target}}^{(m,k)} = \frac{\boldsymbol{r}_{n,\text{target}}^{(m,k)}}{\left|\boldsymbol{r}_{n,\text{target}}^{(m,k)}\right|}. \tag{3.12}$$

Assuming the target is in the far-field, the unit vectors for different transmitters on radar k become approximately equal:

$$\bar{\boldsymbol{r}}_{n,\text{target}}^{(1,k)} \approx \bar{\boldsymbol{r}}_{n,\text{target}}^{(2,k)} \approx \cdots \approx \bar{\boldsymbol{r}}_{n,\text{target}}^{(N_T,k)}. \tag{3.13}$$

This shared direction is denoted as $\bar{\boldsymbol{r}}_{n,\text{target}}^{(T,k)}$. As it is the velocity component along the line of sight that is of interest, the velocity vector is projected onto the unit vector. The projection is seen as an approximation, because the distance due to the velocity term is assumed small compared to the initial distance. Thus, (3.11) becomes

$$\left|\boldsymbol{r}_n(t_0) + (t - t_0)\boldsymbol{v}_n(t_0) - \boldsymbol{r}^{(m,k)}\right| \approx \left|\boldsymbol{r}_{n,\text{target}}^{(m,k)}\right| + \bar{\boldsymbol{r}}_{n,\text{target}}^{(T,k)} \cdot \boldsymbol{v}_n(t_0)(t - t_0). \tag{3.14}$$

The same holds for the second term in the parenthesis in (3.10) in relation to the receiver array. Thus, (3.10) becomes

$$\tau_n^{(k)} \approx \frac{1}{c}\left(\left|\boldsymbol{r}_{n,\text{target}}^{(m,k)}\right| + \bar{\boldsymbol{r}}_{n,\text{target}}^{(T,k)} \cdot \boldsymbol{v}_n(t_0)(t - t_0) + \left|\boldsymbol{r}_{n,\text{target}}^{(j,k)}\right| + \bar{\boldsymbol{r}}_{n,\text{target}}^{(R,k)} \cdot \boldsymbol{v}_n(t_0)(t - t_0)\right) \tag{3.15}$$

$$\approx \frac{1}{c}\left(\left|\boldsymbol{r}_{n,\text{target}}^{(m,k)}\right| + v_n^{(T,k)}(t - t_0) + \left|\boldsymbol{r}_{n,\text{target}}^{(j,k)}\right| + v_n^{(R,k)}(t - t_0)\right), \tag{3.16}$$

where $v_n^{(T,k)} = \vec{r}_{n,\text{target}}^{(T,k)} \cdot \boldsymbol{v}_n(t_0)$ and $v_n^{(R,k)} = \vec{r}_{n,\text{target}}^{(R,k)} \cdot \boldsymbol{v}_n(t_0)(t - t_0)$. The distances from the transmitter and receiver arrays to the target is rewritten as

$$\left| \boldsymbol{r}_{n,\text{target}}^{(m,k)} \right| = \underbrace{\left| \boldsymbol{r}_n(t_0) - \boldsymbol{r}^{(m=1,k)} \right|}_{r_{n,\text{target}}^{(m=1,k)}} + \underbrace{\left(-\vec{r}_{n,\text{target}}^{(m=1,k)} \cdot \boldsymbol{d}^{(m,k)} \right)}_{\Delta r_n^{(m,k)}}, \tag{3.17}$$

$$\left| \boldsymbol{r}_{n,\text{target}}^{(j,k)} \right| = \underbrace{\left| \boldsymbol{r}_n(t_0) - \boldsymbol{r}^{(j=1,k)} \right|}_{r_{n,\text{target}}^{(j=1,k)}} + \underbrace{\left(-\vec{r}_{n,\text{target}}^{(j=1,k)} \cdot \boldsymbol{d}^{(j,k)} \right)}_{\Delta r_n^{(j,k)}}, \tag{3.18}$$

where $\boldsymbol{d}^{(m,k)} = \boldsymbol{r}^{(m,k)} - \boldsymbol{r}^{(m=1,k)}$ and likewise for $\boldsymbol{d}^{(j,k)}$. Note that $\Delta r_n^{(m,k)}$ denotes the difference in travel distance for the transmitted signal from transmitter m on radar k compared to the transmitted signal from transmitter 1 on radar k, and likewise for $\Delta r_n^{(j,k)}$. Now, (3.16) is written as

$$\tau_n^{(k)} \approx \frac{1}{c} \left(r_{n,\text{target}}^{(m=1,k)} + \Delta r_n^{(m,k)} + v_n^{(T,k)}(t - t_0) + r_{n,\text{target}}^{(j=1,k)} + \Delta r_n^{(j,k)} + v_n^{(R,k)}(t - t_0) \right) \tag{3.19}$$

$$= \underbrace{\frac{r_{n,\text{target}}^{(m=1,k)} + r_{n,\text{target}}^{(j=1,k)}}{c} - t_0 \frac{v_n^{(T,k)} + v_n^{(R,k)}}{c}}_{\text{slow changing, } \tau_{n,S}} + t \overbrace{\frac{v_n^{(T,k)} + v_n^{(R,k)}}{c}}^{\tau_{n,D}^{(T,R,k)}} + \overbrace{\frac{\Delta r_n^{(m,k)}}{c}}^{\Delta \tau_n^{(m,k)}} + \overbrace{\frac{\Delta r_n^{(j,k)}}{c}}^{\Delta \tau_n^{(j,k)}}, \tag{3.20}$$

$$\underbrace{\hspace{10cm}}_{\text{fast changing}}$$

where $\tau_{n,D}^{(T,R,k)}$ contains the information from the Doppler shift. The terms labelled "fast changing" in (3.20) are ignored for the complex baseband signal since a small timing offset does not affect it significantly due to the long time scale of a single pulse repetition interval. Thus, (3.7) is written as

$$s_{n,\text{target}}^{(j,k)}(t) = \sum_{m=1}^{N_T} \tilde{\alpha}_n^{(m,j,k)} u^{(m,k)}\left(t - \tau_{n,S}\right) e^{i\omega_c\left(t - \tau_{n,S} - \tau_{n,D}^{(T,R,k)} + \Delta\tau_n^{(m,k)} + \Delta\tau_n^{(j,k)}\right)}. \tag{3.21}$$

As described in Section 2.1, the received signal at the R_x antenna is downconverted using a mixer. Thus, (3.21) is multiplied with the transmitted signal:

$$s_{n,\text{target}}^{(j,k)}(t) = \sum_{m=1}^{N_T} \tilde{\alpha}_n^{(m,j,k)} u^{(m,k)}\left(t - \tau_{n,S}\right) e^{i\omega_c\left(t - \tau_{n,S} - \tau_{n,D}^{(T,R,k)} + \Delta\tau_n^{(m,k)} + \Delta\tau_n^{(j,k)}\right)} \left(\mathcal{X}^{(m,k)} \right)^*(t). \tag{3.22}$$

Inserting (3.1) and using (2.8) in the complex baseband signal yields

$$s_{n,\text{target}}^{(j,k)}(t) = \sum_{m=1}^{N_T} \tilde{\alpha}_n^{(m,j,k)} e^{i\left(\pi S\left(t - \tau_{n,S}\right)^2 + \varphi_0\right)} e^{i\omega_c\left(t - \tau_{n,S} - \tau_{n,D}^{(T,R,k)} + \Delta\tau_n^{(m,k)} + \Delta\tau_n^{(j,k)}\right)} e^{-i\left(\pi St^2 + \varphi_0\right)} e^{-i\omega_c t} \tag{3.23}$$

$$= \sum_{m=1}^{N_T} \tilde{\alpha}_n^{(m,j,k)} e^{i\pi S\left(\left(t - \tau_{n,S}\right)^2 - t^2\right)} e^{i\omega_c\left(-\tau_{n,S} - \tau_{n,D}^{(T,R,k)} + \Delta\tau_n^{(m,k)} + \Delta\tau_n^{(j,k)}\right)}. \tag{3.24}$$

The first exponential term is rewritten as

$$e^{i\pi S\left(\left(t - \tau_{n,S}\right)^2 - t^2\right)} = e^{i\pi S\left(t^2 + \tau_{n,S}^2 - 2\tau_{n,S}t - t^2\right)} \tag{3.25}$$

$$= e^{i\pi S\left(\tau_{n,S}^2 - 2t\tau_{n,S}\right)} \tag{3.26}$$

$$= e^{i\pi S\tau_{n,S}^2} \cdot e^{-i2\pi S\tau_{n,S}t}. \tag{3.27}$$

Inserting (3.27) into (3.24) yields

$$s_{n,\text{target}}^{(j,k)}(t) = \sum_{m=1}^{N_T} \tilde{\alpha}_n^{(m,j,k)} \cdot \mathrm{e}^{i\pi S\tau_{n,S}^2} \cdot \mathrm{e}^{-i2\pi S\tau_{n,S}t} \cdot \mathrm{e}^{i\omega_c\left(-\tau_{n,S}-\tau_{n,D}^{(T,R,k)}+\Delta\tau_n^{(m,k)}+\Delta\tau_n^{(j,k)}\right)} \tag{3.28}$$

$$= \sum_{m=1}^{N_T} \tilde{\alpha}_n^{(m,j,k)} \cdot \mathrm{e}^{i\pi S\tau_{n,S}^2} \cdot \mathrm{e}^{-i2\pi S\tau_{n,S}t} \cdot \mathrm{e}^{-i\omega_c\tau_{n,S}} \cdot \mathrm{e}^{-i\omega_c\tau_{n,D}^{(T,R,k)}} \cdot \mathrm{e}^{i\omega_c\left(\Delta\tau_n^{(m,k)}+\Delta\tau_n^{(j,k)}\right)}. \tag{3.29}$$

The terms containing the slow changing time delay $\tau_{n,S}$ in the first and third exponential term is put into the path loss term. The fourth exponential term containing the time delay for the Doppler shift is disregarded as the "stop-and-hop" approximation is used. The last exponential term represents the time delay in relation to the distance between the transmitters and receivers, thus this term is contained in the steering matrix $A^{(m,j,k)}(x_n^{(k)}, y_n^{(k)})$. The second exponential term is rewritten using (2.14), thus the target signal model ends up being

$$s_{n,\text{target}}^{(j,k)}(t) = \sum_{m=1}^{N_T} \alpha_n^{(m,j,k)} A^{(m,j,k)}\left(x_n^{(k)}, y_n^{(k)}\right) \underbrace{\mathrm{e}^{-i2\pi f_{\text{IF}}\left(x_n^{(k)}, y_n^{(k)}\right)t}}_{u^{(m,k)}(t-\tau_n)\left(u^{(m,k)}\right)^*(t)}. \tag{3.30}$$

3.2   Clutter Signal Model

To model $s_{n,\text{clutter}}^{(j,k)}$ in (3.2), consider the clutter environment without a target present as depicted in Figure 3.5. Instead of modelling the received signal as a single reflected signal as for the target signal, now, the received signal consists of multiple reflected signals across the FOV. The clutter signal is modelled as a superposition of reflected signals according to the clutter field $C^{(k)}(x, y; t) \in \mathbb{C}$. The "stop-and-hop" approximation is utilised, thus $C^{(k)}(x, y; t) = C_n^{(k)}(x, y)$ for $n\Delta t \leq t < (n+1)\Delta t$. As a result, it is assumed that the Doppler shift is zero for the whole field. By assuming single-bounce, the clutter signal for radar k is given as

$$s_{n,\text{clutter}}^{(j,k)}(t) = \sum_{m=1}^{N_T} \int_{\mathbb{R}^2} C_n^{(k)}(x, y) u^{(m,k)}\left(t - \tau^{(m,k)} - \tau^{(j,k)}\right) \mathrm{e}^{i\omega_c\left(t-\tau^{(m,k)}-\tau^{(j,k)}\right)} \, \mathrm{d}x\mathrm{d}y. \tag{3.31}$$

This expression is rewritten using the same procedure as in Section 3.1, yielding

$$s_{n,\text{clutter}}^{(j,k)}(t) = \sum_{m=1}^{N_T} \int_{\mathbb{R}^2} C_n^{(k)}(x, y) A^{(m,j,k)}(x, y) \mathrm{e}^{-i2\pi f_{\text{IF}}(x,y)t} \, \mathrm{d}x\mathrm{d}y. \tag{3.32}$$

The clutter field is modelled as a two-dimensional stochastic process, known as a random field, to effectively represent its spatial and temporal dynamics.

3.2.1   Random Fields

In this section, based on [Adler and Taylor, 2015, pp. 23, 27-28, 30, 36-37], [Root and Pitcher, 1955], [Başar et al., 2016, p. 39] and [Li and Chen, 2014, pp. 16, 19], an introduction to random fields is presented including Gaussian random fields and orthogonal expansions of random fields.
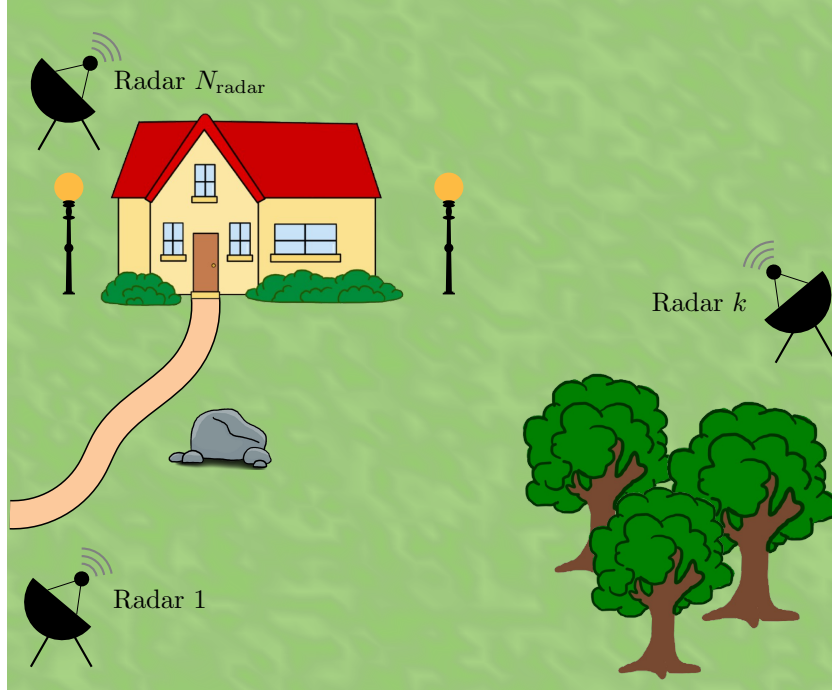
Figure 3.5. Setup of radars illuminating a clutter environment containing no target.

Definition 3.2.1 (Random Field)

Given an index space Z, a stochastic process C over Z is a collection of random variables

$$\{C(\boldsymbol{z}) : \boldsymbol{z} \in Z\}. \tag{3.33}$$

If Z is a set of dimension N, and the random variables $C(\boldsymbol{z})$ are all vector valued of dimension d, then the vector valued stochastic process C is called an (N, d) random field.

[Adler and Taylor, 2015, Definition 2.1.1]

Note that the index variable $\boldsymbol{z}$ can represent time, space, or other relevant domains. Furthermore, an $(N, 1)$ random field is called an N-dimensional random field.

By Kolmogorov's extension theorem, Theorem A.1.1, a random field's distributional properties are completely determined by the finite-dimensional distributions for the field. These finite-dimensional distributions are defined as the joint probability distributions of the random variables $C(\boldsymbol{z}_1), \ldots, C(\boldsymbol{z}_n)$ for any finite subset of indices $\{\boldsymbol{z}_1, \ldots, \boldsymbol{z}_n\} \subseteq Z$. From this, the definition of Gaussian random fields naturally follows, as the field is called a Gaussian random field if all the finite-dimensional distributions of the random field are multivariate Gaussian. Gaussian random fields are determined by their mean $\boldsymbol{\mu}_C$ and precision $\boldsymbol{\Lambda}_C$.

When modelling a random field, problems might be encountered due to the complexity of the field. One solution is to transform the representation of the field using orthogonal expansions. Transforming the representation of a random field is essential for both theoretical insights and practical calculations.

Orthogonal Expansions of Random Fields

Consider an N-dimensional random field $C(\boldsymbol{z}) \in \mathbb{C}$ with $\boldsymbol{z} \in \mathbb{R}^N$. The random field is expressed by the synthesis equation:

$$C(\boldsymbol{z}) = \sum_{l}^{\infty} \gamma^{(l)} \psi^{(l)}(\boldsymbol{z}), \tag{3.34}$$

where $\{\gamma^{(l)}\}_{\forall l}$ are random variables called expansion coefficients and $\{\psi^{(l)}\}_{\forall l}$ are deterministic basis functions. The basis is denoted by $\Psi = \{\psi^{(l)}(\boldsymbol{z})\}_{\forall l}$ and (3.34) holds if Ψ forms a complete basis, meaning that any square integrable function C defined over a domain in $\boldsymbol{z}$ can be represented as a linear combination of the basis functions in Ψ. The basis functions are orthonormal in $L^2(\mathbb{R}^N)$, meaning

$$\left\langle \psi^{(l)}(\boldsymbol{z}), \psi^{(l')}(\boldsymbol{z}) \right\rangle = \int_{\mathbb{R}^N} \psi^{(l)}(\boldsymbol{z}) \left(\psi^{(l')} \right)^*(\boldsymbol{z}) \, \mathrm{d}\boldsymbol{z} = \delta_{l,l'}, \tag{3.35}$$

where $\delta_{l,l'}$ is the Kronecker delta function and $\langle \cdot, \cdot \rangle$ is the inner product. Some properties of orthogonal expansions of random fields are presented in Section A.1.1, including the covariance and autocorrelation function.

Given an observation of a random field $C(\boldsymbol{z})$, the expansion coefficients $\{\gamma^{(l)}\}_{\forall l}$ for the random field is determined by calculating the inner product. For one expansion coefficient $\psi^{(g)}$ the inner product is given as

$$\left\langle C(\boldsymbol{z}), \psi^{(g)}(\boldsymbol{z}) \right\rangle = \left\langle \sum_{l}^{\infty} \gamma^{(l)} \psi^{(l)}(\boldsymbol{z}), \psi^{(g)}(\boldsymbol{z}) \right\rangle \tag{3.36}$$

$$= \sum_{l}^{\infty} \gamma^{(l)} \left\langle \psi^{(l)}(\boldsymbol{z}), \psi^{(g)}(\boldsymbol{z}) \right\rangle. \tag{3.37}$$

Since the basis functions are orthonormal they satisfy

$$\left\langle \psi^{(l)}(\boldsymbol{z}), \psi^{(g)}(\boldsymbol{z}) \right\rangle = \begin{cases} 1, & \text{if } l = g, \\ 0, & \text{otherwise.} \end{cases} \tag{3.38}$$

Thus,

$$\gamma^{(g)} = \left\langle C(\boldsymbol{z}), \psi^{(g)}(\boldsymbol{z}) \right\rangle \tag{3.39}$$

$$= \int_{\mathbb{R}^N} C(\boldsymbol{z}) \left(\psi^{(g)} \right)^*(\boldsymbol{z}) \, \mathrm{d}\boldsymbol{z}. \tag{3.40}$$

The same procedure is repeated to determine all expansion coefficients $\{\gamma^{(l)}\}_{\forall l}$. This is called the analysis equation.

When using orthogonal expansions, the orthogonal basis can either be constructed using the Gram-Schmidt procedure or be chosen from well-known bases such as the Fourier basis. Expansion in the Fourier basis is useful for modelling periodic and stationary processes, since it decomposes the field into a sum of complex exponentials:

$$C(\boldsymbol{z}) = \sum_{l=-\infty}^{\infty} \gamma^{(l)} e^{i \boldsymbol{\omega}_l^\top \boldsymbol{z}}, \tag{3.41}$$

where $\Psi^F = \{e^{i\boldsymbol{\omega}_l^\top \boldsymbol{z}}\}_{\forall l}$ is the Fourier basis. The complex exponential basis functions form a complete orthogonal basis for square integrable functions on a bounded interval due to the periodicity of the basis.

The expansion coefficients $\{\gamma^{(l)}\}_{\forall l}$ can follow either a Gaussian distribution or non-Gaussian distributions. If $\{\gamma^{(l)}\}_{\forall l}$ follow a complex Gaussian distribution, then $C(\boldsymbol{z})$ would be a complex Gaussian random field. Expansions using Gaussian expansion coefficients are typically used to model processes that exhibit smoothness and predictability, where the noise is characterised by Gaussian distributions. When the expansion coefficients follow a non-Gaussian distribution, such as the Poisson or complex Laplace distribution, the resulting random field is also non-Gaussian. These distributions work well for representing non-stationary, complex random fields with non-linear behaviour such as spikes, discontinuities, and skewness.

Approximation of Random Fields using Orthogonal Expansions

Theoretically, a random field is expanded as an infinite sum of orthogonal basis functions, however, a digital implementation require a finite approximation due to memory and computational limitations. Thus, the field must be represented using a finite number of orthogonal basis functions to reduce complexity while preserving its characteristics.

The field will be approximated using a subset of the basis. Let $\Psi = \{\psi^{(l)}\}_{\forall l}$ be the complete set of basis functions and $\Psi_{N_B} \subset \Psi$ be the selected subset, where N_B denotes the number of retained basis functions. The approximation of $C(\boldsymbol{z})$ is given as

$$\hat{C}(\boldsymbol{z}) = \sum_{l=1}^{N_B} \left(\gamma^{(l)}\right)' \left(\psi^{(l)}\right)'(\boldsymbol{z}), \tag{3.42}$$

where $\{(\psi^{(l)})'(\boldsymbol{z})\}_{l=1}^{N_B}$ form the reduced basis and $\{(\gamma^{(l)})'\}_{l=1}^{N_B}$ are the corresponding expansion coefficients. The selected subset of basis functions does not necessarily correspond to the first N_B elements of the complete basis, that is $\{(\psi^{(l)})'\}_{l=1}^{N_B} \neq \{\psi^{(l)}\}_{l=1}^{N_B}$. In practice, it is desired to use the fewest basis functions necessary to represent the random field while minimising the error:

$$E_{N_B} = \frac{1}{\mathcal{A}} \int_{\mathbb{R}^N} \left|C(\boldsymbol{z}) - \hat{C}(\boldsymbol{z})\right|^2 \mathrm{d}\boldsymbol{z}, \tag{3.43}$$

where $\mathcal{A}$ is the area of the domain that is integrated over. For discrete representations of the field, the integrals are replaced with summations, and $\mathcal{A}$ is the number of elements in the sum.

Example 3.2.2 (Fourier Basis Functions)
Consider a two-dimensional discrete random field given as $C(x, y)$ for $x = 0, \ldots, N_x - 1$ and $y = 0, \ldots, N_y - 1$. The field is represented using the Fourier basis functions

$$\psi^{(l,g)}(x, y) = \frac{1}{\sqrt{N_x N_y}} e^{i2\pi(lx/N_x + gy/N_y)}, \tag{3.44}$$

which form a complete orthonormal basis when $N_x N_y$ basis functions are used. To represent a random field using the orthonormal basis, the $N_x N_y$ basis functions are scaled by the expansion coefficients and summed. Thus,

$$C(x, y) = \sum_{l=0}^{N_x-1} \sum_{g=0}^{N_y-1} \gamma^{(l,g)} \psi^{(l,g)}(x, y). \tag{3.45}$$

Let $N_x = N_y = 20$, such that

$$\psi^{(l,g)}(x,y) = \frac{1}{20}e^{i2\pi(lx+gy)/20}. \tag{3.46}$$

Using $l = 2$ and $g = 0$, Figure 3.6 shows different representations of the basis function $\psi^{(2,0)}(x,y)$, where the real and imaginary part of $\psi^{(2,0)}(x,y)$ are given as

$$\psi^{(2,0)}(x,y) = \frac{1}{20}e^{i4\pi x/20} \tag{3.47}$$

$$= \underbrace{\frac{1}{20}\cos(4\pi x/20)}_{\text{Re}(\psi^{(2,0)}(x,y))} + i\underbrace{\frac{1}{20}\sin(4\pi x/20)}_{\text{Im}(\psi^{(2,0)}(x,y))}. \tag{3.48}$$

Note that $|\psi^{(2,0)}(x,y)| = 1/20$ for all (x,y) since the real and imaginary part of $\psi^{(2,0)}(x,y)$ lies on the unit circle scaled by $1/20$.

(a) $|\psi^{(2,0)}(x,y)|$.   *(b)* $\text{Re}(\psi^{(2,0)}(x,y))$.   *(c)* $\text{Im}(\psi^{(2,0)}(x,y))$.
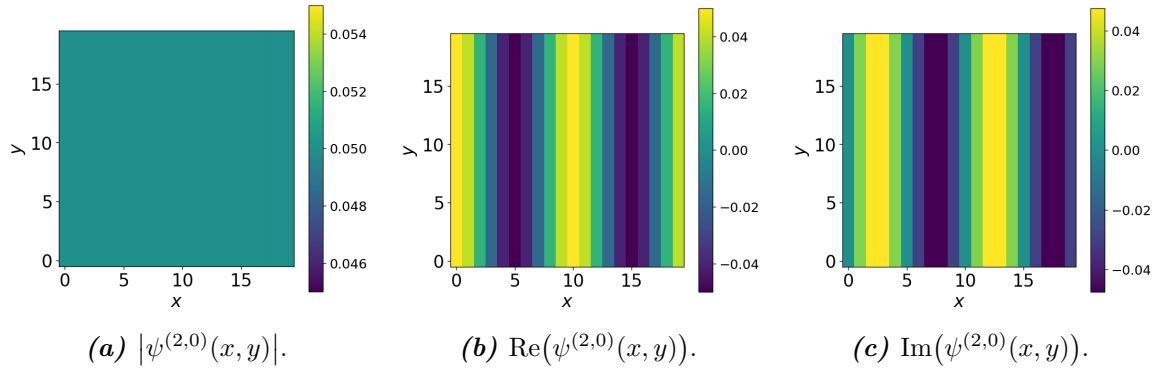
Figure 3.6. Different representations of the Fourier basis function $\psi^{(2,0)}(x,y)$.

Using $l = 2$ and $g = 4$ instead, Figure 3.7 shows the real and imaginary part of $\psi^{(2,4)}(x,y)$. The absolute value of $\psi^{(2,4)}(x,y)$ is the same as in Figure 3.6a.

(a) $\text{Re}(\psi^{(2,4)}(x,y))$.   *(b)* $\text{Im}(\psi^{(2,4)}(x,y))$.
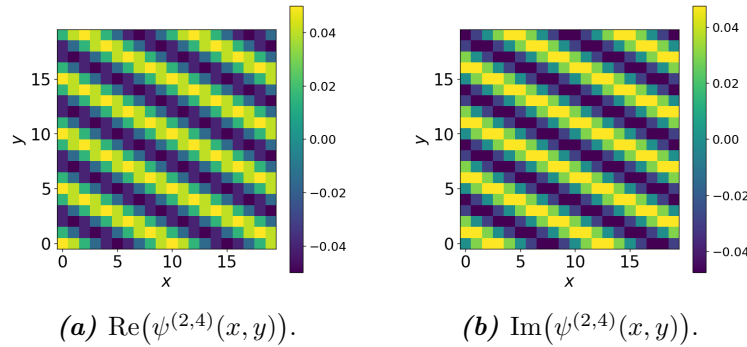
Figure 3.7. Different representations of the Fourier basis function $\psi^{(2,4)}(x,y)$.

Figure 3.8 shows different representations of the sum of $\psi^{(1,0)}(x,y)$ and $\psi^{(2,4)}(x,y)$, where

$$\text{Re}\Big(\psi^{(1,0)}(x,y) + \psi^{(2,4)}(x,y)\Big) = \frac{1}{20}\Big(\cos(2\pi x/20) + \cos(2\pi(2x+4y)/20)\Big), \tag{3.49}$$

$$\text{Im}\Big(\psi^{(1,0)}(x,y) + \psi^{(2,4)}(x,y)\Big) = \frac{1}{20}\Big(\sin(2\pi x/20) + \sin(2\pi(2x+4y)/20)\Big). \tag{3.50}$$

Now, the absolute value is no longer $1/20$ for all (x, y) as the real and imaginary part no longer lies on the unit circle.

(a)
$\left|\psi^{(1,0)}(x,y) + \psi^{(2,4)}(x,y)\right|$.

(b)
$\mathrm{Re}\left(\psi^{(1,0)}(x,y) + \psi^{(2,4)}(x,y)\right)$.

(c)
$\mathrm{Im}\left(\psi^{(1,0)}(x,y) + \psi^{(2,4)}(x,y)\right)$.
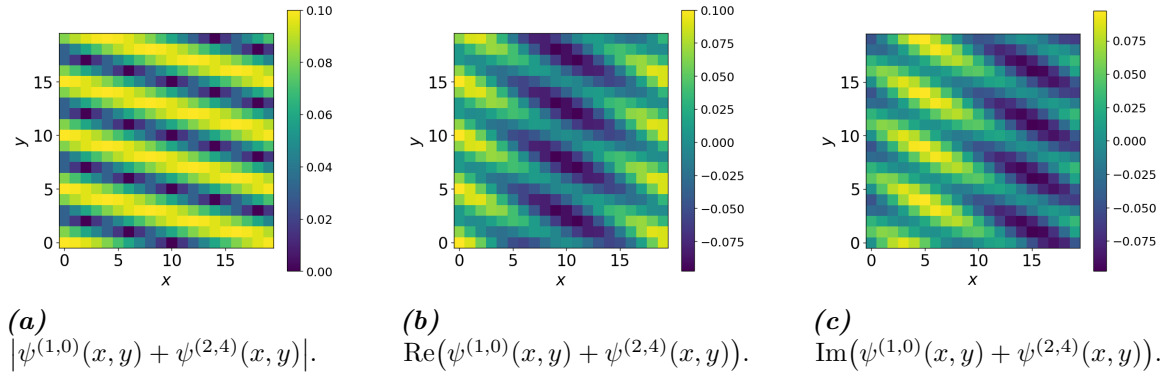
Figure 3.8. Different representations of the combined Fourier basis functions $\psi^{(1,0)}(x,y)$ and $\psi^{(2,4)}(x,y)$.

Consider an observation of a 20×20 discrete Gaussian random field $C(x, y)$, which is shown in Figure 3.9. This field can be represented exactly using the Fourier basis functions from (3.46):

$$C(x,y) = \frac{1}{20} \sum_{l=0}^{19} \sum_{g=0}^{19} \gamma^{(l,g)} \mathrm{e}^{i2\pi(lx+gy)/20}. \tag{3.51}$$

The expansion coefficients can be calculated using the analysis equation from (3.39):

$$\gamma^{(l,g)} = \left\langle C(x,y), \psi^{(l,g)}(x,y) \right\rangle \tag{3.52}$$

$$= \frac{1}{20} \sum_{x=0}^{19} \sum_{y=0}^{19} C(x,y) \mathrm{e}^{-i2\pi(lx+gy)/20}. \tag{3.53}$$

The absolute value of the expansion coefficients are shown in Figure 3.11a. Note that the majority of the expansion coefficients are close to zero, indicating that their corresponding basis functions do not contribute to the sum.
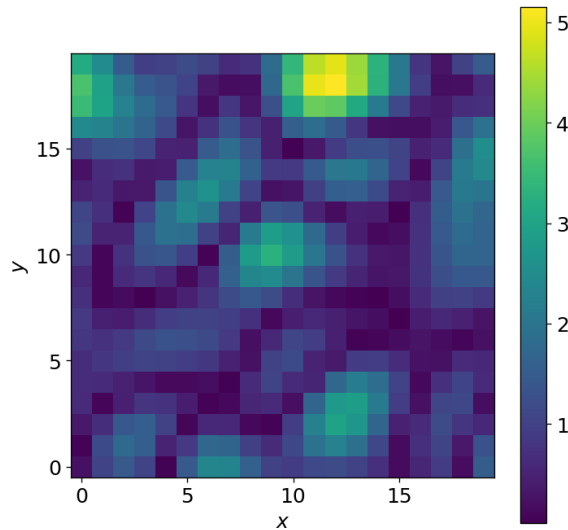
Figure 3.9. Example of a 20×20 discrete Gaussian random field.

Instead of describing the random field using all 400 basis functions, it is now approximated using the 37 basis functions for which $|\gamma^{(l,g)}| > 2$. The approximation $\hat{C}(x,y)$ is depicted in Figure 3.10 and the corresponding absolute value of the expansion coefficients are shown in Figure 3.11b.
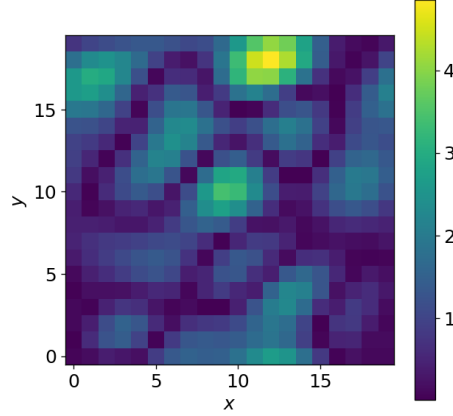
Figure 3.10. An approximation of the random field in Figure 3.9 using 37 basis functions.

(a) Figure 3.9.   *(b)* Figure 3.10.
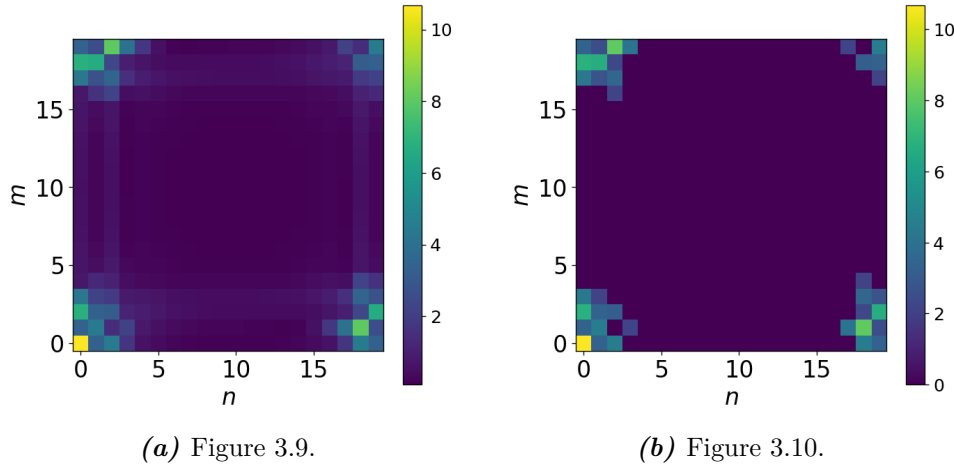
Figure 3.11. The expansion coefficients of the random field in Figure 3.9 and Figure 3.10.

The error of the approximation is

$$E_{37} = \frac{1}{400} \sum_{x,y} \left| C(x,y) - \hat{C}(x,y) \right|^2 = 0.33. \tag{3.54}$$

3.2.2 Clutter Signal Model using Random Fields

The clutter signal model from (3.32) is now rewritten using orthogonal expansions of random fields, where the clutter field is expressed using the synthesis equation from (3.34):

$$C_n^{(k)}(x,y) = \sum_{l,g} \gamma_n^{(l,g,k)} \psi^{(l,g)}(x,y), \tag{3.55}$$

where the basis functions are the same for all radars across all transmitter-receiver pairs. Inserting (3.55) in (3.32) results in

$$s_{n,\text{clutter}}^{(j,k)}(t) = \sum_{m=1}^{N_T} \int_{\mathbb{R}^2} \underbrace{\sum_{l,g} \gamma_n^{(l,g,k)} \psi^{(l,g)}(x,y)}_{C_n^{(k)}(x,y)} A^{(m,j,k)}(x,y) \mathrm{e}^{-i2\pi f_{\text{IF}}(x,y)t} \, \mathrm{d}x\mathrm{d}y \tag{3.56}$$

$$= \sum_{m=1}^{N_T} \sum_{l,g} \gamma_n^{(l,g,k)} \int_{\mathbb{R}^2} \psi^{(l,g)}(x,y) A^{(m,j,k)}(x,y) \mathrm{e}^{-i2\pi f_{\text{IF}}(x,y)t} \, \mathrm{d}x\mathrm{d}y. \tag{3.57}$$

A similar expansion is applied to $\left(A^{(m,j,k)}(x,y)\mathrm{e}^{-i2\pi f_{\text{IF}}(x,y)t}\right)^*$ using the same basis functions as in (3.55):

$$\left(A^{(m,j,k)}(x,y)\mathrm{e}^{-i2\pi f_{\text{IF}}(x,y)t}\right)^* = \sum_{l,g} \beta^{(l,g,m,j,k)}(t)\psi^{(l,g)}(x,y), \tag{3.58}$$

resulting in

$$A^{(m,j,k)}(x,y)\mathrm{e}^{-i2\pi f_{\text{IF}}(x,y)t} = \sum_{l,g} \left(\beta^{(l,g,m,j,k)}\right)^*(t)\left(\psi^{(l,g)}\right)^*(x,y). \tag{3.59}$$

An expression for the expansion coefficients is obtained by using the analysis equation from (3.39) on (3.59):

$$\left(\beta^{(l,g,m,j,k)}\right)^*(t) = \left\langle A^{(m,j,k)}(x,y)\mathrm{e}^{-i2\pi f_{\text{IF}}(x,y)t}, \left(\psi^{(l,g)}\right)^*(x,y)\right\rangle. \tag{3.60}$$

Inserting (3.59) in (3.57) yields:

$$s_{n,\text{clutter}}^{(j,k)}(t) = \sum_{m=1}^{N_T} \sum_{l,g} \gamma_n^{(l,g,k)} \underbrace{\left(\beta^{(l,g,m,j,k)}\right)^*(t)}_{\left\langle A^{(m,j,k)}(x,y)\mathrm{e}^{-i2\pi f_{\text{IF}}(x,y)t}, \left(\psi^{(l,g)}\right)^*(x,y)\right\rangle} \int_{\mathbb{R}^2} \psi^{(l,g)}(x,y)\left(\psi^{(l,g)}\right)^*(x,y) \, \mathrm{d}x\mathrm{d}y. \tag{3.61}$$

By choosing an orthonormal basis, the signal model for the clutter signal reduces to

$$s_{n,\text{clutter}}^{(j,k)}(t) = \sum_{m=1}^{N_T} \sum_{l,g} \left(\beta^{(l,g,m,j,k)}\right)^*(t)\gamma_n^{(l,g,k)}. \tag{3.62}$$

3.3 Total Signal Model

The total signal model is obtained by inserting (3.30) and (3.62) into (3.2):

$$\mathcal{Y}_n^{(j,k)}(t) = \sum_{m=1}^{N_T} \left[\alpha_n^{(m,j,k)} A^{(m,j,k)}\left(x_n^{(k)},y_n^{(k)}\right)\mathrm{e}^{-i2\pi f_{\text{IF}}\left(x_n^{(k)},y_n^{(k)}\right)t} + \sum_{l,g}\left(\beta^{(l,g,m,j,k)}\right)^*(t)\gamma_n^{(l,g,k)}\right]$$
$$+ w_n^{(j,k)}(t), \tag{3.63}$$

where the model is based on the following assumptions:

- Objects are located in the far-field.
- The received signals contain only single-bounce reflections.
- Objects move slowly compared to transmission time, meaning the "stop-and-hop" approximation applies.

The total signal model is derived in continuous time, but must be sampled for digital processing. First, the total received signal from (3.63) is match filtered to obtain the received signal from each channel:

$$z_n^{(m,j,k)}(t) = s_{n,\text{target}}^{(m,j,k)}(t) + s_{n,\text{clutter}}^{(m,j,k)}(t) + w_n^{(m,j,k)}(t). \tag{3.64}$$

Now, the signal is discretised by sampling it

$$z_n^{(m,j,k)}[h] = z_n^{(m,j,k)}(hT_s), \tag{3.65}$$

where $h = 1, \ldots, N_s$ is the sampling index and $T_s = \frac{1}{f_s}$ is the sampling period. In the frequency domain, the signal is on the form:

$$Z_n^{(m,j,k)}[h'] = \mathcal{F}_{h \to h'}\left\{z_n^{(m,j,k)}[h]\right\} \tag{3.66}$$

$$= \mathcal{F}_{h \to h'}\left\{s_{n,\text{target}}^{(m,j,k)}[h]\right\} + \mathcal{F}_{h \to h'}\left\{s_{n,\text{clutter}}^{(m,j,k)}[h]\right\} + \mathcal{F}_{h \to h'}\left\{w_n^{(m,j,k)}[h]\right\} \tag{3.67}$$

$$= S_n^{(m,j,k)}[h'] + M^{(m,j,k)}[h']\mathbf{\Gamma}_n^{(k)} + W_n^{(m,j,k)}[h'], \tag{3.68}$$

where $M^{(m,j,k)}[h'] = \text{Vec}(\mathcal{F}_{h \to h'}\left\{\beta^{(l,g,m,j,k)}[h]\right\})^\dagger$, $\mathbf{\Gamma}^{(k)} = \text{Vec}(\gamma^{(l,g,k)}) \in \mathbb{C}^{N_B}$, and $\text{Vec}(\cdot)$ denotes the vectorisation. Lastly, $Z_n^{(m,j,k)}[h']$ is vectorised for all N_s samples for all transmitter-receiver pairs. This yields

$$\boldsymbol{Z}_n^{(k)} = \boldsymbol{S}_n^{(k)} + \boldsymbol{M}^{(k)}\mathbf{\Gamma}_n^{(k)} + \boldsymbol{W}_n^{(k)}, \tag{3.69}$$

where $\boldsymbol{Z}_n^{(k)} \in \mathbb{C}^{N_s N_T N_R}$ and $\boldsymbol{M}^{(k)} \in \mathbb{C}^{N_s N_T N_R \times N_B}$. Note that $\boldsymbol{Z}_n^{(k)}$ is constructed by concatenating the received signal samples across all transmitter–receiver pairs. For each transmitter m and receiver j, the N_s samples $Z_n^{(m,j,k)}[1], Z_n^{(m,j,k)}[2], \ldots, Z_n^{(m,j,k)}[N_s]$ are placed consecutively in $\boldsymbol{Z}_n^{(k)}$. These sample blocks are first stacked over all transmitters for a given receiver, and then repeated for each receiver.

Estimation of Signal Model Parameters

<div style="text-align: right; font-size: xx-large;">4</div>

In this chapter, expressions for the signal model parameters are derived. The parameters to be estimated are the target state vector $\boldsymbol{\phi}_n = [x_n\ y_n\ v_n^{(x)}\ v_n^{(y)}]^\top$ and the expansion coefficients $\boldsymbol{\Gamma}_n^{(k)} = \text{Vec}(\gamma_n^{(k)})$ for the clutter field. Since these parameters cannot be estimated directly from the received signals $\boldsymbol{Z}_n^{1:N_{\text{radar}}} = \boldsymbol{Z}_n^{(1)}, \ldots, \boldsymbol{Z}_n^{(N_{\text{radar}})}$, variational message passing is introduced as an inference method to estimate their posterior distributions.

4.1 Inference in Graphical Models using Variational Message Passing

This section, based on [Bishop, 2006, pp. 360-361, 394-398, 462-466], gives a brief introduction to inference in graphical models and variational message passing using the mean field approach.

A probabilistic graphical model represents random variables by nodes and their probabilistic dependencies through edges. Probabilistic graphical models are generally used to visualise probabilities and provide an overview of conditional independence between latent and observed variables. Message passing in graphical models is a method used for inference, where messages are exchanged between the nodes in a graph to compute marginal distributions. A message contains information about the probabilities of the respective nodes in the graphical model.

4.1.1 Inference in Graphical Models

Consider a joint probability $p(x_1, x_2, x_3)$, where x_i is a random variable. The joint probability is decomposed into a product of conditional probabilities such that

$$p(x_1, x_2, x_3) = p(x_3|x_2, x_1)p(x_2|x_1)p(x_1). \tag{4.1}$$

Each variable x_i is depicted as a node and the conditional probabilities are depicted as an edge between the linked nodes. An example is shown in Figure 4.1. When the graph is constructed this way, it forms a directed acyclic graph. The direction of each edge is determined by the underlying conditional probability, and acyclicity means that the graph never returns to the starting node when following the direction of the edges. This type of graphical model is also known as a Bayesian network.

Consider a joint probability with N variables, where the Markov property is satisfied:

$$p(x_1, \ldots, x_N) = p(x_N|x_{N-1}) \ldots p(x_2|x_1)p(x_1). \tag{4.2}$$

This joint probability, is depicted in Figure 4.2. The marginal distribution $p(x_n)$ is calculated as

$$p(x_n) = \sum_{x_1} \sum_{x_2} \cdots \sum_{x_{n-1}} p(x_1, \ldots, x_N). \tag{4.3}$$
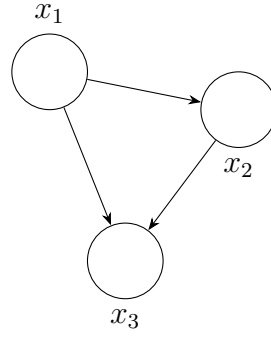
Figure 4.1. Directed, acyclic Bayesian network depicting the joint distribution $p(x_1, x_2, x_3)$.

When calculating the marginal distribution as in (4.3), the joint distribution is evaluated first, followed by the summations. This results in computational costs that scale exponentially with N. Thus, an alternative representation of (4.3) is necessary for large N. This is found using the product rule of probabilities along with the Markov property:

$$p(x_n) = \sum_{x_1} \cdots \sum_{x_{n-1}} p(x_1)p(x_2|x_1)p(x_3|x_2) \cdots p(x_n|x_{n-1}). \tag{4.4}$$

While this does not directly influence the computational cost, it enables the use of local calculations instead of global calculations. For instance, only the last term is dependent on x_{n-1}, the summation over x_{n-1} simplifies to:

$$\sum_{x_{n-1}} p(x_n|x_{n-1}). \tag{4.5}$$

This is repeated for each summation, where each summation results in a function of the next variable, such that the summation over x_{n-1} results in a function of x_{n-2} and so on. Thus, the marginal distribution can now be written as

$$p(x_n) = \underbrace{\sum_{x_{n-1}} p(x_n|x_{n-1}) \cdots \sum_{x_2} p(x_3|x_2) \sum_{x_1} p(x_2|x_1)p(x_1)}_{\varepsilon_{\mathrm{msg}}(x_n)}, \tag{4.6}$$

where $\varepsilon_{\mathrm{msg}}(x_n)$ is the message containing information passed from preceding nodes. Each node has their own message $\varepsilon_{\mathrm{msg}}(\cdot)$, making it possible to evaluate the messages recursively, where the first message $\varepsilon_{\mathrm{msg}}(x_2)$ is evaluated followed by the succeeding messages.

4.1.2 Variational Message Passing

Consider a Bayesian network where all parameters are given prior distributions. The network may have latent variables and parameters collectively denoted by ϕ, while the set of observed variables is denoted by $\boldsymbol{Z}$. The probabilistic model specifies a joint distribution given as $p(\boldsymbol{Z}, \phi)$, and the distribution of interest is the posterior distribution $p(\phi|\boldsymbol{Z})$. As this posterior distribution
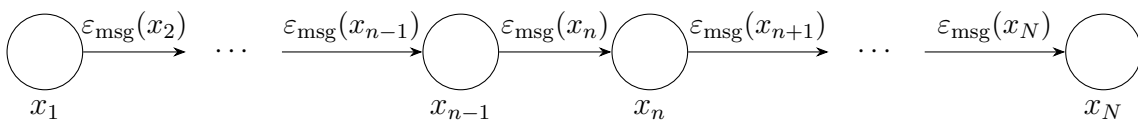
Figure 4.2. Directed, acyclic Bayesian network depicting the joint distribution $p(x_1, \ldots, x_N)$, where $\varepsilon_{\mathrm{msg}}$ is the information sent to the next node.

often is intractable, the goal of the method is to approximate it. Furthermore, the marginal distribution, given as

$$p(\mathbf{Z}) = \int p(\mathbf{Z}, \boldsymbol{\phi}) \, \mathrm{d}\boldsymbol{\phi}, \tag{4.7}$$

is also of interest. However, it is assumed that optimisation of the marginal distribution $p(\mathbf{Z})$ is difficult and optimisation of the joint distribution $p(\mathbf{Z}, \boldsymbol{\phi})$ is much easier. A proper distribution $q(\boldsymbol{\phi})$ is now introduced, where this is used as a surrogate function for the true posterior. For any $q(\boldsymbol{\phi})$, the following decomposition of the log marginal probability holds true:

$$\ln\left(p(\mathbf{Z})\right) = \mathcal{L}(q) + \mathrm{D}_{\mathrm{KL}}(q||p), \tag{4.8}$$

where $\mathrm{D}_{\mathrm{KL}}(q||p)$ is the Kullback-Leibler (KL) divergence between the posterior distribution $p(\boldsymbol{\phi}|\mathbf{Z})$ and the surrogate function $q(\boldsymbol{\phi})$, defined as

$$\mathrm{D}_{\mathrm{KL}} = -\int q(\boldsymbol{\phi}) \ln\left(\frac{p(\boldsymbol{\phi}|\mathbf{Z})}{q(\boldsymbol{\phi})}\right) \mathrm{d}\boldsymbol{\phi}, \tag{4.9}$$

and $\mathcal{L}(q)$ is given as

$$\mathcal{L}(q) = \int q(\boldsymbol{\phi}) \ln\left(\frac{p(\mathbf{Z}, \boldsymbol{\phi})}{q(\boldsymbol{\phi})}\right) \mathrm{d}\boldsymbol{\phi}. \tag{4.10}$$

The decomposition in (4.8) can be explained by examining (4.10). Using the definition of conditional probability, the log joint probability distribution is rewritten as

$$\ln(p(\mathbf{Z}, \boldsymbol{\phi})) = \ln(p(\boldsymbol{\phi}|\mathbf{Z})p(\mathbf{Z})) \tag{4.11}$$

$$= \ln(p(\boldsymbol{\phi}|\mathbf{Z})) + \ln(p(\mathbf{Z})). \tag{4.12}$$

Inserting (4.12) into (4.10) yields

$$\mathcal{L}(q) = \int q(\boldsymbol{\phi})\left(\ln\left(\frac{p(\boldsymbol{\phi}|\mathbf{Z})}{q(\boldsymbol{\phi})}\right) + \ln(p(\mathbf{Z}))\right)\mathrm{d}\boldsymbol{\phi} = \underbrace{\int q(\boldsymbol{\phi}) \ln\left(\frac{p(\boldsymbol{\phi}|\mathbf{Z})}{q(\boldsymbol{\phi})}\right)\mathrm{d}\boldsymbol{\phi}}_{=-\mathrm{D}_{\mathrm{KL}}(q||p)} + \ln(p(\mathbf{Z}))\underbrace{\int q(\boldsymbol{\phi})\,\mathrm{d}\boldsymbol{\phi}}_{=1}. \tag{4.13}$$

When inserting (4.13) into (4.8), it is seen that the first term cancels out KL divergence while the second term equals the log marginal probability $\ln(p(\mathbf{z}))$ as $q(\boldsymbol{\phi})$ is a proper probability distribution. It is known that the KL divergence only satisfies $\mathrm{D}_{\mathrm{KL}}(q||p) = 0$, if $q(\boldsymbol{\phi}) = p(\boldsymbol{\phi}|\mathbf{Z})$, thus $\mathcal{L}(q) \leq \ln(p(\mathbf{Z}))$, meaning $\mathcal{L}(q)$ is a lower bound on $\ln(p(\mathbf{Z}))$.

As the true posterior of a model is often intractable, a restricted family of distributions for which the lower bound $\mathcal{L}(q)$ is maximised is considered. This corresponds to minimising the KL divergence between the surrogate function $q(\boldsymbol{\phi})$ and the true posterior $p(\boldsymbol{\phi}|\mathbf{Z})$. Furthermore, the surrogate functions $q(\boldsymbol{\phi})$ needs to be tractable, hence it is desired to restrict the family sufficiently such that they comprise only tractable distributions. To achieve this, the mean field approximation is commonly applied.

4.1.2.1   Mean Field Approximation

A common family of distributions $q(\boldsymbol{\phi})$ is the set of fully factorised functions, where

$$q(\boldsymbol{\phi}) = \prod_{i=1}^{N} q_i(\boldsymbol{\phi}_i). \tag{4.14}$$

The elements of $\boldsymbol{\phi}$ have been partitioned into disjoint groups denoted $\boldsymbol{\phi}_i$ for $i = 1, \ldots, N$. Using this family of distributions leads to the method known as the mean field approximation. The general idea is to consider all distributions $q(\boldsymbol{\phi})$ on the form in (4.14), and then choose the one for which the lower bound $\mathcal{L}(q)$ is largest. For this purpose, a free form variational optimisation of $\mathcal{L}(q)$ with regard to all the distributions $q_i(\boldsymbol{\phi}_i)$ will be performed by optimising with respect to each of the factors, one at a time.

First, (4.14) is substituted into (4.10):

$$\mathcal{L}(q) = \int \prod_{i=1}^{N} q_i(\boldsymbol{\phi}_i) \ln\left(\frac{p(\boldsymbol{Z}, \boldsymbol{\phi})}{\prod_{i'=1}^{N} q_{i'}(\boldsymbol{\phi}_{i'})} \right) \mathrm{d}\boldsymbol{\phi}. \tag{4.15}$$

Next, the dependence of $q_j(\boldsymbol{\phi}_j)$ is pulled out of the first product as it is desired to obtain an optimisation expression for one factor $q_j(\boldsymbol{\phi}_j)$. Thus,

$$\mathcal{L}(q) = \int q_j(\boldsymbol{\phi}_j) \prod_{i \neq j}^{N} q_i(\boldsymbol{\phi}_i) \ln\left(\frac{p(\boldsymbol{Z}, \boldsymbol{\phi})}{\prod_{i'=1}^{N} q_{i'}(\boldsymbol{\phi}_{i'})} \right) \mathrm{d}\boldsymbol{\phi} \tag{4.16}$$

$$= \int q_j(\boldsymbol{\phi}_j) \left(\prod_{i \neq j}^{N} q_i(\boldsymbol{\phi}_i) \ln(p(\boldsymbol{Z}, \boldsymbol{\phi})) - \prod_{i \neq j}^{N} q_i(\boldsymbol{\phi}_i) \sum_{i'}^{N} \ln(q_{i'}(\boldsymbol{\phi}_{i'})) \right) \mathrm{d}\boldsymbol{\phi}. \tag{4.17}$$

The integral is split up and converted into a double integral, to integrate over $\boldsymbol{\phi}_i$ and $\boldsymbol{\phi}_j$:

$$\mathcal{L}(q) = \int q_j(\boldsymbol{\phi}_j) \underbrace{\left(\int \ln(p(\boldsymbol{Z}, \boldsymbol{\phi})) \prod_{i \neq j}^{N} q_i(\boldsymbol{\phi}_i) \, \mathrm{d}\boldsymbol{\phi}_i \right)}_{\ln(\widetilde{p}(\boldsymbol{Z}, \boldsymbol{\phi}_j))} \mathrm{d}\boldsymbol{\phi}_j - \int q_j(\boldsymbol{\phi}_j) \ln(q_j(\boldsymbol{\phi}_j)) \, \mathrm{d}\boldsymbol{\phi}_j$$

$$+ \int \prod_{i \neq j}^{N} q_i(\boldsymbol{\phi}_i) \sum_{i' \neq j}^{N} \ln(q_{i'}(\boldsymbol{\phi}_{i'})) \, \mathrm{d}\boldsymbol{\phi}_i. \tag{4.18}$$

In (4.18), $\ln(\widetilde{p}(\boldsymbol{Z}, \boldsymbol{\phi}_j))$ is written as

$$\ln(\widetilde{p}(\boldsymbol{Z}, \boldsymbol{\phi}_j)) = \underset{i \neq j}{\mathbb{E}} [\ln(p(\boldsymbol{Z}, \boldsymbol{\phi}_i))] + \text{constant}, \tag{4.19}$$

where $\underset{i \neq j}{\mathbb{E}}$ is the expected value over all variables $\boldsymbol{Z}$ except Z_i. Note that the last term in (4.18) is constant, thus,

$$\mathcal{L}(q) = \int q_j(\boldsymbol{\phi}_j) \ln(\widetilde{p}(\boldsymbol{Z}, \boldsymbol{\phi}_j) \, \mathrm{d}\boldsymbol{\phi}_j - \int q_j(\boldsymbol{\phi}_j) \ln(q_j(\boldsymbol{\phi}_j)) \, \mathrm{d}\boldsymbol{\phi}_j + \text{constant} \tag{4.20}$$

$$= \int q_j(\boldsymbol{\phi}_j) \left(\ln\left(\frac{\widetilde{p}(\boldsymbol{Z}, \boldsymbol{\phi}_j)}{q_j(\boldsymbol{\phi}_j)} \right) \right) \mathrm{d}\boldsymbol{\phi}_j + \text{constant} \tag{4.21}$$

$$= -\mathrm{D}_{\mathrm{KL}}(q||\widetilde{p}), \tag{4.22}$$

for the set of fully factorised functions. This means that maximising the lower bound is equivalent to minimising the KL divergence between $\widetilde{p}(\boldsymbol{Z}, \boldsymbol{\phi}_j)$ and $q_j(\boldsymbol{\phi}_j)$. From the definition of the KL

divergence, it is known that the minimum of (4.22) occurs when $q_j(\boldsymbol{\phi}_j) = \widetilde{p}(\boldsymbol{Z}, \boldsymbol{\phi}_j)$, thus an optimal solution is given by

$$\ln(q_j^{\star}(\boldsymbol{\phi}_j)) = \underset{i \neq j}{\mathbb{E}}[\ln(p(\boldsymbol{Z}, \boldsymbol{\phi}_i))] + \text{constant}. \tag{4.23}$$

The expression in (4.23) is iteratively solved for each variable $q_j(\boldsymbol{\phi}_j)$.

By combining variational message passing with the mean field approximation, an approach for approximating the posterior distributions of the parameters of interest has been obtained.

4.2 Parameter Estimation using Variational Message Passing

The concepts of variational message passing and the mean field approximation is now applied to the problem of jointly estimating all $\boldsymbol{\phi}_0, \boldsymbol{\phi}_1, \ldots, \boldsymbol{\phi}_n$ and $\boldsymbol{\Gamma}_0^{(k)}, \boldsymbol{\Gamma}_1^{(k)}, \ldots, \boldsymbol{\Gamma}_n^{(k)}$ for $k = 1, \ldots N_{\text{radar}}$ in a system with multiple MIMO FMCW radars. These parameters will be estimated for one target in a clutter environment using the observations $\boldsymbol{Z}_{0:n}^{1:N_{\text{radar}}}$ from (3.69), representing the first n MIMO cycles for each radar, where $n = 0, 1, \ldots, N$. To ease notation, $\boldsymbol{Z}_{0:n}^{1:N_{\text{radar}}} = \boldsymbol{Z}_0^{(1)}, \ldots, \boldsymbol{Z}_n^{(1)}, \ldots, \boldsymbol{Z}_0^{(N_{\text{radar}})}, \ldots, \boldsymbol{Z}_n^{(N_{\text{radar}})}$ and likewise for $\boldsymbol{\phi}_{0:n}$ and $\boldsymbol{\Gamma}_{0:n}^{1:N_{\text{radar}}}$. The MRBLaT algorithm presented in [Kitchen et al., 2025] will be utilised for the target parameter estimation along with the clutter field estimation presented in [Westerkam and Pedersen, 2025]. The goal is to combine the clutter tracking algorithm with the MRBLaT algorithm.

4.2.1 Local or Global Clutter Field Framework

In a multi-radar setup, the clutter field can be modelled either as a global or a local clutter field. For the global clutter field, all radars jointly estimate one common clutter field from different perspectives, meaning that $\boldsymbol{\Gamma}_n^{(k)}$ is the same for all radars. For the local clutter field each radar independently estimate their own individual clutter field.

Both approaches has its advantages and disadvantages. The Bayesian network for the global clutter field can be seen in Figure 4.3. Using a global clutter field ensures a common interpretation of it, leading to a potentially more accurate joint estimation. Another advantage is that fewer parameters needs to be estimated. A disadvantage for a global clutter field is that information about $\boldsymbol{\Gamma}_{0:n}$ must be exchanged between the radars, which either requires centralised processing or sending very large data vectors between the radars. Both cases will likely cause the computational complexity to increase. Furthermore, blind spots can cause discrepancies between radars, as one radar may detect objects that are obstructed from another's view.

The Bayesian network for the local clutter field can be seen in Figure 4.4. For local clutter fields, one advantage is that no data needs to be exchanged between the radars since the parameters are estimated independently for each radar. Additionally, the clutter field is then independent of the geometry and position of the radar. Lastly, local estimation can better account for varying terrain and obstructions specific to each radar. The disadvantages of a local clutter field are that more parameters must be estimated and that there is no shared interpretation of the clutter environment across radars.

We have chosen to use the local clutter field setting, due to its advantages on decentralised parameter estimation and to avoid discrepancies among radars regarding whether or not there is an object present. Furthermore, by having local clutter fields both the target tracking and
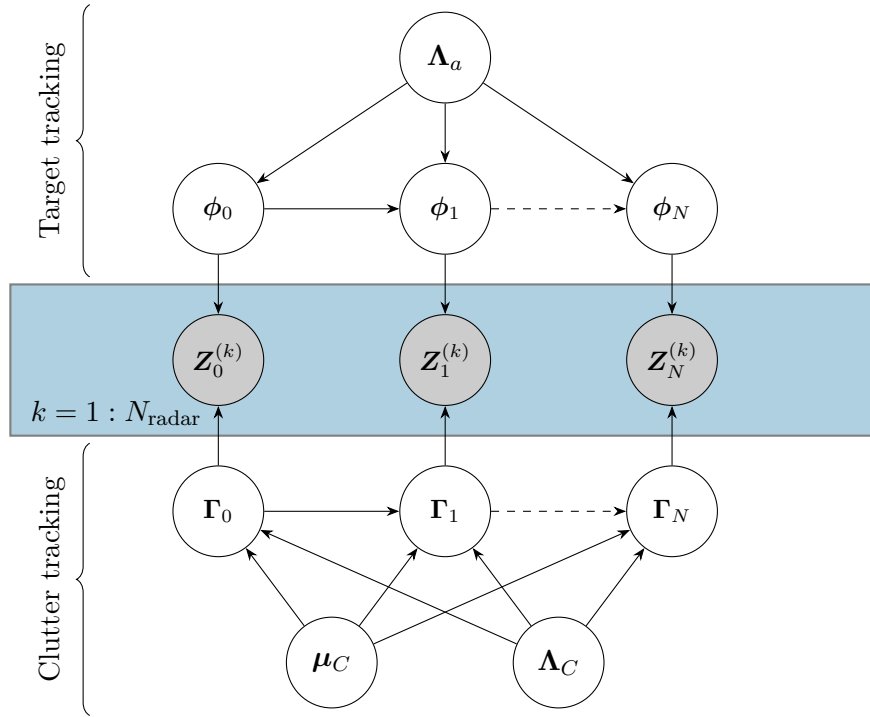
Figure 4.3. The Bayesian network for target and clutter tracking using a global clutter field. The observed variables are marked with grey.
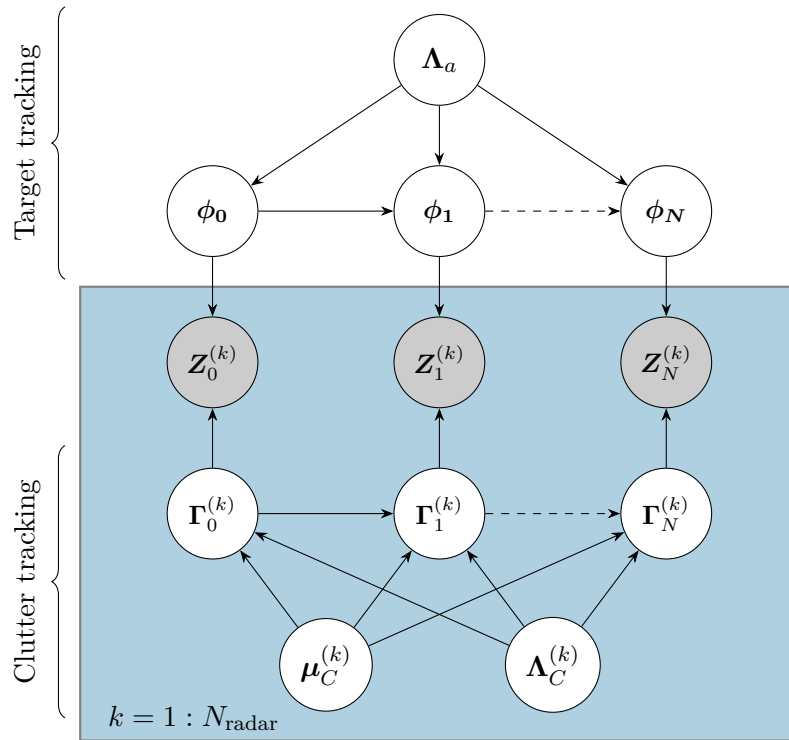

Figure 4.4. The Bayesian network for target and clutter tracking using a local clutter field. The observed variables are marked with grey.

clutter tracking are distributed algorithms. Thus, the rest of the parameter estimation will be carried out using a local clutter field approach.

It is assumed that the target follows a kinematic model with mean $\boldsymbol{\mu}_a = 0$ and precision matrix $\boldsymbol{\Lambda}_a$ as described in [Kitchen et al., 2025]. Furthermore, it is assumed that $\boldsymbol{\Gamma}_n^{(k)}|\boldsymbol{\mu}_C^{(k)}, \boldsymbol{\Lambda}_C^{(k)} \sim \mathcal{N}^C(\boldsymbol{\mu}_C^{(k)}, \boldsymbol{\Lambda}_C^{(k)})$ and that $\boldsymbol{\Gamma}_n^{(k)}|\boldsymbol{\mu}_C^{(k)}, \boldsymbol{\Lambda}_C^{(k)}, \boldsymbol{\Gamma}_{n-1}^{(k)}$ form a Markov process with mean $\boldsymbol{\mu}_C^{(k)}$ and precision matrix $\boldsymbol{\Lambda}_C^{(k)}$:

$$\boldsymbol{\Gamma}_n^{(k)} = \kappa\boldsymbol{\Gamma}_{n-1}^{(k)} + \boldsymbol{V}_N^{(k)}, \tag{4.24}$$

where $\boldsymbol{V}_N^{(k)} \sim \mathcal{N}^C(\boldsymbol{\mu}_V^{(k)}, \boldsymbol{\Lambda}_V^{(k)})$ is the process noise and $\kappa =]0, 1[$ is a scaling factor. Note that the clutter field is complex Gaussian as the expansion coefficients are complex Gaussian. Assuming that $\boldsymbol{\Gamma}_n^{(k)}|\boldsymbol{\mu}_C^{(k)}, \boldsymbol{\Lambda}_C^{(k)}$ is wide sense stationary, the mean and precision of the noise are

$$\boldsymbol{\mu}_V^{(k)} = \boldsymbol{\mu}_C^{(k)}(1 - \kappa), \qquad \boldsymbol{\Lambda}_V^{(k)} = \frac{\boldsymbol{\Lambda}_C^{(k)}}{1 - \kappa^2}. \tag{4.25}$$

This comes from the fact that the mean for the Markov process is given as

$$\boldsymbol{\mu}_C^{(k)} = \kappa\boldsymbol{\mu}_C^{(k)} + \boldsymbol{\mu}_V^{(k)}, \tag{4.26}$$

and the covariance is given as

$$\left(\boldsymbol{\Lambda}_C^{(k)}\right)^{-1} = \kappa^2\left(\boldsymbol{\Lambda}_C^{(k)}\right)^{-1} + \left(\boldsymbol{\Lambda}_V^{(k)}\right)^{-1}. \tag{4.27}$$

4.2.2 Parameter Estimation using a Local Clutter Field

The dependencies of the target parameters and the clutter parameters, illustrated in Figure 4.4, are modelled as a Markov process, which yields a joint density function of the unknown parameters and the data:

$$p\Big(\boldsymbol{Z}_{0:N}^{1:N_{\text{radar}}}, \boldsymbol{\phi}_{0:N}, \boldsymbol{\Gamma}_{0:N}^{1:N_{\text{radar}}}, \boldsymbol{\Lambda}_a, \boldsymbol{\mu}_C^{1:N_{\text{radar}}}, \boldsymbol{\Lambda}_C^{1:N_{\text{radar}}}\Big)$$

$$= p(\boldsymbol{\phi}_0|\boldsymbol{\Lambda}_a)p(\boldsymbol{\Lambda}_a)\prod_{n=0}^{N}\left(\prod_{k=1}^{N_{\text{radar}}}p\Big(\boldsymbol{Z}_n^{(k)}\Big|\boldsymbol{\phi}_n, \boldsymbol{\Gamma}_n^{(k)}\Big)\right)$$

$$\times\prod_{n'=1}^{N}p(\boldsymbol{\phi}_{n'}|\boldsymbol{\phi}_{n'-1}, \boldsymbol{\Lambda}_a)\left(\prod_{k'=1}^{N_{\text{radar}}}p\Big(\boldsymbol{\Lambda}_C^{(k')}\Big)p\Big(\boldsymbol{\mu}_C^{(k')}\Big)p\Big(\boldsymbol{\Gamma}_0^{(k')}\Big|\boldsymbol{\mu}_C^{(k')}, \boldsymbol{\Lambda}_C^{(k')}\Big)p\Big(\boldsymbol{\Gamma}_{n'}^{(k')}\Big|\boldsymbol{\Gamma}_{n'-1}^{(k')}, \boldsymbol{\mu}_C^{(k')}, \boldsymbol{\Lambda}_C^{(k')}\Big)\right).$$

$$\tag{4.28}$$

Here, $\boldsymbol{\Lambda}_a$ and $\boldsymbol{\Lambda}_C^{(k)}$ are the precision matrix of the target's acceleration and clutter field according to radar k, respectively, and $\boldsymbol{\mu}_C^{(k)}$ is the mean of the clutter field according to radar k. Note that the variance of $p(\boldsymbol{\phi}_0|\boldsymbol{\Lambda}_a)$ will tend to infinity for any stationary solution, thus an improper distribution is chosen such that $p(\boldsymbol{\phi}_0|\boldsymbol{\Lambda}_a) = 1$.

As the goal is to estimate $\boldsymbol{\phi}_{0:N}$ and $\boldsymbol{\Gamma}_{0:N}^{1:N_{\text{radar}}}$ based on the data $\boldsymbol{Z}_{0:N}^{1:N_{\text{radar}}}$, the posterior distributions $p\Big(\boldsymbol{\phi}_n|\boldsymbol{Z}_{0:n}^{1:N_{\text{radar}}}, \boldsymbol{\Lambda}_a\Big)$ and $p\Big(\boldsymbol{\Gamma}_n^{(k)}|\boldsymbol{Z}_{0:n}^{1:N_{\text{radar}}}, \boldsymbol{\mu}_C^{1:N_{\text{radar}}}, \boldsymbol{\Lambda}_C^{1:N_{\text{radar}}}\Big)$ are examined. However, these posteriors are intractable, thus the mean field approach is used to approximate the joint posterior with surrogate functions:

$$\prod_{k=1}^{N_{\text{radar}}}q\Big(\boldsymbol{\phi}_{0:N}, \boldsymbol{\Gamma}_{0:N}^{(k)}, \boldsymbol{\Lambda}_a, \boldsymbol{\mu}_C^{(k)}, \boldsymbol{\Lambda}_C^{(k)}\Big) = q(\boldsymbol{\Lambda}_a)\prod_{k=1}^{N_{\text{radar}}}q\Big(\boldsymbol{\mu}_C^{(k)}\Big)q\Big(\boldsymbol{\Lambda}_C^{(k)}\Big)\prod_{n=0}^{N}q(\boldsymbol{\phi}_n)q\Big(\boldsymbol{\Gamma}_n^{(k)}\Big). \tag{4.29}$$

These are obtained by minimising the KL divergence with regards to the true posterior.

Target Tracking

An expression for the posterior of the target parameters is derived first. From [Kitchen et al., 2025], the two surrogate functions from (4.29) related to the target are written as

$$
\ln(q(\boldsymbol{\phi}_n)) = \sum_{k=1}^{N_{\text{radar}}} \ln\left(p\left(\boldsymbol{Z}_n^{(k)} \middle| \boldsymbol{\phi}_n, \boldsymbol{\Gamma}_n^{(k)} \right) \right) + \underset{\backslash \boldsymbol{\phi}_n}{\mathbb{E}} \left[\ln(p(\boldsymbol{\phi}_n|\boldsymbol{\phi}_{n-1}, \boldsymbol{\Lambda}_a)) \right]
$$
$$
+ \underset{\backslash \boldsymbol{\phi}_n}{\mathbb{E}} \left[\ln(p(\boldsymbol{\phi}_{n+1}|\boldsymbol{\phi}_n, \boldsymbol{\Lambda}_a)) \right] + \text{constant}, \quad (4.30)
$$

and

$$
\ln(q(\boldsymbol{\Lambda}_a)) = \sum_{n=1}^{N} \underset{\backslash \boldsymbol{\Lambda}_a}{\mathbb{E}} \left[\ln(p(\boldsymbol{\phi}_n|\boldsymbol{\phi}_{n-1}, \boldsymbol{\Lambda}_a)) \right] + \ln(p(\boldsymbol{\Lambda}_a)) + \text{constant}, \quad (4.31)
$$

where each of the terms in the surrogate functions is viewed as a message. Note that while the messages are derived for each radar, the expressions for the messages are the same for all radars and the superscript (k) is therefore omitted. The messages that are derived for the target are:

1. $\varepsilon^{(\boldsymbol{Z}_n \to \boldsymbol{\phi}_n)}$ from (4.30).
2. $\varepsilon^{(\boldsymbol{\phi}_{n-1} \to \boldsymbol{\phi}_n)}$ from (4.30).
3. $\varepsilon^{(\boldsymbol{\phi}_{n+1} \to \boldsymbol{\phi}_n)}$ from (4.30).
4. $\varepsilon^{(\boldsymbol{\Lambda}_a \to \boldsymbol{\phi}_n)}$ from (4.31).

The derivations of **the second and third message** are found in Section B.1.

The first message is now derived, where $\varepsilon^{(\boldsymbol{Z}_n \to \boldsymbol{\phi}_n)}$ is expanded as

$$
\underset{\backslash \boldsymbol{\phi}_n}{\mathbb{E}} \left[\ln(p(\boldsymbol{Z}_n|\boldsymbol{\phi}_n, \boldsymbol{\Gamma}_n)) \right] \propto - \underset{\backslash \boldsymbol{\phi}_n}{\mathbb{E}} \left[\left(\underbrace{\boldsymbol{Z}_n - \boldsymbol{M}\boldsymbol{\Gamma}_n}_{\acute{\boldsymbol{Z}}_n} - \boldsymbol{S}(\boldsymbol{\phi}_n) \right)^\dagger \boldsymbol{\Lambda}_Z \left(\underbrace{\boldsymbol{Z}_n - \boldsymbol{M}\boldsymbol{\Gamma}_n}_{\acute{\boldsymbol{Z}}_n} - \boldsymbol{S}(\boldsymbol{\phi}_n) \right) \right] \quad (4.32)
$$

$$
= - \underbrace{\underset{\backslash \boldsymbol{\phi}_n}{\mathbb{E}} \left[\acute{\boldsymbol{Z}}_n^\dagger \boldsymbol{\Lambda}_Z \acute{\boldsymbol{Z}}_n \right]}_{\text{constant}} - \underset{\backslash \boldsymbol{\phi}_n}{\mathbb{E}} \left[\boldsymbol{S}(\boldsymbol{\phi}_n)^\dagger \boldsymbol{\Lambda}_Z \boldsymbol{S}(\boldsymbol{\phi}_n) \right]
$$
$$
+ 2\mathrm{Re}\left(\underset{\backslash \boldsymbol{\phi}_n}{\mathbb{E}} \left[\acute{\boldsymbol{Z}}^\dagger \boldsymbol{\Lambda}_Z \boldsymbol{S}(\boldsymbol{\phi}_n) \right] \right) \quad (4.33)
$$

$$
= - \boldsymbol{S}(\boldsymbol{\phi}_n)^\dagger \boldsymbol{\Lambda}_Z \boldsymbol{S}(\boldsymbol{\phi}_n) + 2\mathrm{Re}\left(\underset{\backslash \boldsymbol{\phi}_n}{\mathbb{E}} \left[\acute{\boldsymbol{Z}}^\dagger \boldsymbol{\Lambda}_Z \boldsymbol{S}(\boldsymbol{\phi}_n) \right] \right) - \text{constant} \quad (4.34)
$$

$$
= - \left(\underset{\backslash \boldsymbol{\phi}_n}{\mathbb{E}} \left[\acute{\boldsymbol{Z}}_n \right] - \boldsymbol{S}(\boldsymbol{\phi}_n) \right)^\dagger \boldsymbol{\Lambda}_Z \left(\underset{\backslash \boldsymbol{\phi}_n}{\mathbb{E}} \left[\acute{\boldsymbol{Z}}_n \right] - \boldsymbol{S}(\boldsymbol{\phi}_n) \right) - \text{constant}. \quad (4.35)
$$

Here,

$$
\underset{\backslash \boldsymbol{\phi}_n}{\mathbb{E}} \left[\acute{\boldsymbol{Z}}_n \right] = \boldsymbol{Z}_n - \boldsymbol{M}\overline{\boldsymbol{\Gamma}}_n = \check{\boldsymbol{Z}}_n, \quad (4.36)
$$

where $\bar{\cdot}$ denotes the mean, and $\check{\boldsymbol{Z}}_n$ shows that when the target parameters are estimated, the mean of the clutter field $\overline{\boldsymbol{\Gamma}}_n$ is subtracted. This attempts to suppress the interference from the clutter environment through mutual interference cancellation. Since (4.35) is not recognised as any known distribution in $\boldsymbol{\phi}_n$, it is desired to estimate the message by a Gaussian distribution:

$$
\varepsilon^{(\boldsymbol{Z}_n \to \boldsymbol{\phi}_n)} = \mathcal{N}^C\left(\overline{\varepsilon}^{(\boldsymbol{Z}_n \to \boldsymbol{\phi}_n)}, \left(\overline{\overline{\varepsilon}}^{(\boldsymbol{Z}_n \to \boldsymbol{\phi}_n)} \right)^{-1} \right), \quad (4.37)
$$

where $\overline{\overline{\cdot}}$ denotes the covariance matrix. The optimal approximation of the message is obtained by minimising the KL divergence between $\varepsilon^{(\boldsymbol{Z}_n \to \phi_n)}$ and a Gaussian distribution in ϕ_n:

$$\left\{ \widehat{\overline{\varepsilon}}^{(\boldsymbol{Z}_n \to \phi_n)}, \widehat{\overline{\overline{\varepsilon}}}^{(\boldsymbol{Z}_n \to \phi_n)} \right\} = \arg\min_{\overline{\varepsilon}, \overline{\overline{\varepsilon}}} D_{KL}\Big(\mathcal{N}^C\big(\phi_n; \overline{\varepsilon}, \overline{\overline{\varepsilon}}^{-1} \big) \Big\| \varepsilon^{(\boldsymbol{Z}_n \to \phi_n)} \Big), \tag{4.38}$$

where

$$D_{KL}\Big(\mathcal{N}^C\big(\phi_n; \overline{\varepsilon}, \overline{\overline{\varepsilon}}^{-1} \big) \Big\| \varepsilon^{(\boldsymbol{Z}_n \to \phi_n)} \Big)$$
$$= -\int_{\phi_n} \mathcal{N}^C\big(\overline{\varepsilon}, \overline{\overline{\varepsilon}}^{-1} \big) \ln\big(\varepsilon^{(\boldsymbol{Z}_n \to \phi_n)} \big) \, d\phi_n + \int_{\phi_n} \mathcal{N}^C\big(\overline{\varepsilon}, \overline{\overline{\varepsilon}}^{-1} \big) \ln\big(\mathcal{N}^C\big(\overline{\varepsilon}, \overline{\overline{\varepsilon}}^{-1} \big) \big) \, d\phi_n. \tag{4.39}$$

Here, the second term is the entropy of a Gaussian distribution, denoted by $\zeta(\overline{\overline{\varepsilon}})$, and the first term is the expectation of $\ln(\varepsilon^{(\boldsymbol{Z}_n \to \phi_n)})$ with regards to the Gaussian distribution $\mathcal{N}^C\big(\overline{\varepsilon}, \overline{\overline{\varepsilon}}^{-1} \big)$. As (4.38) is difficult to optimise numerically, the first term is (4.39) is rewritten as

$$\mathbb{E}_{\phi_n}\Big[\Big(\big(\boldsymbol{S}_n(\phi_n) - \check{\boldsymbol{Z}}_n \big)^\dagger \boldsymbol{\Lambda}_Z \big(\boldsymbol{S}_n(\phi_n) - \check{\boldsymbol{Z}}_n \big) \Big) \Big]$$
$$= \mathbb{E}_{\phi_n}\Big[\boldsymbol{S}_n(\phi_n)^\dagger \boldsymbol{\Lambda}_Z \boldsymbol{S}_n(\phi_n) \Big] - \check{\boldsymbol{Z}}_n^\dagger \boldsymbol{\Lambda}_Z \mathbb{E}_{\phi_n}[\boldsymbol{S}_n(\phi_n)] - \mathbb{E}_{\phi_n}\Big[\boldsymbol{S}_n(\phi_n)^\dagger \Big] \boldsymbol{\Lambda}_Z \check{\boldsymbol{Z}}_n + \check{\boldsymbol{Z}}_n^\dagger \boldsymbol{\Lambda}_Z \check{\boldsymbol{Z}}_n, \tag{4.40}$$

where

$$\mathbb{E}_{\phi_n}\Big[\boldsymbol{S}_n(\phi_n)^\dagger \boldsymbol{\Lambda}_Z \boldsymbol{S}_n(\phi_n) \Big] = \mathbb{E}_{\phi_n}\Big[\mathrm{tr}\Big(\boldsymbol{S}_n(\phi_n)^\dagger \boldsymbol{\Lambda}_Z \boldsymbol{S}_n(\phi_n) \Big) \Big] \tag{4.41}$$
$$= \mathbb{E}_{\phi_n}\Big[\mathrm{tr}\Big(\boldsymbol{S}_n(\phi_n) \boldsymbol{S}_n(\phi_n)^\dagger \boldsymbol{\Lambda}_Z \Big) \Big] \tag{4.42}$$
$$= \mathrm{tr}\Big(\mathbb{E}_{\phi_n}\Big[\boldsymbol{S}_n(\phi_n) \boldsymbol{S}_n(\phi_n)^\dagger \Big] \boldsymbol{\Lambda}_Z \Big). \tag{4.43}$$

Inserting (4.43) in (4.40) yields

$$\mathbb{E}_{\phi_n}\Big[\Big(\big(\boldsymbol{S}_n(\phi_n) - \check{\boldsymbol{Z}}_n \big)^\dagger \boldsymbol{\Lambda}_Z \big(\boldsymbol{S}_n(\phi_n) - \check{\boldsymbol{Z}}_n \big) \Big) \Big]$$
$$= \mathrm{tr}\Big(\mathbb{E}_{\phi_n}\Big[\boldsymbol{S}_n(\phi_n) \boldsymbol{S}_n(\phi_n)^\dagger \Big] \boldsymbol{\Lambda}_Z \Big) - \check{\boldsymbol{Z}}_n^\dagger \boldsymbol{\Lambda}_Z \mathbb{E}_{\phi_n}[\boldsymbol{S}_n(\phi_n)] - \mathbb{E}_{\phi_n}\Big[\boldsymbol{S}_n(\phi_n)^\dagger \Big] \boldsymbol{\Lambda}_Z \check{\boldsymbol{Z}}_n + \check{\boldsymbol{Z}}_n^\dagger \boldsymbol{\Lambda}_Z \check{\boldsymbol{Z}}_n. \tag{4.44}$$

The expectations in (4.44) are intractable, therefore, the delta method [Zepeda-Tello et al., 2022] is utilised to approximate them. The calculation for this approximation is seen in Section B.2, yielding (B.29)

$$\mathbb{E}_{\phi_n}[\boldsymbol{S}_n(\phi_n)] \approx \boldsymbol{S}_n(\overline{\phi}_n), \tag{4.45}$$

and (B.35)

$$\mathbb{E}_{\phi_n}\Big[\boldsymbol{S}_n(\phi_n) \boldsymbol{S}_n(\phi_n)^\dagger \Big] \approx \boldsymbol{S}_n(\overline{\phi}_n) \boldsymbol{S}_n(\overline{\phi}_n)^\dagger + \nabla_{\phi_n} \boldsymbol{S}_n(\overline{\phi}_n) \overline{\overline{\phi}}_n \nabla_{\phi_n} \boldsymbol{S}_n(\overline{\phi}_n)^\dagger. \tag{4.46}$$

An expression for the KL divergence in (4.39) is obtained by inserting these approximations into (4.44):

$$D_{KL} \propto \mathrm{tr}\Big(\big(\boldsymbol{S}_n(\overline{\phi}_n) \boldsymbol{S}_n(\overline{\phi}_n)^\dagger + \nabla_{\phi_n} \boldsymbol{S}_n(\overline{\phi}_n) \overline{\overline{\phi}}_n \nabla_{\phi_n} \boldsymbol{S}_n(\overline{\phi}_n)^\dagger \big) \boldsymbol{\Lambda}_Z \Big)$$
$$- \check{\boldsymbol{Z}}_n^\dagger \boldsymbol{\Lambda}_Z \boldsymbol{S}_n(\overline{\phi}_n) - \boldsymbol{S}_n(\overline{\phi}_n)^\dagger \boldsymbol{\Lambda}_Z \check{\boldsymbol{Z}}_n + \check{\boldsymbol{Z}}_n^\dagger \boldsymbol{\Lambda}_Z \check{\boldsymbol{Z}}_n - \zeta(\overline{\overline{\phi}}_n) \tag{4.47}$$
$$= \boldsymbol{S}_n(\overline{\phi}_n)^\dagger \boldsymbol{\Lambda}_Z \boldsymbol{S}_n(\overline{\phi}_n) + \mathrm{tr}\Big(\overline{\overline{\phi}}_n \nabla_{\phi_n} \boldsymbol{S}_n(\overline{\phi}_n)^\dagger \boldsymbol{\Lambda}_Z \nabla_{\phi_n} \boldsymbol{S}_n(\overline{\phi}_n) \Big)$$
$$- 2\mathrm{Re}\Big(\big(\boldsymbol{S}_n(\overline{\phi}_n) - \check{\boldsymbol{Z}}_n \big)^\dagger \boldsymbol{\Lambda}_Z \big(\check{\boldsymbol{Z}}_n - \boldsymbol{S}_n(\overline{\phi}_n) \big) \Big) - \zeta(\overline{\overline{\phi}}_n). \tag{4.48}$$

Now, (4.48) can be numerically minimised in $\overline{\phi}_n$ and $\overline{\overline{\phi}}_n$.

An approximation of the path loss α is needed as it contains information about the reflectivity of the target. This will be done using a maximum likelihood estimate, using the mean of the previous target parameter $\overline{\phi}_{n-1}$:

$$\hat{\alpha} = \frac{S_n(\overline{\phi}_{n-1})^\dagger \Lambda_Z \check{Z}_n}{S_n(\overline{\phi}_{n-1})^\dagger \Lambda_Z S_n(\overline{\phi}_{n-1})}. \tag{4.49}$$

As mentioned in [Kitchen et al., 2025], the real operator in (4.48) causes instability and is therefore replaced by an absolute value. Thus the objective function becomes

$$\mathrm{D_{KL}} \propto -2\left|\hat{\alpha}\left(S_n(\overline{\phi}_n) - \check{Z}_n\right)^\dagger \Lambda_Z\left(\check{Z}_n - S_n(\overline{\phi}_n)\right)\right|$$
$$+ |\hat{\alpha}|^2 S_n(\overline{\phi}_n)^\dagger \Lambda_Z S_n(\overline{\phi}_n) + |\hat{\alpha}|^2 \mathrm{tr}\left(\overline{\overline{\phi}}_n \nabla_{\phi_n} S_n(\overline{\phi}_n)^\dagger \Lambda_Z \nabla_{\phi_n} S_n(\overline{\phi}_n)\right) - \zeta(\overline{\overline{\phi}}_n). \tag{4.50}$$

As the first three messages going to ϕ_n are described as multivariate complex Gaussian distributions, the surrogate function $q(\phi_n)$ is described as a product of these distributions:

$$q(\phi_n) = \mathcal{N}(\mu_{\mathrm{tot}}, \Lambda_{\mathrm{tot}}) = \prod_{n=0}^{N} \mathcal{N}(\mu_n, \Lambda_n) \tag{4.51}$$

where

$$\Lambda_{\mathrm{tot}}^{-1} = \sum_{n=0}^{N} \sum_{k=1}^{N_{\mathrm{radar}}} \overline{\overline{\varepsilon}}^{(\phi_{n-1} \to \phi_n)} + \overline{\overline{\varepsilon}}^{(\phi_{n+1} \to \phi_n)} + \overline{\overline{\varepsilon}}^{\left(Z_n^{(k)} \to \phi_n\right)} \tag{4.52}$$

is the total precision matrix, and

$$\mu_{\mathrm{tot}} = (\Lambda_{\mathrm{tot}})^{-1} \sum_{n=0}^{N} \left(\overline{\overline{\varepsilon}}^{(\phi_{n-1} \to \phi_n)} + \overline{\overline{\varepsilon}}^{(\phi_{n+1} \to \phi_n)} + \overline{\overline{\varepsilon}}^{(Z_n \to \phi_n)}\right)$$
$$\times \left(\overline{\varepsilon}^{(\phi_{n-1} \to \phi_n)} + \overline{\varepsilon}^{(\phi_{n+1} \to \phi_n)} + \overline{\varepsilon}^{(Z_n \to \phi_n)}\right) \tag{4.53}$$

is the total mean vector. Here, the precision matrices of the messages are given by (B.24), (B.27), and (4.50) and the means of the messages are given by (B.23), (B.26), and (4.50).

The fourth message $\varepsilon^{(\Lambda_a \to \phi_n)}$ is, by [Westerkam et al., 2025], written as

$$\exp\left(\sum_{n=1}^{N} \mathop{\mathbb{E}}_{\backslash \Lambda_a}\left[\ln(p(\phi_n|\phi_{n-1}, \Lambda_a))\right]\right) = \exp\left(-\frac{1}{2}\sum_{n=1}^{N} \mathrm{tr}\left(\Lambda_a \mathbb{V}_{n,n-1}^{(k)}\right)\right)|\Lambda_a|^{\frac{N}{2}}, \tag{4.54}$$

where

$$\mathbb{V}_{n,n-1}^{(k)} = \mathop{\mathbb{E}}_{\backslash \Lambda_a}\left[\left(\phi_n - T\overline{\phi}_{n-1}\right)\left(G^\top G\right)^{-1}\left(\phi_n - T\overline{\phi}_{n-1}\right)^\top\right]. \tag{4.55}$$

By using a factorised prior probability density function (pdf), that is $p(\Lambda_a^{(k)}) = \prod_{j=1}^{4} p(\Lambda_{a,j}^{(k)})$, the trace is written as

$$\mathrm{tr}\left(\Lambda_a^{(k)}, \mathbb{V}_{n,n-1}^{(k)}\right) = \sum_{j=1}^{4} \Lambda_{a,j}^{(k)}\left[\mathbb{V}_{n,n-1}^{(k)}\right]_{j,j}. \tag{4.56}$$

Inserting (4.56) in (4.54) results in

$$\exp\left(\sum_{n=1}^{N} \underset{\backslash \mathbf{\Lambda}_a}{\mathbb{E}}\left[\ln(p(\boldsymbol{\phi}_n|\boldsymbol{\phi}_{n-1}, \mathbf{\Lambda}_a))\right]\right) = \exp\left(-\frac{1}{2}\sum_{n=1}^{N}\sum_{j=1}^{4}\Lambda_{a,j}^{(k)}\left[\mathbb{V}_{n,n-1}^{(k)}\right]_{j,j}\right)|\mathbf{\Lambda}_a|^{\frac{N}{2}}, \qquad (4.57)$$

which is recognised as the functional form of a gamma distribution $\text{Gamma}(\mathcal{G}, \epsilon)$ with parameters $\mathcal{G} = N/2 + 1$ and $\epsilon = \frac{\sum_{n=1}^{N} \mathbb{V}_{n,n-1,j,j}^{(k)}}{2}$.

Clutter Tracking

The expression for the posterior for the clutter parameters are derived. The three surrogate functions that are related to the clutter parameters in (4.29) are

$$\ln\left(q\left(\mathbf{\Gamma}_n^{(k)}\right)\right) = \sum_{n=0}^{N}\ln\left(p\left(\mathbf{Z}_n^{(k)}|\boldsymbol{\phi}_n, \mathbf{\Gamma}_n^{(k)}\right)\right) + \underset{\backslash \mathbf{\Gamma}_n^{(k)}}{\mathbb{E}}\left[\ln\left(p\left(\mathbf{\Gamma}_n^{(k)}|\mathbf{\Gamma}_{n-1}^{(k)}, \boldsymbol{\mu}_C^{(k)}, \mathbf{\Lambda}_C^{(k)}\right)\right)\right]$$
$$+ \underset{\backslash \mathbf{\Gamma}_n^{(k)}}{\mathbb{E}}\left[\ln\left(p\left(\mathbf{\Gamma}_{n+1}^{(k)}|\mathbf{\Gamma}_n^{(k)}, \boldsymbol{\mu}_C^{(k)}, \mathbf{\Lambda}_C^{(k)}\right)\right)\right] + \text{constant}, \quad (4.58)$$

$$\ln\left(q\left(\boldsymbol{\mu}_C^{(k)}\right)\right) = \ln\left(p\left(\boldsymbol{\mu}_C^{(k)}\right)\right) + \sum_{n=0}^{N}\underset{\backslash \boldsymbol{\mu}_C^{(k)}}{\mathbb{E}}\left[\ln\left(p\left(\mathbf{\Gamma}_n^{(k)}|\mathbf{\Gamma}_{n-1}^{(k)}, \boldsymbol{\mu}_C^{(k)}, \mathbf{\Lambda}_C^{(k)}\right)\right)\right] + \text{constant}, \qquad (4.59)$$

and

$$\ln\left(q\left(\mathbf{\Lambda}_C^{(k)}\right)\right) = \ln\left(p\left(\mathbf{\Lambda}_C^{(k)}\right)\right) + \sum_{n=0}^{N}\underset{\backslash \mathbf{\Lambda}_C^{(k)}}{\mathbb{E}}\left[\ln\left(p\left(\mathbf{\Gamma}_n^{(k)}|\mathbf{\Gamma}_{n-1}^{(k)}, \boldsymbol{\mu}_C^{(k)}, \mathbf{\Lambda}_C^{(k)}\right)\right)\right] + \text{constant}. \qquad (4.60)$$

Once again, note that while the message is calculated for each radar, the expression for the message is the same for all radars, and the superscript (k) is therefore omitted. The messages that are derived for the clutter are:

1. $\varepsilon^{(\mathbf{\Gamma}_{n-1}\to\mathbf{\Gamma}_n)}$ from (4.58).
2. $\varepsilon^{(\mathbf{\Gamma}_{n+1}\to\mathbf{\Gamma}_n)}$ from (4.58).
3. $\varepsilon^{(\mathbf{Z}_n\to\mathbf{\Gamma}_n)}$ from (4.58).
4. $\varepsilon^{(\boldsymbol{\mu}_C\to\mathbf{\Gamma}_n)}$ from (4.59).
5. $\varepsilon^{(\mathbf{\Lambda}_C\to\mathbf{\Gamma}_n)}$ from (4.60).

The first message $\varepsilon^{(\mathbf{\Gamma}_{n-1}\to\mathbf{\Gamma}_n)}$ is derived, where

$$\ln\left(\varepsilon^{(\mathbf{\Gamma}_{n-1}\to\mathbf{\Gamma}_n)}\right) = \underset{\backslash \mathbf{\Gamma}_n}{\mathbb{E}}\left[\ln(p(\mathbf{\Gamma}_n|\mathbf{\Gamma}_{n-1}, \boldsymbol{\mu}_C, \mathbf{\Lambda}_C))\right]. \qquad (4.61)$$

By (4.24) and (4.25):

$$p(\mathbf{\Gamma}_n|\mathbf{\Gamma}_{n-1}, \boldsymbol{\mu}_C, \mathbf{\Lambda}_C) = \mathcal{N}^C\left(\underbrace{\kappa\mathbf{\Gamma}_{n-1} + \boldsymbol{\mu}_C(1-\kappa)}_{\xi}, \underbrace{\frac{\mathbf{\Lambda}_C}{1-\kappa^2}}_{\eta}\right) \qquad (4.62)$$

$$= \frac{\sqrt{\det(\boldsymbol{\eta})}}{2\pi}\exp\left(-\frac{1}{2}(\mathbf{\Gamma}_n - \boldsymbol{\xi})^\dagger\boldsymbol{\eta}(\mathbf{\Gamma}_n - \boldsymbol{\xi})\right). \qquad (4.63)$$

Inserting (4.63) in (4.61) yields

$$\ln\Big(\varepsilon^{(\boldsymbol{\Gamma}_{n-1}\to\boldsymbol{\Gamma}_n)}\Big) = \mathbb{E}_{\backslash\boldsymbol{\Gamma}_n}\left[\ln\left(\frac{\sqrt{\det(\boldsymbol{\eta})}}{2\pi}\exp\left(-\frac{1}{2}(\boldsymbol{\Gamma}_n-\boldsymbol{\xi})^\dagger\boldsymbol{\eta}(\boldsymbol{\Gamma}_n-\boldsymbol{\xi})\right)\right)\right] \tag{4.64}$$

$$= \mathbb{E}_{\backslash\boldsymbol{\Gamma}_n}\left[-(\boldsymbol{\Gamma}_n-\boldsymbol{\xi})^\dagger\boldsymbol{\eta}(\boldsymbol{\Gamma}_n-\boldsymbol{\xi})\right] + \mathbb{E}_{\backslash\boldsymbol{\Gamma}_n}\left[g(\boldsymbol{\Lambda}_C)\right] \tag{4.65}$$

$$= \mathbb{E}_{\backslash\boldsymbol{\Gamma}_n}\left[-(\boldsymbol{\Gamma}_n^\dagger\boldsymbol{\eta}\boldsymbol{\Gamma}_n-\boldsymbol{\xi}^\dagger\boldsymbol{\eta}\boldsymbol{\Gamma}_n-\boldsymbol{\Gamma}_n^\dagger\boldsymbol{\eta}\boldsymbol{\xi}+\boldsymbol{\xi}^\dagger\boldsymbol{\eta}\boldsymbol{\xi})\right] + \mathbb{E}_{\backslash\boldsymbol{\Gamma}_n}\left[g(\boldsymbol{\Lambda}_C)\right] \tag{4.66}$$

$$= -\Big(\boldsymbol{\Gamma}_n^\dagger\overline{\boldsymbol{\eta}}\boldsymbol{\Gamma}_n-\overline{\boldsymbol{\xi}}^\dagger\overline{\boldsymbol{\eta}}\boldsymbol{\Gamma}_n-\boldsymbol{\Gamma}_n^\dagger\overline{\boldsymbol{\eta}}\overline{\boldsymbol{\xi}}+\underbrace{\mathbb{E}_{\backslash\boldsymbol{\Gamma}_n}\left[\boldsymbol{\xi}^\dagger\boldsymbol{\eta}\boldsymbol{\xi}\right]}_{\text{constant}}\Big) + \mathbb{E}_{\backslash\boldsymbol{\Gamma}_n}\left[g(\boldsymbol{\Lambda}_C)\right] \tag{4.67}$$

$$= -(\boldsymbol{\Gamma}_n-\overline{\boldsymbol{\xi}})^\dagger\overline{\boldsymbol{\eta}}(\boldsymbol{\Gamma}_n-\overline{\boldsymbol{\xi}}) + \mathbb{E}_{\backslash\boldsymbol{\Gamma}_n}\left[g(\boldsymbol{\Lambda}_C)\right] + \text{constant}, \tag{4.68}$$

where g is a deterministic function of $\boldsymbol{\Lambda}_C$. The first term is recognised as the pdf of a Gaussian distribution with mean $\overline{\boldsymbol{\xi}} = \kappa\overline{\boldsymbol{\Gamma}}_{n-1}+\overline{\boldsymbol{\mu}}_C(1-\kappa)$ and covariance $\overline{\boldsymbol{\eta}} = \left(\frac{\overline{\boldsymbol{\Lambda}}_C}{1-\kappa^2}\right)^{-1}$. Thus, the statistics of the message are

$$\overline{\varepsilon}^{(\boldsymbol{\Gamma}_{n-1}\to\boldsymbol{\Gamma}_n)} = \overline{\boldsymbol{\mu}}_C + \kappa\big(\overline{\boldsymbol{\Gamma}}_{n-1} - \overline{\boldsymbol{\mu}}_C\big), \tag{4.69}$$

$$\overline{\overline{\varepsilon}}^{(\boldsymbol{\Gamma}_{n-1}\to\boldsymbol{\Gamma}_n)} = (1-\kappa^2)\overline{\boldsymbol{\Lambda}}_C^{-1}, \tag{4.70}$$

where $\boldsymbol{\mu}_C$ and $\boldsymbol{\Lambda}_C$ themselves are stochastic variables.

The second message $\varepsilon^{(\boldsymbol{\Gamma}_{n+1}\to\boldsymbol{\Gamma}_n)}$ is derived similarly, except that the Markov chain is now given by

$$\boldsymbol{\Gamma}_n = \frac{1}{\kappa}(\boldsymbol{\Gamma}_{n+1} + \boldsymbol{V}_N), \tag{4.71}$$

where this expression is obtained by (4.24). Thus, the statistics of the message are

$$\overline{\varepsilon}^{(\boldsymbol{\Gamma}_{n+1}\to\boldsymbol{\Gamma}_n)} = \overline{\boldsymbol{\mu}}_C + \frac{1}{\kappa}\big(\overline{\boldsymbol{\Gamma}}_{n+1} - \overline{\boldsymbol{\mu}}_C\big), \tag{4.72}$$

$$\overline{\overline{\varepsilon}}^{(\boldsymbol{\Gamma}_{n+1}\to\boldsymbol{\Gamma}_n)} = \frac{1-\kappa^2}{\kappa^2}\overline{\boldsymbol{\Lambda}}_C^{-1}. \tag{4.73}$$

The third message $\varepsilon^{(\boldsymbol{Z}_n\to\boldsymbol{\Gamma}_n)}$ is now derived. This is the same expression as in (4.32) with the expectation taken for all variables except $\boldsymbol{\Gamma}_n$ instead. Thus,

$$\mathbb{E}_{\backslash\boldsymbol{\Gamma}_n}\left[\ln(p(\boldsymbol{Z}_n|\boldsymbol{\phi}_n,\boldsymbol{\Gamma}_n))\right] \propto -\mathbb{E}_{\backslash\boldsymbol{\Gamma}_n}\left[\Big(\underbrace{\boldsymbol{Z}_n-\boldsymbol{S}(\boldsymbol{\phi}_n)}_{\dot{\boldsymbol{Z}}_n}-\boldsymbol{M}\boldsymbol{\Gamma}_n\Big)^\dagger\boldsymbol{\Lambda}_Z\Big(\underbrace{\boldsymbol{Z}_n-\boldsymbol{S}(\boldsymbol{\phi}_n)}_{\dot{\boldsymbol{Z}}_n}-\boldsymbol{M}\boldsymbol{\Gamma}_n\Big)\right]. \tag{4.74}$$

Applying the the same steps as in (4.32)-(4.35) results in

$$\mathbb{E}_{\backslash\boldsymbol{\Gamma}_n}\left[\ln(p(\boldsymbol{Z}_n|\boldsymbol{\phi}_n,\boldsymbol{\Gamma}_n))\right] \propto -\Big(\mathbb{E}_{\backslash\boldsymbol{\Gamma}_n}\left[\dot{\boldsymbol{Z}}_n\right] - \boldsymbol{M}\boldsymbol{\Gamma}_n\Big)^\dagger\boldsymbol{\Lambda}_Z\Big(\mathbb{E}_{\backslash\boldsymbol{\Gamma}_n}\left[\dot{\boldsymbol{Z}}_n\right] - \boldsymbol{M}\boldsymbol{\Gamma}_n\Big), \tag{4.75}$$

where

$$\mathbb{E}_{\backslash\boldsymbol{\Gamma}_n}\left[\dot{\boldsymbol{Z}}\right] = \boldsymbol{Z}_n - \boldsymbol{S}(\overline{\boldsymbol{\phi}}_n) = \widetilde{\boldsymbol{Z}}_n. \tag{4.76}$$

The expression in (4.75) is recognised as a Gaussian distribution in $\widetilde{\boldsymbol{Z}}_n$, but not in $\boldsymbol{\Gamma}_n$. The non-Gaussian nature of $\boldsymbol{\Gamma}_n$ becomes apparent when examining the pdf:

$$p(\boldsymbol{Z}_n|\boldsymbol{\phi}_n, \boldsymbol{\Gamma}_n) \propto \exp\left(-\left(\widetilde{\boldsymbol{Z}}_n - \boldsymbol{M}\boldsymbol{\Gamma}_n\right)^\dagger \boldsymbol{\Lambda}_Z \left(\widetilde{\boldsymbol{Z}}_n - \boldsymbol{M}\boldsymbol{\Gamma}_n\right)\right). \tag{4.77}$$

If the distribution were Gaussian in both $\widetilde{\boldsymbol{Z}}_n$ and $\boldsymbol{\Gamma}_n$, it would allow the following rewriting:

$$p(\boldsymbol{Z}_n|\boldsymbol{\phi}_n, \boldsymbol{\Gamma}_n) \propto \exp\left(-\left(\boldsymbol{M}^{-1}\widetilde{\boldsymbol{Z}}_n - \boldsymbol{\Gamma}_n\right)^\dagger \boldsymbol{\Lambda}_Z \left(\boldsymbol{M}^{-1}\widetilde{\boldsymbol{Z}}_n - \boldsymbol{\Gamma}_n\right)\right). \tag{4.78}$$

However, as $\boldsymbol{M}$ is non-square, $\boldsymbol{M}^{-1}$ does not exist, making (4.78) an invalid rewriting. Since it is desired for the distribution to be Gaussian, this is enforced:

$$\varepsilon^{(\boldsymbol{Z}_n \to \boldsymbol{\Gamma}_n)} = \mathcal{N}^C\left(\overline{\varepsilon}^{(\boldsymbol{Z}_n \to \boldsymbol{\Gamma}_n)}, \left(\overline{\overline{\varepsilon}}^{(\boldsymbol{Z}_n \to \boldsymbol{\Gamma}_n)}\right)^{-1}\right). \tag{4.79}$$

To obtain a distribution that is close to $p(\boldsymbol{Z}_n|\boldsymbol{\phi}_n, \boldsymbol{\Gamma}_n)$, moment matching is utilised. Thereby, the mean $\overline{\varepsilon}^{(\boldsymbol{Z}_n \to \boldsymbol{\Gamma}_n)}$ and covariance $\overline{\overline{\varepsilon}}^{(\boldsymbol{Z}_n \to \boldsymbol{\Gamma}_n)}$ is set to the mean and covariance of $p(\boldsymbol{Z}_n|\boldsymbol{\phi}_n, \boldsymbol{\Gamma}_n)$. Thus,

$$\overline{\varepsilon}^{(\boldsymbol{Z}_n \to \boldsymbol{\Gamma}_n)} = \int_{\boldsymbol{\Gamma}_n} \boldsymbol{\Gamma}_n p(\boldsymbol{Z}_n|\boldsymbol{\phi}_n, \boldsymbol{\Gamma}_n) \, \mathrm{d}\boldsymbol{\Gamma}_n. \tag{4.80}$$

As this is difficult to evaluate directly, the integral is instead taken over the entire complex space $\mathbb{C}$, while still restricting it to a specific plane of $\boldsymbol{\Gamma}_n$. Thus,

$$\overline{\varepsilon}^{(\boldsymbol{Z}_n \to \boldsymbol{\Gamma}_n)} = \int_{\mathbb{C}} p(\boldsymbol{Z}_n|\boldsymbol{S}_C) \int_{\boldsymbol{\Gamma}_n} \boldsymbol{\Gamma}_n \delta(\boldsymbol{S}_C - \boldsymbol{M}\boldsymbol{\Gamma}_n) \, \mathrm{d}\boldsymbol{\Gamma}_n \mathrm{d}\boldsymbol{S}_C, \tag{4.81}$$

where $\boldsymbol{S}_C \in \mathbb{C}$ and $\delta(\cdot)$ is the Dirac delta function. The innermost integral in (4.81) outputs a value when

$$\boldsymbol{S}_C = \boldsymbol{M}\boldsymbol{\Gamma}_n. \tag{4.82}$$

However, when solving for $\boldsymbol{\Gamma}_n$, a solution is not guaranteed to exist for (4.82) as the equation is over-determined. A solution is found, using the Moore-Penrose pseudo inverse denoted as $\cdot^+$ such that

$$\boldsymbol{\Gamma}_n = \boldsymbol{M}^+ \boldsymbol{S}_C. \tag{4.83}$$

The innermost integral in (4.81) is then equal to

$$\int_{\boldsymbol{\Gamma}_n} \boldsymbol{\Gamma}_n \delta(\boldsymbol{S}_C - \boldsymbol{M}\boldsymbol{\Gamma}_n) \, \mathrm{d}\boldsymbol{\Gamma}_n = \boldsymbol{M}^+ \boldsymbol{S}_C, \tag{4.84}$$

due to the integral only giving an output when $\boldsymbol{S}_C = \boldsymbol{M}\boldsymbol{\Gamma}_n$. Inserting (4.84) into (4.81), results in

$$\overline{\varepsilon}^{(\boldsymbol{Z}_n \to \boldsymbol{\Gamma}_n)} = \int_{\mathbb{C}} p(\boldsymbol{Z}_n|\boldsymbol{S}_C) \boldsymbol{M}^+ \boldsymbol{S}_C \, \mathrm{d}\boldsymbol{S}_C \tag{4.85}$$

$$= \boldsymbol{M}^+ \int_{\mathbb{C}} p(\boldsymbol{Z}_n|\boldsymbol{S}_C) \boldsymbol{S}_C \, \mathrm{d}\boldsymbol{S}_C \tag{4.86}$$

$$= \boldsymbol{M}^+ \boldsymbol{Z}_n. \tag{4.87}$$

The same procedure is used for the covariance matrix. Here, it is utilised that the covariance is written as

$$\bar{\bar{\varepsilon}}^{(\boldsymbol{Z}_n \to \boldsymbol{\Gamma}_n)} = \mathrm{Cov}(p(\boldsymbol{Z}_n | \boldsymbol{\phi}_n, \boldsymbol{\Gamma}_n)) \tag{4.88}$$

$$= \mathop{\mathbb{E}}_{\backslash \boldsymbol{\Gamma}_n} \left[(p(\boldsymbol{Z}_n | \boldsymbol{\phi}_n, \boldsymbol{\Gamma}_n) - \bar{\varepsilon})(p(\boldsymbol{Z}_n | \boldsymbol{\phi}_n, \boldsymbol{\Gamma}_n) - \bar{\varepsilon})^\dagger \right]. \tag{4.89}$$

It is known that

$$\mathop{\mathbb{E}}_{\backslash \boldsymbol{\Gamma}_n} \left[(\boldsymbol{\Gamma}_n - \bar{\varepsilon})(\boldsymbol{\Gamma}_n - \bar{\varepsilon})^\dagger \right] = \mathop{\mathbb{E}}_{\backslash \boldsymbol{\Gamma}_n} \left[\boldsymbol{\Gamma}_n \boldsymbol{\Gamma}_n^\dagger \right] - \bar{\varepsilon} \cdot \bar{\varepsilon}^\dagger, \tag{4.90}$$

where

$$\mathop{\mathbb{E}}_{\backslash \boldsymbol{\Gamma}_n} \left[\boldsymbol{\Gamma}_n \boldsymbol{\Gamma}_n^\dagger \right] = \int_{\boldsymbol{\Gamma}_n} \boldsymbol{\Gamma}_n \boldsymbol{\Gamma}_n^\dagger p(\widetilde{\boldsymbol{Z}}_n | \boldsymbol{M} \boldsymbol{\Gamma}_n) \, \mathrm{d}\boldsymbol{\Gamma}_n \tag{4.91}$$

$$= \int_{\mathbb{C}} p(\widetilde{\boldsymbol{Z}}_n | \boldsymbol{S}_C) \underbrace{\int_{\boldsymbol{\Gamma}_n} \boldsymbol{\Gamma}_n \boldsymbol{\Gamma}_n^\dagger \delta(\boldsymbol{S}_C - \boldsymbol{M}^+ \boldsymbol{\Gamma}_n) \, \mathrm{d}\boldsymbol{\Gamma}_n \mathrm{d}\boldsymbol{S}_C}_{\boldsymbol{M}^+ \boldsymbol{S}_C \boldsymbol{S}_C^\dagger (\boldsymbol{M}^+)^\dagger} \tag{4.92}$$

$$= \boldsymbol{M}^+ \underbrace{\mathop{\mathbb{E}}_{\backslash \boldsymbol{\Gamma}_n} \left[\boldsymbol{S}_C \boldsymbol{S}_C^\dagger \right]}_{\boldsymbol{\Lambda}_Z^{-1} + \widetilde{\boldsymbol{Z}}_n \widetilde{\boldsymbol{Z}}_n^\dagger} (\boldsymbol{M}^+)^\dagger \tag{4.93}$$

$$= \boldsymbol{M}^+ \boldsymbol{\Lambda}_Z^{-1} (\boldsymbol{M}^+)^\dagger + \underbrace{\boldsymbol{M}^+ \widetilde{\boldsymbol{Z}} \left(\widetilde{\boldsymbol{Z}} \boldsymbol{M}^+ \right)^\dagger}_{\bar{\varepsilon} \cdot \bar{\varepsilon}^\dagger}. \tag{4.94}$$

Inserting (4.91) into (4.94) results in

$$\mathop{\mathbb{E}}_{\backslash \boldsymbol{\Gamma}_n} \left[(\boldsymbol{\Gamma}_n - \bar{\varepsilon})(\boldsymbol{\Gamma}_n - \bar{\varepsilon})^\dagger \right] = \boldsymbol{M}^+ \boldsymbol{\Lambda}_Z^{-1} (\boldsymbol{M}^+)^\dagger + \bar{\varepsilon} \cdot \bar{\varepsilon}^\dagger - \bar{\varepsilon} \cdot \bar{\varepsilon}^\dagger \tag{4.95}$$

$$= \boldsymbol{M}^+ \boldsymbol{\Lambda}_Z^{-1} (\boldsymbol{M}^+)^\dagger. \tag{4.96}$$

Thus, the statistics of the message are given as

$$\bar{\varepsilon}^{\boldsymbol{Z}_n \to \boldsymbol{\Gamma}_n} = \boldsymbol{M}^+ \boldsymbol{Z}_n, \tag{4.97}$$

$$\bar{\bar{\varepsilon}}^{\boldsymbol{Z}_n \to \boldsymbol{\Gamma}_n} = \boldsymbol{M}^+ \boldsymbol{\Lambda}_Z^{-1} \left(\boldsymbol{M}^+ \right)^\dagger. \tag{4.98}$$

As the first three messages going to $\boldsymbol{\Gamma}_n$ are described as multivariate complex Gaussian distributions, the surrogate function $q(\boldsymbol{\Gamma}_n)$ is described as a product of these distributions:

$$q(\boldsymbol{\Gamma}_n) = \mathcal{N}^C(\boldsymbol{\mu}_{\mathrm{total}}, \boldsymbol{\Lambda}_{\mathrm{total}}) = \prod_{n=0}^{N} \mathcal{N}^C(\boldsymbol{\mu}_n, \boldsymbol{\Lambda}_n), \tag{4.99}$$

where

$$\left(\boldsymbol{\Lambda}_{\mathrm{total}}^{(k)} \right)^{-1} = \sum_{n=0}^{N} \bar{\bar{\varepsilon}}^{(\boldsymbol{\Gamma}_{n-1} \to \boldsymbol{\Gamma}_n)} + \bar{\bar{\varepsilon}}^{(\boldsymbol{\Gamma}_{n+1} \to \boldsymbol{\Gamma}_n)} + \bar{\bar{\varepsilon}}^{(\boldsymbol{Z}_n \to \boldsymbol{\Gamma}_n)} \tag{4.100}$$

is the total precision matrix, and

$$\boldsymbol{\mu}_{\mathrm{total}}^{(k)} = \left(\boldsymbol{\Lambda}_{\mathrm{total}}^{(k)} \right)^{-1} \sum_{n=0}^{N} \Bigg(\left(\bar{\bar{\varepsilon}}^{(\boldsymbol{\Gamma}_{n-1} \to \boldsymbol{\Gamma}_n)} + \bar{\bar{\varepsilon}}^{(\boldsymbol{\Gamma}_{n+1} \to \boldsymbol{\Gamma}_n)} + \bar{\bar{\varepsilon}}^{(\boldsymbol{Z}_n \to \boldsymbol{\Gamma}_n)} \right)$$
$$\times \left(\bar{\varepsilon}^{(\boldsymbol{\Gamma}_{n-1} \to \boldsymbol{\Gamma}_n)} + \bar{\varepsilon}^{(\boldsymbol{\Gamma}_{n+1} \to \boldsymbol{\Gamma}_n)} + \bar{\varepsilon}^{(\boldsymbol{Z}_n \to \boldsymbol{\Gamma}_n)} \right) \Bigg) \tag{4.101}$$

is the total mean vector. The precision matrices are given by (4.70),(4.73), and (4.98) and the means are given by (4.69), (4.72), and (4.97).

The fourth message $\varepsilon^{(\boldsymbol{\mu}_C \to \boldsymbol{\Gamma}_n)}$ is now derived. This is done similarly as for $\varepsilon^{(\boldsymbol{\Gamma}_{n-1} \to \boldsymbol{\Gamma}_n)}$, but where the expectation is taken for all variables expect $\boldsymbol{\mu}_C$ instead. Thus,

$$\ln\left(\varepsilon^{(\boldsymbol{\mu}_C \to \boldsymbol{\Gamma}_n)}\right) = \mathop{\mathbb{E}}_{\backslash \boldsymbol{\mu}_C} \left[\ln(p(\boldsymbol{\Gamma}_n | \boldsymbol{\Gamma}_{n-1}, \boldsymbol{\mu}_C, \boldsymbol{\Lambda}_C))\right]. \tag{4.102}$$

Here,

$$p(\boldsymbol{\Gamma}_n | \boldsymbol{\Gamma}_{n-1}, \boldsymbol{\mu}_C, \boldsymbol{\Lambda}_C) = \mathcal{N}^C\Big(\underbrace{\frac{1}{1-\kappa}\boldsymbol{\Gamma}_n - \frac{\kappa}{1-\kappa}\boldsymbol{\Gamma}_{n-1}}_{\boldsymbol{\Upsilon}}, \underbrace{\frac{\boldsymbol{\Lambda}_C}{1-\kappa^2}}_{\boldsymbol{\eta}} \Big) \tag{4.103}$$

$$= \frac{\sqrt{\det(\boldsymbol{\eta})}}{2\pi}\exp\Big(-\frac{1}{2}(\boldsymbol{\mu}_C - \boldsymbol{\Upsilon})^\dagger \boldsymbol{\eta}(\boldsymbol{\mu}_C - \boldsymbol{\Upsilon})\Big). \tag{4.104}$$

Applying the same steps as in (4.64)-(4.68), yields

$$\ln\left(\varepsilon^{(\boldsymbol{\mu}_C \to \boldsymbol{\Gamma}_n)}\right) = = -((\boldsymbol{\mu}_C - \overline{\boldsymbol{\Upsilon}})^\dagger \overline{\boldsymbol{\eta}}(\boldsymbol{\mu}_C - \overline{\boldsymbol{\Upsilon}})) + \mathop{\mathbb{E}}_{\backslash \boldsymbol{\mu}_C} [g(\boldsymbol{\Lambda}_C)] + \text{constant}. \tag{4.105}$$

Thus, the statistics of the message are given as

$$\overline{\varepsilon}^{(\boldsymbol{\mu}_C \to \boldsymbol{\Gamma}_n)} = \frac{1}{1-\kappa}\overline{\boldsymbol{\Gamma}}_n - \frac{\kappa}{1-\kappa}\overline{\boldsymbol{\Gamma}}_{n-1}, \tag{4.106}$$

$$\overline{\overline{\varepsilon}}^{(\boldsymbol{\mu}_C \to \boldsymbol{\Gamma}_n)} = (1-\kappa^2)\overline{\boldsymbol{\Lambda}}_C^{-1}. \tag{4.107}$$

As a result, the surrogate function $q(\boldsymbol{\mu}_C)$ becomes

$$q(\boldsymbol{\mu}_C) = \prod_{n=1}^N \mathcal{N}^C\Big(\frac{1}{1-\kappa}\overline{\boldsymbol{\Gamma}}_n - \frac{\kappa}{1-\kappa}\overline{\boldsymbol{\Gamma}}_{n-1}, (1-\kappa^2)\overline{\boldsymbol{\Lambda}}_C^{-1} \Big). \tag{4.108}$$

The fifth message $\varepsilon^{(\boldsymbol{\Lambda}_C \to \boldsymbol{\Gamma}_n)}$ is written similarly to $\varepsilon^{(\boldsymbol{\Gamma}_{n-1} \to \boldsymbol{\Gamma}_n)}$ but where the expectation is taken across all variables except $\boldsymbol{\Lambda}_C$. Thus,

$$\varepsilon^{(\boldsymbol{\Lambda}_C \to \boldsymbol{\Gamma}_n)} = \mathop{\mathbb{E}}_{\backslash \boldsymbol{\Lambda}_C} \left[\ln(p(\boldsymbol{\Gamma}_n | \boldsymbol{\Gamma}_{n-1}, \boldsymbol{\mu}_C, \boldsymbol{\Lambda}_C))\right] \tag{4.109}$$

$$= \mathop{\mathbb{E}}_{\backslash \boldsymbol{\Lambda}_C} \left[\ln\Big(\frac{\sqrt{\det(\boldsymbol{\eta})}}{2\pi}\exp\Big(-\frac{1}{2}(\boldsymbol{\Gamma}_n - \boldsymbol{\xi})^\dagger \boldsymbol{\eta}(\boldsymbol{\Gamma}_n - \boldsymbol{\xi})\Big)\Big)\right], \tag{4.110}$$

where

$$\boldsymbol{\xi} = \kappa\boldsymbol{\Gamma}_{n-1} + \boldsymbol{\mu}_C(1-\kappa), \qquad \boldsymbol{\eta} = \frac{\boldsymbol{\Lambda}_C}{1-\kappa^2}. \tag{4.111}$$

The message is rewritten as

$$\varepsilon^{(\boldsymbol{\Lambda}_C \to \boldsymbol{\Gamma}_n)} = -\mathop{\mathbb{E}}_{\backslash \boldsymbol{\Lambda}_C} \left[\left(\boldsymbol{\Gamma}_n^\dagger \boldsymbol{\eta}\boldsymbol{\Gamma}_n - \boldsymbol{\Gamma}_n^\dagger \boldsymbol{\eta}\boldsymbol{\xi} - \boldsymbol{\xi}^\dagger \boldsymbol{\eta}\boldsymbol{\Gamma}_n + \boldsymbol{\xi}^\dagger \boldsymbol{\eta}\boldsymbol{\xi}\right)\right] + h(\boldsymbol{\Lambda}_C) \tag{4.112}$$

$$= -\Big(\underbrace{\mathop{\mathbb{E}}_{\backslash \boldsymbol{\Lambda}_C} \left[\boldsymbol{\Gamma}_n^\dagger \boldsymbol{\eta}\boldsymbol{\Gamma}_n\right]}_{\text{tr}\left(\boldsymbol{\eta}\overline{\overline{\boldsymbol{\Gamma}}}_n\right) + \overline{\boldsymbol{\Gamma}}_n^\dagger \boldsymbol{\eta}\overline{\boldsymbol{\Gamma}}_n} - \overline{\boldsymbol{\Gamma}}_n^\dagger \boldsymbol{\eta}\overline{\boldsymbol{\xi}} - \overline{\boldsymbol{\xi}}^\dagger \boldsymbol{\eta}\overline{\boldsymbol{\Gamma}}_n + \mathop{\mathbb{E}}_{\backslash \boldsymbol{\Lambda}_C} \left[\boldsymbol{\xi}^\dagger \boldsymbol{\eta}\boldsymbol{\xi}\right] \Big) + h(\boldsymbol{\Lambda}_C), \tag{4.113}$$

where h is a deterministic function of $\mathbf{\Lambda}_C$. Thus, the surrogate function $\ln(q_n(\mathbf{\Lambda}_C))$ becomes

$$\ln(q_n(\mathbf{\Lambda}_C)) \propto -\mathrm{tr}\left(\boldsymbol{\eta}\overline{\overline{\mathbf{\Gamma}}}_n\right) - \overline{\mathbf{\Gamma}}_n^\dagger \boldsymbol{\eta} \overline{\mathbf{\Gamma}}_n + \mathrm{Re}\left(\overline{\mathbf{\Gamma}}_n^\dagger \boldsymbol{\eta} \overline{\boldsymbol{\xi}}\right) + h(\mathbf{\Lambda}_C). \tag{4.114}$$

With this a factorised diagonal prior is imposed on $\mathbf{\Lambda}_C$ such that $p(\Lambda_{C,i\neq j}) = 0$. Thus, each term is rewritten using the diagonal prior:

$$\mathrm{tr}(\boldsymbol{\eta}\overline{\overline{\mathbf{\Gamma}}}_n) = \frac{1}{1-\kappa^2}\sum_{j=1}^{N_b} \mathbf{\Lambda}_{C,n}\overline{\overline{\mathbf{\Gamma}}}_n, \tag{4.115}$$

$$\overline{\mathbf{\Gamma}}_n^\dagger \boldsymbol{\eta} \overline{\mathbf{\Gamma}} = \frac{1}{1-\kappa^2}\sum_{j=1}^{N_b} |\overline{\mathbf{\Gamma}}_{n,j}| \mathbf{\Lambda}_{C,j}, \tag{4.116}$$

$$\overline{\mathbf{\Gamma}}_n^\dagger \boldsymbol{\eta} \overline{\boldsymbol{\xi}} = \frac{1}{1-\kappa^2}\sum_{j=1}^{N_b} \overline{\mathbf{\Gamma}}_{n,j}\overline{\boldsymbol{\xi}}_j \mathbf{\Lambda}_{C,j}, \tag{4.117}$$

$$h(\mathbf{\Lambda}_C) = \det(\mathbf{\Lambda}_C) = \prod_{j}^{N_b} \mathbf{\Lambda}_{C,j}. \tag{4.118}$$

Inserting these into (4.114) yields

$$q(\mathbf{\Lambda}_C) = \prod_{j=1}^{N_B} \mathbf{\Lambda}_{C,j} \exp\left(-\frac{1}{1-\kappa^2}\left(\sum_{j=1}^{N_B} \mathbf{\Lambda}_{C,n}\overline{\overline{\mathbf{\Gamma}}}_n + \sum_{j=1}^{N_B} |\overline{\mathbf{\Gamma}}_{n,j}|^2 \mathbf{\Lambda}_{C,j} - 2\sum_{j=1}^{N_B} \mathrm{Re}\left(\overline{\mathbf{\Gamma}}_{n,j}\overline{\boldsymbol{\xi}}_j\right)\mathbf{\Lambda}_{C,j}\right)\right). \tag{4.119}$$

The surrogate function factorises in $\mathbf{\Lambda}_{C,j}$, thus

$$q(\mathbf{\Lambda}_{C,j}) = \mathbf{\Lambda}_{C,j}\exp\left(-\sum_{j=1}^{N_B}\mathbb{W}_{n,n-1,j}\mathbf{\Lambda}_{C,j}\right), \tag{4.120}$$

where

$$\mathbb{W}_{n,n-1,j} = \frac{1}{1-\kappa^2}\left(\overline{\overline{\mathbf{\Gamma}}}_{n,j} + |\overline{\mathbf{\Gamma}}_{n,j}|^2 - 2\mathrm{Re}\left(\overline{\mathbf{\Gamma}}_{n,j}\overline{\boldsymbol{\xi}}_{n,j}\right)\right). \tag{4.121}$$

The total surrogate function then becomes a sum of (4.120) over j and a product over n:

$$\prod_{n=0}^{N}\sum_{j=1}^{N_b} q(\mathbf{\Lambda}_{C,j}) = \prod_{n=0}^{N} \mathbf{\Lambda}_{C,j}\exp\left(-\sum_{n=0}^{N}\mathbb{W}_{n,n-1,j}\mathbf{\Lambda}_{C,j}\right) \tag{4.122}$$

$$= \mathbf{\Lambda}_{C,j}^N \exp\left(-\sum_{n=0}^{N}\mathbb{W}_{n,n-1,j}\mathbf{\Lambda}_{C,j}\right). \tag{4.123}$$

This is recognised as a Gamma distribution with parameters

$$\mathcal{G} = N+1, \qquad \epsilon = \mathbb{W}_{n,n-1,j}. \tag{4.124}$$

4.3 Multiple Radar Clutter and Target Bayesian Localisation and Tracking Algorithm

Having obtained expressions for all messages, it is possible to construct the recursive Bayesian filter to estimate $\boldsymbol{\phi}_{0:N}$ and $\mathbf{\Gamma}_{0:N}^{1:N_{\mathrm{radar}}}$ using the observed $\boldsymbol{Z}_{0:N}$. The pseudo code for the algorithm can be seen in Algorithm 1.

Algorithm 1: Multiple Radar Clutter and Target Bayesian Localisation and Tracking

---

1: **procedure** $\mathrm{MRCATBLAT}(\boldsymbol{Z}_N^{1:N_{\mathrm{radar}}}, \overline{\boldsymbol{\mu}}_C^{1:N_{\mathrm{radar}}}, \overline{\overline{\boldsymbol{\mu}}}_C^{1:N_{\mathrm{radar}}}, \overline{\boldsymbol{\Lambda}}_C^{1:N_{\mathrm{radar}}}, \overline{\overline{\boldsymbol{\Lambda}}}_C^{1:N_{\mathrm{radar}}})$

    In parallel at each radar k:

2:     **if** $N = 0$ **then**

        Initialisation

3:         Calculate $\overline{\overline{\varepsilon}}^{\left(\boldsymbol{Z}_N^{(k)} \to \boldsymbol{\Gamma}_N^{(k)}\right)}$ and $\left(\overline{\overline{\varepsilon}}^{\left(\boldsymbol{Z}_N^{(k)} \to \boldsymbol{\Gamma}_N^{(k)}\right)}\right)^{-1}$ using (4.98)   ▷ Stays constant $\forall N$

4:         $\overline{\varepsilon}^{\left(\boldsymbol{Z}_N^{(k)} \to \boldsymbol{\Gamma}_N^{(k)}\right)} \leftarrow \boldsymbol{\Gamma}_N^{(k)}$

5:         $\overline{\boldsymbol{\Gamma}}_N^{(k)} \leftarrow \overline{\varepsilon}^{\left(\boldsymbol{Z}_N^{(k)} \to \boldsymbol{\Gamma}_N^{(k)}\right)}$

6:         $\overline{\overline{\boldsymbol{\Gamma}}}_N^{(k)} \leftarrow \overline{\overline{\varepsilon}}^{\left(\boldsymbol{Z}_N^{(k)} \to \boldsymbol{\Gamma}_N^{(k)}\right)}$

7:         $\overline{\boldsymbol{\mu}}_C^{(k)} \leftarrow \overline{\boldsymbol{\Gamma}}_N^{(k)}$

8:         $\epsilon_j^{(k)} \leftarrow \left|\overline{\boldsymbol{\Gamma}}_{N,j}^{(k)} - \overline{\boldsymbol{\mu}}_{C,j}^{(k)}\right|^2 + \overline{\overline{\boldsymbol{\Gamma}}}_{N,j,j}^{(k)}$

9:         $\left(\overline{\boldsymbol{\Lambda}}_C^{(k)}\right)^{-1} \leftarrow \boldsymbol{\epsilon}^{(k)}$

10:     **else**

       Local message passing at each radar

       Clutter Message Passing

11:         $\widetilde{\boldsymbol{Z}}_N^{(k)} \leftarrow \boldsymbol{Z}_N^{(k)} - \boldsymbol{S}_N^{(k)}(\bar{\boldsymbol{\phi}}_N)$

12:         $\overline{\varepsilon}^{(\boldsymbol{Z}_N \to \boldsymbol{\Gamma}_N)} \leftarrow \boldsymbol{M}^\dagger \widetilde{\boldsymbol{Z}}_N$ using (4.97)

13:         Calculate $\overline{\overline{\varepsilon}}^{(\boldsymbol{Z}_N \to \boldsymbol{\Gamma}_N)}$ and $\left(\overline{\overline{\varepsilon}}^{(\boldsymbol{Z}_N \to \boldsymbol{\Gamma}_N)}\right)^{-1}$ using (4.98).   ▷ Stays constant $\forall N$

14:         **for** ite $\leftarrow 1$ to N_{ite} **do**

15:             **for** $n \leftarrow 0$ to N **do**

16:                $\overline{\overline{\boldsymbol{\Gamma}}}_n^{-1} \leftarrow \sum_{\varepsilon \in \mathcal{N}_{\boldsymbol{\Gamma}_n}} \overline{\overline{\varepsilon}}_n^{-1}$

17:                $\overline{\boldsymbol{\Gamma}}_n \leftarrow \overline{\overline{\boldsymbol{\Gamma}}}_n \sum_{\varepsilon \in \mathcal{N}_{\boldsymbol{\Gamma}_n}} \overline{\overline{\varepsilon}}^{-1}\overline{\varepsilon}$

18:         Update $\overline{\boldsymbol{\mu}}_C$ using (4.106) and $\overline{\overline{\boldsymbol{\mu}}}_C$ using (4.107)

19:         $\boldsymbol{\epsilon} \leftarrow \sum_{n=0}^{N} \mathbb{W}_{n,n-1,j}$ using (4.121)

20:         $\overline{\boldsymbol{\Lambda}}_C^{-1} = \boldsymbol{\epsilon}/(N+1)$

       Target Message Passing

21:         $\check{\boldsymbol{Z}}_N^{(k)} \leftarrow \boldsymbol{Z}_N^{(k)} - \boldsymbol{M}\overline{\boldsymbol{\Gamma}}_N^{(k)}$

22:         $\left(\overline{\varepsilon}^{\left(\boldsymbol{Z}_N^{(k)} \to \phi_N\right)}, \overline{\overline{\varepsilon}}^{\left(\boldsymbol{Z}_N^{(k)} \to \phi_N\right)}\right) \leftarrow \arg\min_{\overline{\varepsilon},\overline{\overline{\varepsilon}}} \mathrm{D}_{\mathrm{KL}}\left(\check{\boldsymbol{Z}}_N^{(k)}\right)$ using (4.50)

23:         Broadcast to all radars $\left(\overline{\varepsilon}^{\left(\boldsymbol{Z}_N^{(k)} \to \phi_N\right)}, \overline{\overline{\varepsilon}}^{\left(\boldsymbol{Z}_N^{(k)} \to \phi_N\right)}\right)$ and save to memory

24:         **for** ite $\leftarrow 1$ to N_{ite} **do**

25:             **for** $n \leftarrow 0$ to N **do**

26:                $\overline{\overline{\phi}}_n^{-1} \leftarrow \sum_{\varepsilon_n \in \mathcal{N}_{\phi_n}} \overline{\overline{\varepsilon}}_n^{-1}$

27:                $\overline{\phi}_n \leftarrow \overline{\overline{\phi}}_n \sum_{\varepsilon_n \in \mathcal{N}_{\phi_n}} \overline{\overline{\varepsilon}}_n^{-1}\overline{\varepsilon}_n$

28:         **if** $N > 1$ **then**

29:             $\boldsymbol{\beta} = \sum_{n=1}^{N} \mathbb{V}_{n,n-1}$ using (4.55)

30:             $\overline{\boldsymbol{\Lambda}}_a^{-1} = \boldsymbol{\beta}/(N+1)$

31:         **else**

32:             $\boldsymbol{\Lambda}_a \leftarrow \boldsymbol{\Lambda}_a^{(\mathrm{init})}$

33: **return** $\left(\overline{\boldsymbol{\Gamma}}_{0:N}^{1:N_{\mathrm{radar}}}, \overline{\overline{\boldsymbol{\Gamma}}}_{0:N}^{1:N_{\mathrm{radar}}}\right), \left(\overline{\boldsymbol{\mu}}_C^{1:N_{\mathrm{radar}}}, \overline{\overline{\boldsymbol{\mu}}}_C^{1:N_{\mathrm{radar}}}, \overline{\boldsymbol{\Lambda}}_C^{1:N_{\mathrm{radar}}}, \overline{\overline{\boldsymbol{\Lambda}}}_C^{1:N_{\mathrm{radar}}}\right)$, and $\left(\overline{\boldsymbol{\phi}}_{0:N}, \overline{\overline{\boldsymbol{\phi}}}_{0:N}\right)$

Prototype Implementation of Algorithm

<div style="text-align:right">5</div>

With the MRCaTBLaT algorithm formulated in **??**, a prototype implementation of it has been developed to enable performance evaluation. This chapter describes the simulation setup and provides an overview of the different code components involved. The general structure of the implementation is depicted in Figure 5.1, where the arrows represents the flow of information. The prototype code is written in MATLAB and executed on consumer-grade hardware. A brief explanation of each block in Figure 5.1 is now given, followed by a deeper explanation of the signal generator and MRCaTBLaT.

Scenarios
This script defines all settings based on a case selected through a switch statement by a user. Each case specifies the settings for the target, target trajectory, clutter field, and radars.

Trajectory Generator
This class, provided by supervisor Anders Westerkam, creates the trajectory of the target based on the settings defined in "Scenarios". It is ensured that Newton's laws of motion are fulfilled. It supports both linear and circular motion, as well as acceleration and deceleration phases. It
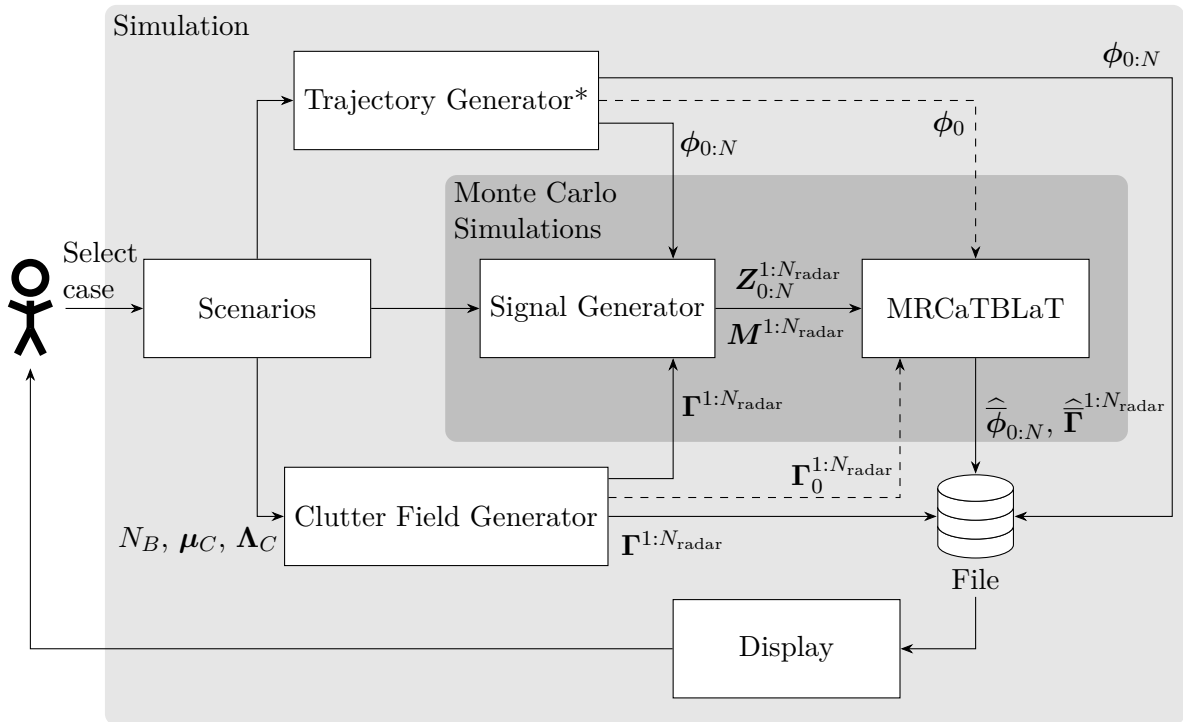
Figure 5.1. Structure of implementation of prototype code. The block marked with * contains code provided by a third party. The arrows represent the flow of information, where the dashed line indicate that only a small part of the output is sent.

outputs the trajectory of the target, consisting of its positions and the corresponding time steps for each position. An example of a target trajectory is seen in Figure 5.2.

Clutter Field Generator

This function generates a clutter field for each radar based on the statistics defined in "Scenarios". It outputs the subset of basis functions Ψ_{N_B} and the expansion coefficients $\mathbf{\Gamma}^{(k)} \sim N^C(\boldsymbol{\mu}_C, \boldsymbol{\Lambda}_C)$ for each radar $k = 1 : N_{\text{radar}}$. An example of a clutter field is depicted in Figure 5.3.

Signal Generator

This class generates the received signal $\boldsymbol{Z}_n^{(k)}$ in a radar. It uses the settings for the system setup from "Scenarios" together with the position of the target along with Ψ_{N_B} and $\mathbf{\Gamma}_n^{(k)}$.

MRCaTBLaT

This script contains the MRCaTBLaT algorithm. It uses the first position from "Trajectory Generator", the position of the radars from "Scenarios", and the received signals $\boldsymbol{Z}_{0:n}^{1:N_{\text{radar}}}$ and $\boldsymbol{M}^{1:N_{\text{radar}}}$ from "Signal Generator" to output the estimated parameters of the target $\widehat{\overline{\boldsymbol{\phi}}}_{0:n}$ and clutter field $\widehat{\overline{\boldsymbol{\Gamma}}}_{0:n}^{1:N_{\text{radar}}}$.

5.1 Implementation of Signal Generator

The signal generator outputs a received signal $\boldsymbol{Z}_n^{(k)}$ in a radar operating in TDM mode transmitting complex baseband signals with a linear chirp. This data is generated using the signal model in (3.69). As input, it takes the current position of the target in local coordinates $[x_n^{(k)} \; y_n^{(k)}]$ and the system settings of the radar as well as $\mathbf{\Gamma}_n^{(k)}$ and Ψ_{N_B}. The target signal and clutter signal is generated separately which allows them to be combined as needed. This enables modelling of three scenarios:

1. Clutter-free environment with one target (CF1T), $\boldsymbol{Z}_n^{(k)} = \boldsymbol{S}_n^{(k)} + \boldsymbol{W}_n^{(k)}$.
2. Clutter environment with no target (C0T), $\boldsymbol{Z}_n^{(k)} = \boldsymbol{M}^{(k)}\mathbf{\Gamma}_n^{(k)} + \boldsymbol{W}_n^{(k)}$.
3. Clutter environment with one target (C1T), $\boldsymbol{Z}_n^{(k)} = \boldsymbol{S}_n^{(k)} + \boldsymbol{M}^{(k)}\mathbf{\Gamma}_n^{(k)} + \boldsymbol{W}_n^{(k)}$.

Apart from the target signal and clutter signal, the signal generator also outputs the matrix $\boldsymbol{M}^{(k)}$ from (3.69).
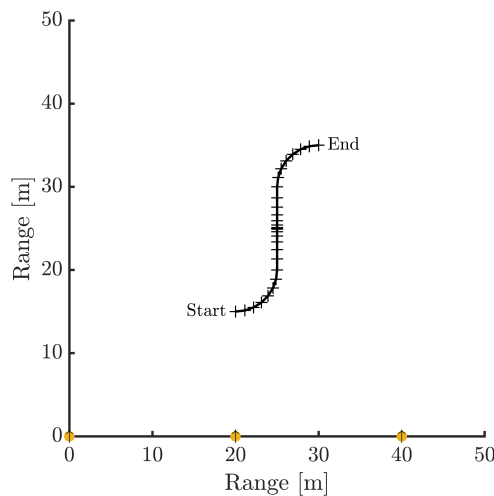

Figure 5.2. Example of a target trajectory. The discretised positions are marked with +.
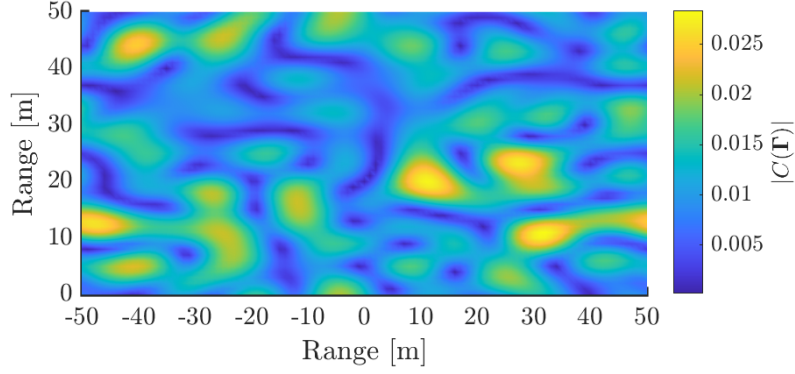
Figure 5.3. Example of a clutter field obtained using $N_B = 80$, $\mu_C^{(k)} = 0$, and $\sigma_C^{(k)} = 0.001$.

5.1.1 Generation of Target Signal

The received signal for the target is based on $\boldsymbol{S}_n^{(k)}$ from (3.69), where f_{IF} and $\alpha_n^{(m,j,k)}$ are calculated as in (2.14) and (2.5), respectively. To get a closed form expression, the Fourier transform of the target signal with respect to time is done as a discrete Fourier transform (DFT):

$$S_n^{(m,j,k)}[h'] = \mathcal{F}_{h \to h'}\left\{ s_{n,\text{target}}^{(m,j,k)}[h] \right\} \tag{5.1}$$

$$= \sum_{h=0}^{N_s-1} \alpha_n^{(m,j,k)} A^{(m,j,k)}\left(x_n^{(k)}, y_n^{(k)}\right) e^{i2\pi f_{\text{IF}}\left(x_n^{(k)}, y_n^{(k)}\right) hT_s} e^{-i2\pi \frac{h'}{N_s} h} \tag{5.2}$$

$$= \alpha_n^{(m,j,k)} A^{(m,j,k)}\left(x_n^{(k)}, y_n^{(k)}\right) \sum_{h=0}^{N_s-1} e^{i\left(2\pi f_{\text{IF}}\left(x_n^{(k)}, y_n^{(k)}\right)T_s - 2\pi \frac{h'}{N_s}\right)h}. \tag{5.3}$$

The expression is simplified by recognising the sum as a finite geometric series. Applying the result from Section C.1, the DFT of the target signal model becomes

$$S_n^{(m,j,k)}[h'] = \alpha_n^{(m,j,k)} A^{(m,j,k)}\left(x_n^{(k)}, y_n^{(k)}\right) \tag{5.4}$$

$$\times e^{i(N_s-1)\pi\left(f_{\text{IF}}\left(x_n^{(k)}, y_n^{(k)}\right)T_s - \frac{h'}{N_s}\right)} \cdot \frac{\sin\left(N_s \pi \left(f_{\text{IF}}\left(x_n^{(k)}, y_n^{(k)}\right)T_s - \frac{h'}{N_s}\right)\right)}{\sin\left(\pi \left(f_{\text{IF}}\left(x_n^{(k)}, y_n^{(k)}\right)T_s - \frac{h'}{N_s}\right)\right)}.$$

Using the received signals $\boldsymbol{S}_n^{(k)}$, the range is estimated as

$$\hat{r}_n^{(k)} = \text{median}\left(\arg\max_{r^{(k)}} \left| \boldsymbol{S}_n^{(k)} \right| \right), \tag{5.5}$$

where arg max is computed individually over each of the $N_T N_R$ channels and the median is taken across all resulting range estimates. The angle $\theta_n^{(k)}$ is found using the Capon beamformer.

The Cartesian coordinates of the target is found from the range and angle as

$$x_n^{(k)} = \hat{r}_n^{(k)} \sin\left(\hat{\theta}_n^{(k)}\right), \qquad y_n^{(k)} = \hat{r}_n^{(k)} \cos\left(\hat{\theta}_n^{(k)}\right). \tag{5.6}$$

Example 5.1.1 (Clutter-free Environment with one Target)
Looking at the CF1T scenario for $N_{\text{radar}} = 1$, where the radar is placed at $[0\ 0]^\top$m and the target is in position $[x_n^{(1)}\ y_n^{(1)}]^\top = [3\ 20]^\top$m, results in Figure 5.4. The plot is generated by calculating $\left| \boldsymbol{S}^{(1)}(\boldsymbol{\phi}_n)^\dagger \boldsymbol{Z}_n^{(1)} \right|$, where the x- and y-coordinate in $\boldsymbol{\phi}_n$ are evaluated across a grid.
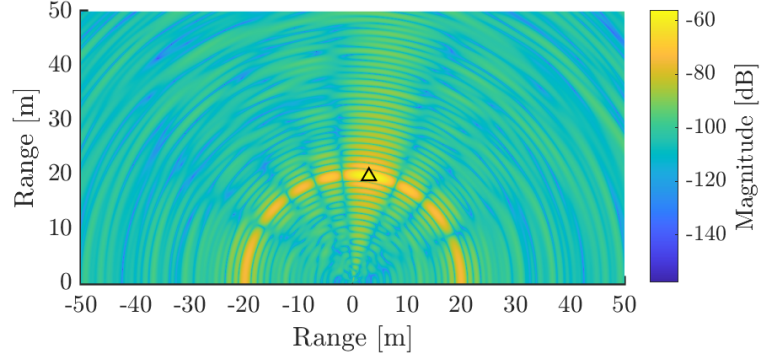
Figure 5.4. Plot of $\left| \boldsymbol{S}^{(1)}(\boldsymbol{\phi}_n)^\dagger \boldsymbol{Z}_n^{(1)} \right|$ with varying $\boldsymbol{\phi}_n$. The radar is placed at $[0\ 0]^\top$ m in the CF1T scenario with $[x_n^{(1)}\ y_n^{(1)}]^\top = [3\ 20]^\top$ m. The ground truth position is marked with a triangle.

The range and angle estimates based on the received signals are

$$\hat{r}_n^{(1)} = 20\,\text{m}, \qquad \hat{\theta}_n^{(1)} = 0.15\,\text{rad}, \tag{5.7}$$

which aligns with the true range and angle. Plots of the range and angle estimations are depicted in Figure 5.10.
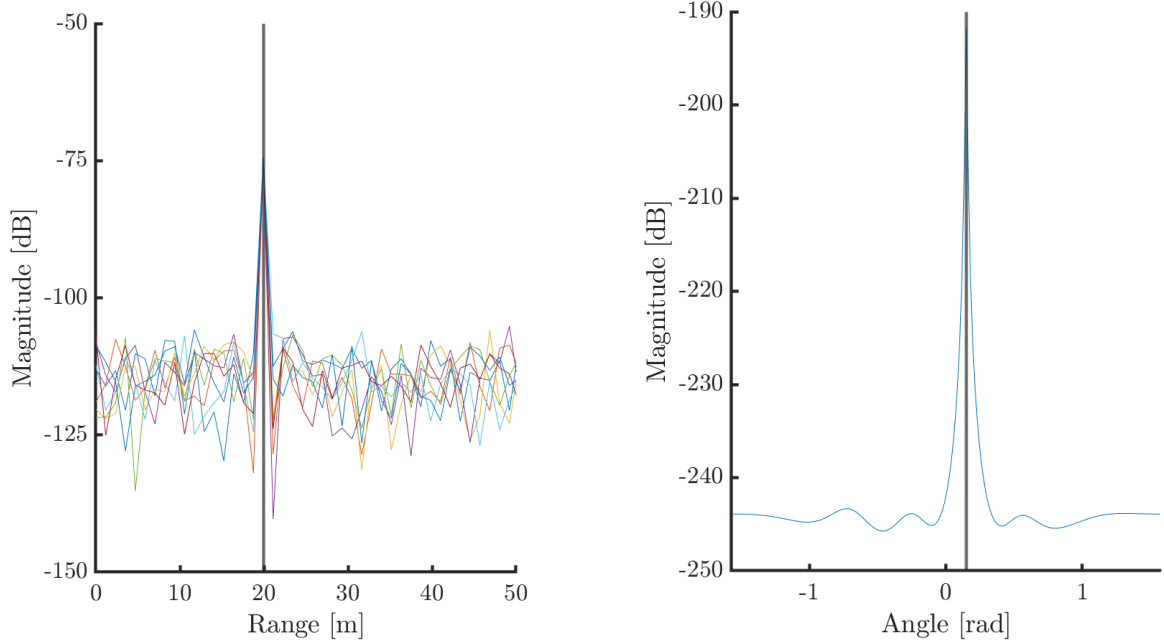
(a) Range estimation. The black vertical line represents the true range.

(b) Angle estimation. The black vertical line represents the true angle.

Figure 5.5. Range and angle estimation. The radar is placed at $[0\ 0]^\top$ m in the CF1T scenario with $[x_n^{(1)}\ y_n^{(1)}]^\top = [3\ 20]^\top$ m.

Converting the range and angle to Cartesian coordinates using (5.6) yields

$$\hat{x}_n^{(1)} = 3\,\text{m}, \qquad \hat{y}_n^{(1)} = 20\,\text{m}. \tag{5.8}$$

5.1.2 Generation of Clutter Signal

The received signal for the clutter is calculated using $\boldsymbol{M}^{(k)}\boldsymbol{\Gamma}_n^{(k)}$ in (3.69). Only the matrix $\boldsymbol{M}^{(k)}$ should be calculated since $\boldsymbol{\Gamma}^{(k)}$ is obtained from the "Clutter Field Generator".

The matrix $\boldsymbol{M}^{(k)} \in \mathbb{C}^{N_s N_T N_R \times N_B}$ contains information of $\mathcal{F}_{h \to h'}\{(\beta^{(l,g,m,j,k)})^*[h]\}$. From (3.60), $(\beta^{(l,g,m,j,k)})^*[h]$ is given as

$$\left(\beta^{(l,g,m,j,k)}\right)^*[h] = \left\langle A^{(m,j,k)}(x,y)\mathrm{e}^{-i2\pi f_{\mathrm{IF}}(x,y)hT_s}, \left(\psi_n^{(l,g)}\right)^*(x,y)\right\rangle. \tag{5.9}$$

Following (5.1)-(5.4), the DFT is applied to Fourier transform in the time domain using the expression obtained in (5.4):

$$\mathcal{F}_{h \to h'}\left\{\left(\beta^{(l,g,m,j,k)}\right)^*[h]\right\} = \left\langle \mathcal{F}_{h \to h'}\left\{A^{(m,j,k)}(x,y)\mathrm{e}^{-i2\pi f_{\mathrm{IF}}(x,y)hT_s}\right\}, \left(\psi_n^{(l,g)}\right)^*(x,y)\right\rangle \tag{5.10}$$

$$= \left\langle \mathbb{F}^{(m,j,k)}(x,y,h'), \left(\psi_n^{(l,g)}\right)^*(x,y)\right\rangle, \tag{5.11}$$

where

$$\mathbb{F}^{(m,j,k)}(x,y,h') = A^{(m,j,k)}(x,y)\mathrm{e}^{i(N_s-1)\pi\left(f_{\mathrm{IF}}^{(k)}T_s - \frac{h'}{N_s}\right)}\frac{\sin\left(N_s\pi\left(f_{\mathrm{IF}}(x,y)T_s - \frac{h'}{N_s}\right)\right)}{\sin\left(\pi\left(f_{\mathrm{IF}}(x,y)T_s - \frac{h'}{N_s}\right)\right)}. \tag{5.12}$$

Here, $\mathbb{F}^{(m,j,k)}(x,y,h')$ is calculated for all values $(x,y) \in \mathbb{Z}$ in the FOV of the radar for all N_s samples. The FOV of the radars is simulated as a rectangle as seen in Figure 5.6, where the red dashed line represents the simulated FOV and the blue shaded area represents the typical FOV of a real-world radar. Thus, for each transmitter-receiver pair, N_s matrices of size $(2r_{\max} + 1) \times (r_{\max} + 1)$ are obtained meaning the resolution is $1\,\mathrm{m}$.

The Fourier basis is selected as the basis function since it is well-know and is separable. Furthermore, this allows for (5.11) to be calculated as the 2D Fourier transform:

$$\mathcal{F}_{h \to h'}\left\{\left(\beta^{(l,g,m,j,k)}\right)^*[h]\right\} = \left\langle \mathbb{F}^{(m,j,k)}(x,y,h'), \left(\psi_n^{(l,g)}\right)^*(x,y)\right\rangle \tag{5.13}$$

$$= \iint \mathbb{F}^{(m,j,k)}(x,y,h')\psi_n^{(l,g)}(x,y)\,\mathrm{d}x\mathrm{d}y \tag{5.14}$$

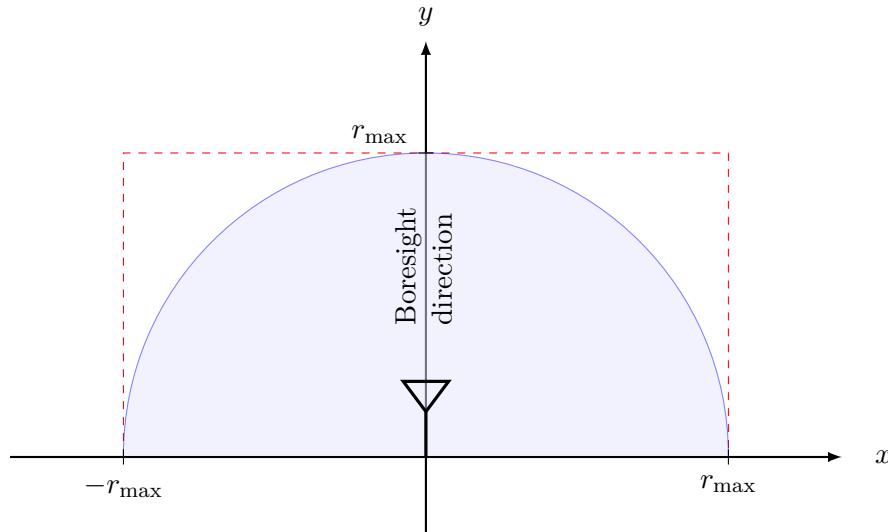$$= \mathcal{F}_{(x,y)\to(l,g)}\left\{\mathbb{F}^{(m,j,k)}(x,y,h')\right\}. \tag{5.15}$$

Figure 5.6. Illustration of the radar's FOV in the local coordinate system. The blue shaded area represents the typical FOV of a real-world radar, while the red dashed line indicates the FOV used in the simulations.

Figure 5.7 shows the process, which yields all expansion coefficients for all basis functions $\Psi_{(2r_{\max}+1)(r_{\max}+1)}$. From this set of expansion coefficients, the values corresponding to the basis functions in Ψ_{N_B} are then subsampled. This should be repeated for all N_s samples across all transmitter-receiver pairs, where all the resulting expansion coefficient are gathered in $\boldsymbol{M}^{(k)}$. Section C.2 shows how these expansion coefficients are organised in $\boldsymbol{M}^{(k)}$. Having computed $\boldsymbol{M}^{(k)}$, the received signal for the clutter is calculated as $\boldsymbol{M}^{(k)}\boldsymbol{\Gamma}^{(k)}$.
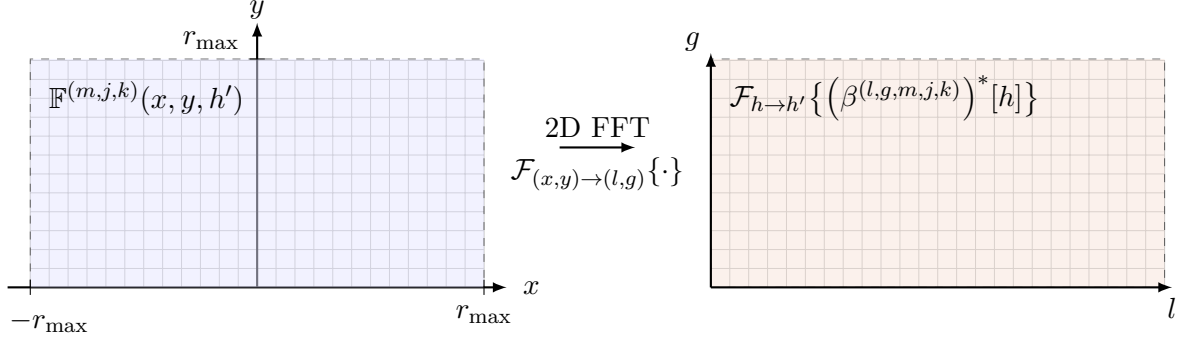

Figure 5.7. Illustration of how the expansion coefficients are obtained from the $\mathbb{F}^{(m,j,k)}(x,y,h')$ signals.

To test the clutter signal generator, it is desired to compare the clutter signal to the output of the target signal. Consequently, a field is generated for a radar in $[0\ 0]^\top$m. The field is 0 for $(-r_{\max}, r_{\max}) \times (0, r_{\max})$ except for $[x\ y]^\top = [0\ 30]^\top$m where $C(0, 30) = 1$. From this field, $\boldsymbol{\Gamma}^{(k)}$ is generated using the analysis equation Equation 3.39. This $\boldsymbol{\Gamma}^{(k)}$ is used to generate the clutter signal $\boldsymbol{M}^{(k)}\boldsymbol{\Gamma}^{(k)}$. To compare it with $\boldsymbol{S}^{(k)}$, we let $\alpha = 1$ and place the target in $[x\ y]^\top = [0\ 30]^\top$m. From Figure 5.8, the two signals are the same.

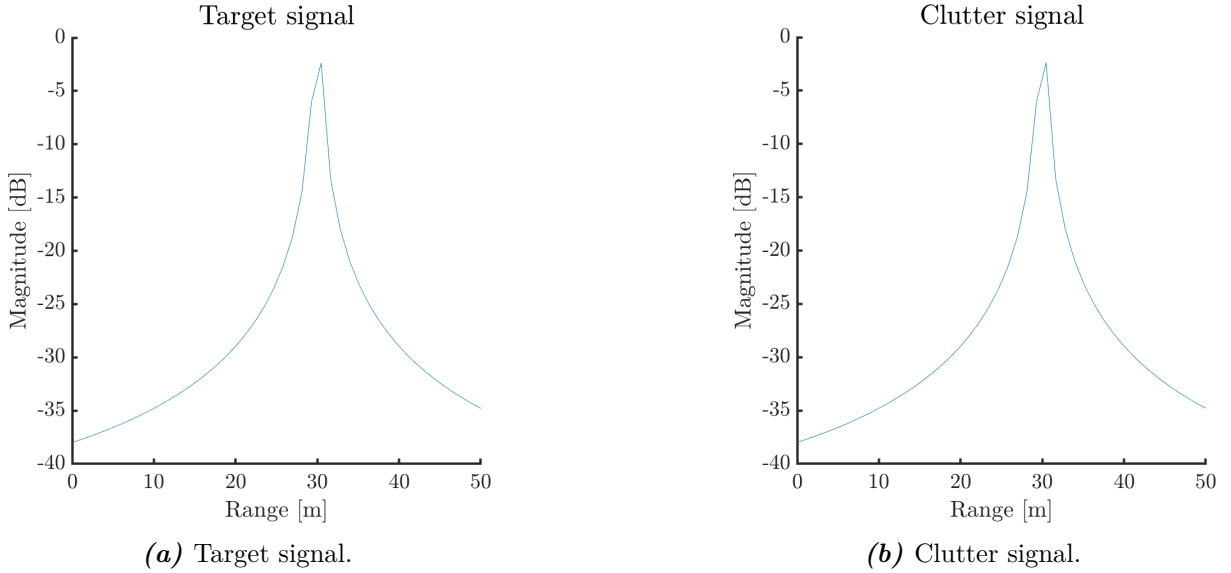**(a)** Target signal.

(b) Clutter signal.

Figure 5.8. Comparison of the target signal and the clutter signal.

Example 5.1.2 (Clutter Environment with no Target)
Looking at the C0T scenario for $N_{\mathrm{radar}} = 1$, where the radar is placed at $[0\ 0]^\top$m and the clutter field is given as in Figure 5.3, results in Figure 5.9. The plot is generated by calculating $\left|\boldsymbol{S}^{(1)}(\phi_n)^\dagger \boldsymbol{Z}_n^{(1)}\right|$, where the x- and y-coordinate in ϕ_n are evaluated across a grid.
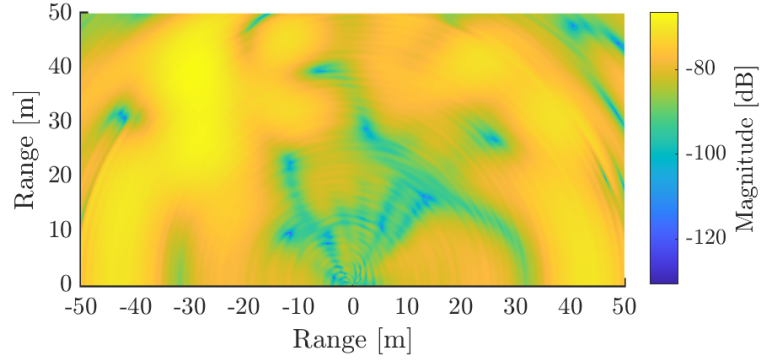
Figure 5.9. Plot of $\left| \boldsymbol{S}^{(1)}(\boldsymbol{\phi}_n)^\dagger \boldsymbol{Z}_n^{(1)} \right|$ with varying $\boldsymbol{\phi}_n$. The radar is placed at $[0\ 0]^\top$m in the C0T scenario using the clutter field from Figure 5.3.

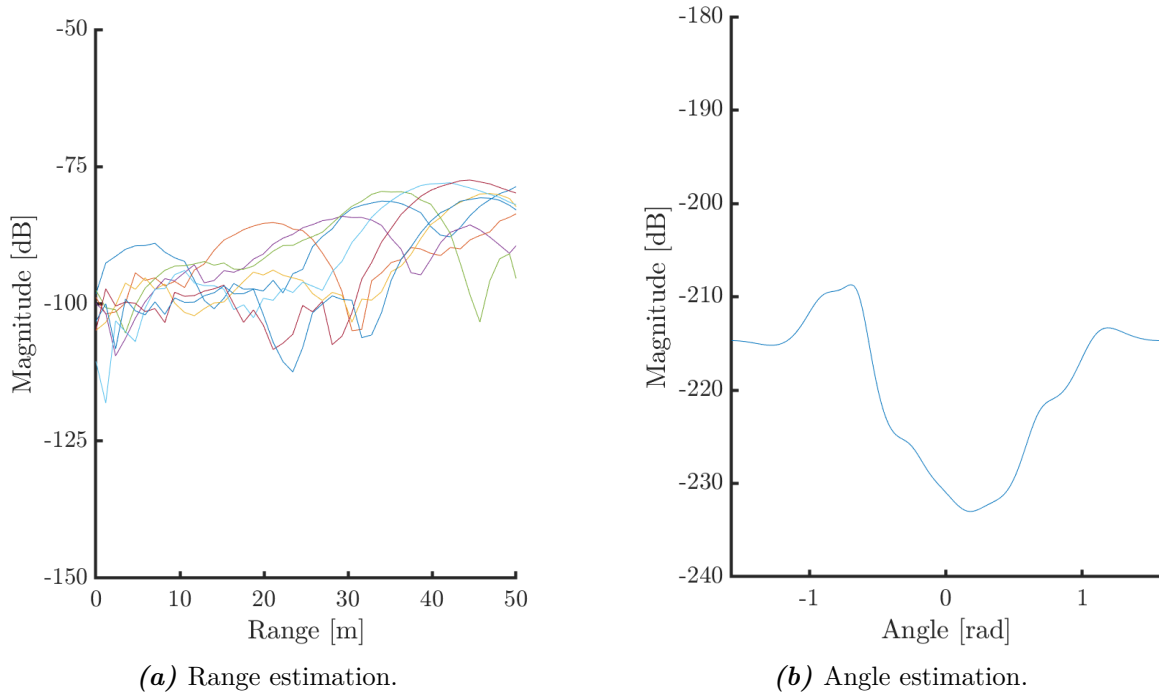Plots of the range and angle estimations are depicted in Figure 5.10.

(a) Range estimation.   *(b)* Angle estimation.

Figure 5.10. Range and angle estimation. The radar is placed at $[0\ 0]^\top$m in the C0T scenario using the clutter field from Figure 5.3.

Note that the clutter field for each radar is generated from $\boldsymbol{\Gamma}^{(k)}$ where $\boldsymbol{\Gamma}^{(k')}$ and $\boldsymbol{\Gamma}^{(k)}$ are generated independently. Thus, discrepancies can occur in the global clutter field if the FOVs of two radars overlap. An example of this is shown in Figure 5.11, where two clutter fields have been generated for a radar in $[0\ 0]^\top$m and a radar in $[0\ 40]^\top$m. Here, it is seen that there is a discrepancy between the two radars in the overlapping area $(x, y) \in (-10, 50) \times (0, 50)$.

5.1.3 Generation of Total Signal

The target and clutter signal is generated separately, so to generate the combined signal, the two separate signals are added together. Note that the noise is added to either of the signals. Thus, noise should only be added to one of the signal in the C1T scenario.
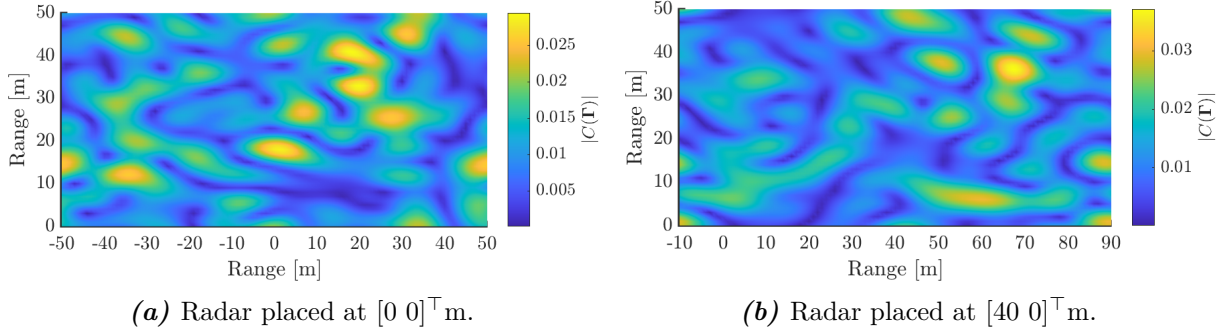
(a) Radar placed at $[0\ 0]^\top$m.   **(b)** Radar placed at $[40\ 0]^\top$m.

Figure 5.11. Example of two clutter fields for two radars with overlapping FOV.

Example 5.1.3 (Clutter Environment with one Target)

Looking at the C1T scenario for $N_{\text{radar}} = 1$, where the radar is placed at $[0\ 0]^\top$m, the target is in position $[x_n^{(k)}\ y_n^{(k)}]^\top = [3\ 20]^\top$m, and the clutter field is given as in Figure 5.3, results in Figure 5.12. The plot is generated by calculating $\left|\boldsymbol{S}^{(1)}(\boldsymbol{\phi}_n)^\dagger \boldsymbol{Z}_n^{(1)}\right|$, where the x- and y-coordinate in $\boldsymbol{\phi}_n$ are evaluated across a grid.
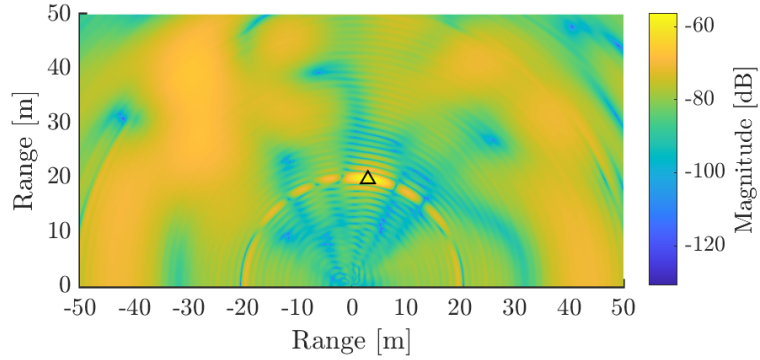
Figure 5.12. Plot of $\left|\boldsymbol{S}^{(1)}(\boldsymbol{\phi}_n)^\dagger Z_n^{(1)}\right|$ with varying $\boldsymbol{\phi}_n$. The radar is placed at $[0\ 0]^\top$m in the C1T scenario with $[x_n^{(k)}\ y_n^{(k)}]^\top = [3\ 20]^\top$m using the clutter field from Figure 5.3. The ground truth position of the target is marked with a triangle.

The range and angle estimates based on the received signals are

$$\hat{r}_n^{(k)} = 20\,\text{m}, \qquad \hat{\theta}_n^{(k)} = 0.15\,\text{rad}, \tag{5.16}$$

which aligns with the true range and angle of the target. Plots of the range and angle estimations are depicted in Figure 5.13.
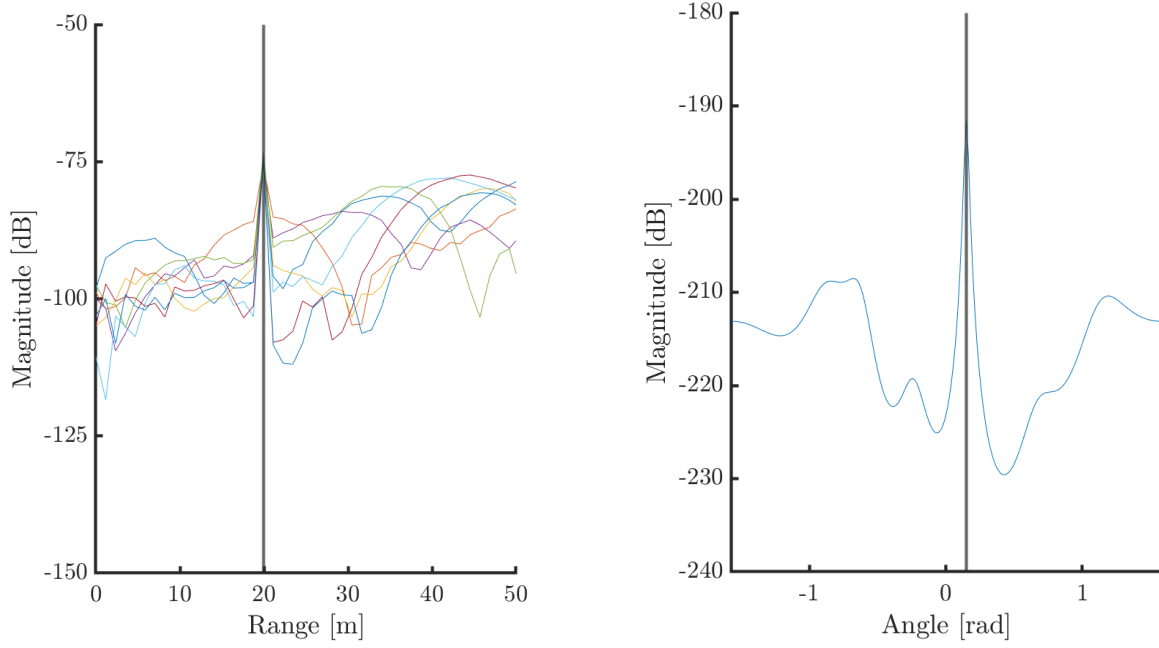
(a) Range estimation. The black vertical line represents the true range.

(b) Angle estimation. The black vertical line represents the true angle.

Figure 5.13. Range and angle estimation. The radar is placed at $[0\ 0]^\top$ m in the C1T scenario with $[x_n^{(k)}\ y_n^{(k)}]^\top = [3\ 20]^\top$ m using the clutter field from Figure 5.3.

Converting the range and angle to Cartesian coordinates using (5.6) yields

$$\hat{x}_n^{(k)} = 3\,\text{m}, \qquad \hat{y}_n^{(k)} = 20\,\text{m}. \tag{5.17}$$

5.2 Implementation of Multiple Radar Clutter and Target Bayesian Localisation and Tracking Algorithm

Algorithm 1 is implemented using the messages derived in Section 4.2 and Section B.1. The algorithm takes the received signals $\boldsymbol{Z}_{0:N}^{1:N_{\text{radar}}}$ as inputs and outputs the estimate of $\boldsymbol{\phi}_{0:N}$ and $\boldsymbol{\Gamma}_{0:N}^{1:N_{\text{radar}}}$. The algorithm consists of two parts: clutter tracking and target tracking, each implemented individually. When combining them, note that clutter tracking must be implemented first, as $\boldsymbol{\Gamma}_n^{1:N_{\text{radar}}}$ is required in the target tracking to calculate $\check{\boldsymbol{Z}}_N^{(k)}$.

As discussed in Section 4.2.1, the clutter field is modelled as a local clutter field. This means each radar has it own set of clutter field parameters that needs to be estimated. On the other hand, the target parameters are global, meaning the statistics of the messages needs to be sent from one radar to the others in order to make the global estimate based on all radars.

5.3 Implementation of Clutter Tracking Algorithm

The red parts of Algorithm 1 corresponds to the clutter tracking. For each time step n, a true $\boldsymbol{\Gamma}_n^{(k)}$ is generated to generate the received signal $\boldsymbol{Z}_n^{(k)}$. After obtaining the received signal for radar k, $\boldsymbol{\Gamma}_n^{(k)}$ is estimated using the messages. This estimate is updated with each time step for all time steps up to the current $\boldsymbol{\Gamma}_{0:n}^{(k)}$.

There are two different ways to generate $\boldsymbol{\Gamma}_n^{(k)}$. The first approach, as described in Section 4.2.2, initialises $\boldsymbol{\Gamma}_0^{(k)}$ from a Gaussian distribution with mean $\boldsymbol{\mu}_C$ and covariance $\boldsymbol{\Lambda}_C^{-1}$, after which subsequent $\boldsymbol{\Gamma}_n^{(k)}$ are generated based on the Markov chain in (4.24). When generating $\boldsymbol{\Gamma}_n^{(k)}$ using the Markov chain, κ controls the correlation between successive values. As $\kappa \to 0$, $\boldsymbol{\Gamma}_n^{(k)}$ become increasingly different, while $\kappa \to 1$ results in more similar values of $\boldsymbol{\Gamma}_n^{(k)}$. An example of this is seen in Figure 5.14. To ensure the assumptions of $\boldsymbol{\Gamma}_n^{(k)}$ follows the Markov chain, the clutter signal is generated based on these values. This approach is used to confirm that the method works under the model's assumptions. The second method generates not only the initial $\boldsymbol{\Gamma}_0^{(k)}$ from a Gaussian distribution with mean $\boldsymbol{\mu}_C$ and covariance $\boldsymbol{\Lambda}_C^{-1}$, but also subsequent $\boldsymbol{\Gamma}_n^{(k)}$ from the same distribution. This method allows for generating $\boldsymbol{\Gamma}_n^{(k)}$ which do not follow the assumed Markov chain.

The Moore-Penrose inverse is implemented using MATLAB's `svds` function and used to calculate $(\boldsymbol{M}^{(k)})^+$ from $\boldsymbol{M}^{(k)}$. This function performs a singular value decomposition for a given matrix and returns the left singular vectors U, diagonal matrix S of singular values, and right singular vectors V. This function also allows for choosing the amount of singular values. This enables a computationally simple and accurate way to compute the inverse. Figure 5.15 shows that the signal created from the singular value decomposition of $\boldsymbol{M}$ and the true $\boldsymbol{\Gamma}_n$ are very close to the true clutter signal $\boldsymbol{Z}_C$.

5.3.1 Target Tracking

The blue parts of Algorithm 1 corresponds to the target tracking. After obtaining the received signal and the estimate of the clutter field, the path loss α is estimated by (4.49) and the KL divergence in (4.50) is minimised. This optimisation is computed numerically in a four-dimensional space as both the mean and variance in terms of x and y is found. The bounds for the optimisation method are given as

$$-r_{\max} \le \mu_x \le r_{\max}, \qquad 0 \le \mu_y \le r_{\max}, \qquad 0 \le \sigma_x \le v_{\max}, \qquad 0 \le \sigma_y \le v_{\max}. \tag{5.18}$$

(a) $\boldsymbol{\Gamma}_1, \boldsymbol{\Gamma}_{10}$, and $\boldsymbol{\Gamma}_{20}$ generated with $\kappa = 0.1$.   *(b)* $\boldsymbol{\Gamma}_1, \boldsymbol{\Gamma}_{10}$, and $\boldsymbol{\Gamma}_{20}$ generated with $\kappa = 0.99$.
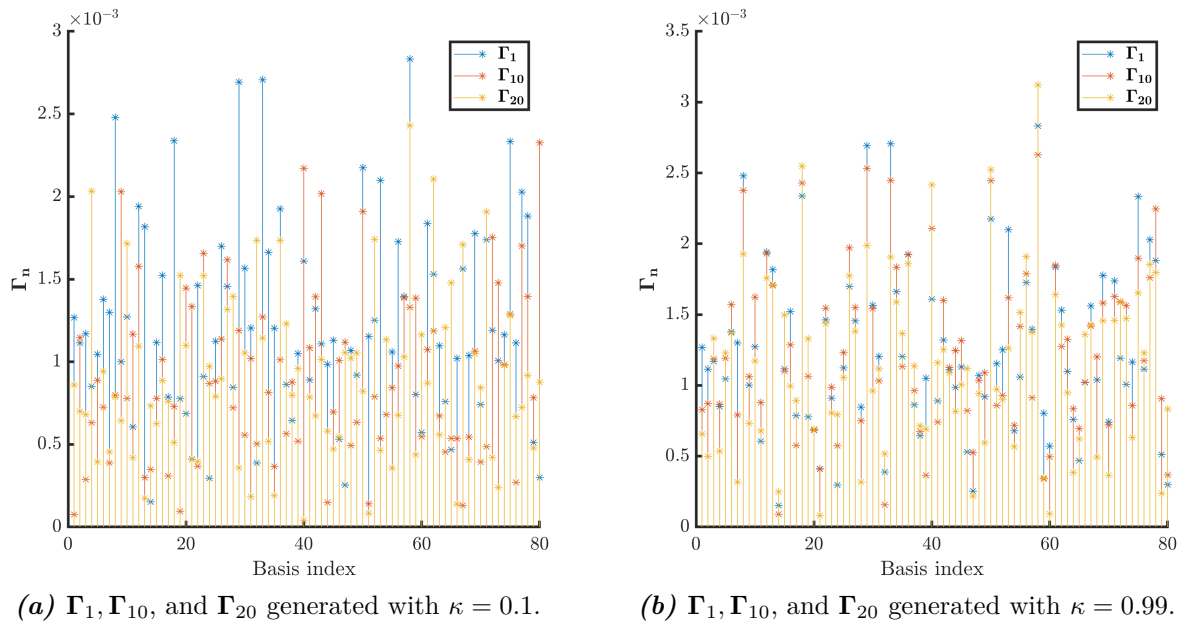
Figure 5.14. The effect of κ when generating $\boldsymbol{\Gamma}_n$.
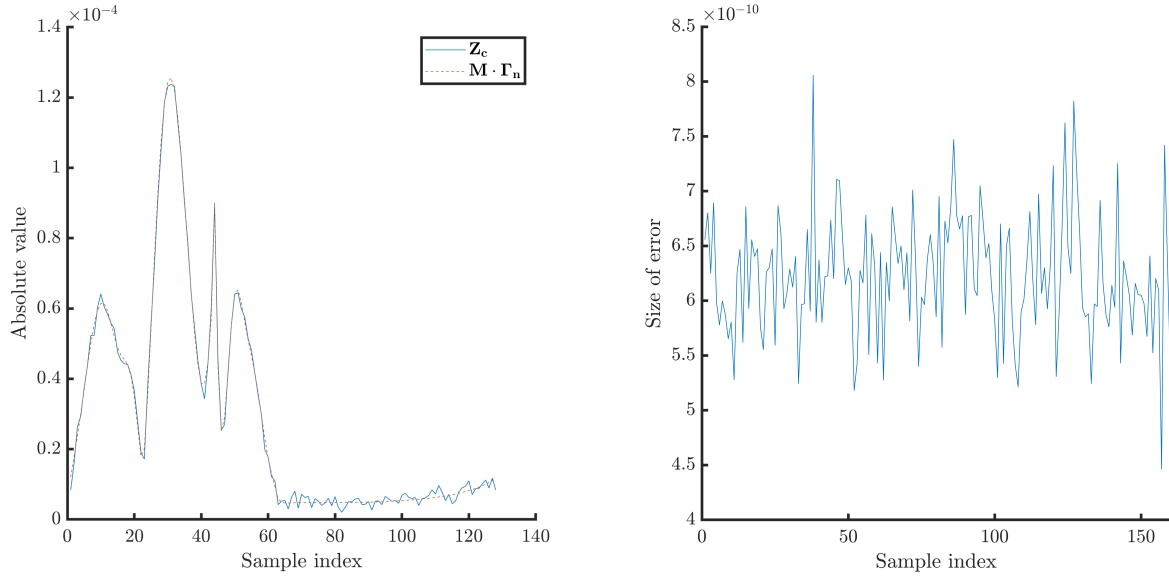
(a) The true clutter signal $\boldsymbol{Z}_C$ and the singular value decomposition clutter signal $\boldsymbol{M}^+\boldsymbol{\Gamma}_n$, with 60 singular values for one transmitter-receiver pair.

(b) The error between $\boldsymbol{Z}_C$ and $\boldsymbol{M}\boldsymbol{\Gamma}_n$, calculated as $\|\boldsymbol{Z}_C - \boldsymbol{M}\boldsymbol{\Gamma}_n\|^2$

Figure 5.15. The effects of using the singular value decomposition for calculating the Moore-Penrose inverse.

An example of (4.50) for the mean and variance is shown Figure 5.16, where the radar is placed at $[0\ 0]^\top$m and the target is in position $[3\ 20]^\top$m .

The minimum of (4.50) is found using MATLAB's `fmincon` function. This function is used to find the minimum of constrained non-linear multivariable functions. The default optimisation algorithm of the function is `interior-point` which is also used in our case. This algorithm approaches the solution from the interior of the feasible region by incorporating constraints into the objective function using a barrier method. The barrier method is an optimisation technique that prevents constraint violations by adding a penalty term to the objective function, which grows rapidly near the boundary of the feasible region. The optimisation method will not be elaborated further as it is out of scope of the project.

The optimisation of (4.50) is performed in the local coordinate system of each radar. Since the MRBLaT algorithm runs in a global coordinate system, the local solution of the optimisation needs to be translated to the global coordinate system. The relation between the local and global
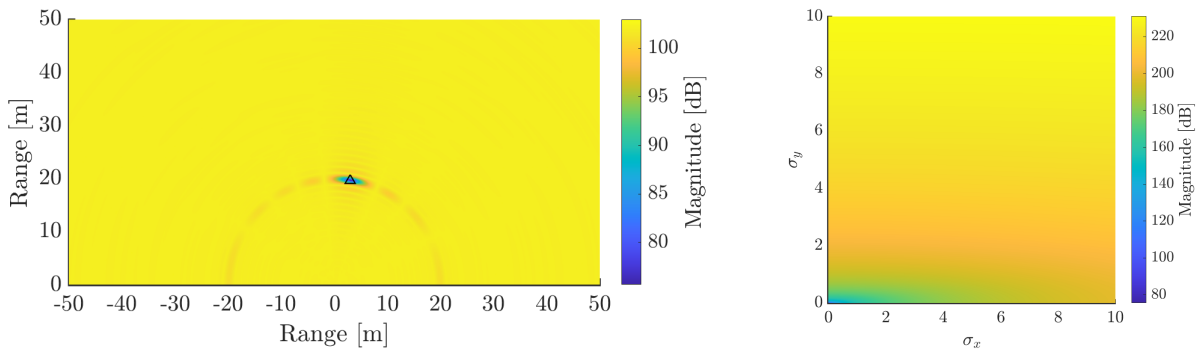
(a) Mean. The ground truth position is marked with a triangle.

(b) Variance.

Figure 5.16. Illustration of (4.50), where the radar is placed at $[0\ 0]^\top$m and the target is in position $[3\ 20]^\top$m .

coordinate system is depicted in Figure 3.3. The mean is translated as

$$
\begin{bmatrix} \mu_x^{(k)} \\ \mu_y^{(k)} \end{bmatrix} = \begin{bmatrix} x_{\text{radar}}^{(k)} \\ y_{\text{radar}}^{(k)} \end{bmatrix} + Q \cdot \begin{bmatrix} \hat{\mu}_x^{(k)} \\ \hat{\mu}_y^{(k)} \end{bmatrix},
\tag{5.19}
$$

where $[x_{\text{radar}}^{(k)} \; y_{\text{radar}}^{(k)}]^\top$ is the position of the radar, $[\hat{\mu}_x^{(k)} \; \hat{\mu}_y^{(k)}]^\top$ is the first two entries of solution from the optimisation, and

$$
Q = \begin{bmatrix} \cos(\Theta) & -\sin(\Theta) \\ \sin(\Theta) & \cos(\Theta) \end{bmatrix},
\tag{5.20}
$$

is the rotation matrix of the radar, where Θ denotes the angle measured clockwise from the positive y-direction with respect to the centre of the radar - see Figure 3.3. The variance is translated as

$$
\begin{bmatrix} \sigma_x^{(k)} \\ \sigma_y^{(k)} \end{bmatrix} = \sqrt{\text{diag}\left(Q \cdot \begin{bmatrix} \left(\hat{\sigma}_x^{(k)}\right)^2 & 0 \\ 0 & \left(\hat{\sigma}_y^{(k)}\right)^2 \end{bmatrix} \cdot Q^\top \right)},
\tag{5.21}
$$

where $\hat{\sigma}_x^{(k)}$ and $\hat{\sigma}_y^{(k)}$ is the variance estimate for the x- and y-coordinate respectively, and it is assumed that the covariance matrix is diagonal.

The global estimate is obtained from the globalised local estimates by using (4.101) and (4.100). Having obtained the global $\hat{\phi}_n$, the backwards smoothing is applied to obtain $\hat{\phi}_{0:n}$. Furthermore, the estimate of Λ_a is calculated using (4.55) for each MIMO FMCW radar cycle.

Target and Clutter Tracking using Bayesian Inference

<div style="text-align: right">6</div>

The MRCaTBLaT algorithm has been implemented where the goal is to track the target and clutter in a clutter environment with one target. The performance of the algorithm is evaluated on simulated data from multiple MIMO FMCW radars. It is assumed that both the target and clutter has been detected and categorised correctly as either target or clutter.

6.1 Data Simulation

The data is simulated as described in Section 5.1, where the radar settings can be seen in Table 6.1. The settings are chosen based on a TI AWR1642 radar.

The system consists of three 2×4 MIMO FMCW radars resulting in eight transmitter-receiver pairs. Each radar uses its own carrier frequency to simulate the absence of mutual interference between the radars. The carrier frequencies are chosen based on the bandwidth of the signal is 1.2 GHz. The three radars are positioned 20 m apart along the x-axis, with the first radar placed in Origo. The radar placement is outside scope of this project and will not be looked further into. The boresight direction of all radars is the positive y-direction.

The RCS of the target is based on the findings in [Sedivy and Nemec, 2021], which examined the RCS values for different drones at different angles. Taking the average of the mean values of their findings results in an RCS of $0.03 \, \text{m}^2$.

The noise power applied at the receivers is calculated as thermal noise by

$$\sigma_w^2 = k_b \cdot T_0 \cdot BW, \tag{6.1}$$

where $k_b \approx 1.38 \cdot 10^{-23} \, \text{J/K}$ is the Boltzmann constant, T_0 is the temperature in Kelvin, and BW is the bandwidth [Kingsley and Quegan, 1992, p. 42]. Using $T_0 = 290 \, \text{K}$, as it is the general assumption [Kingsley and Quegan, 1992, p. 41], with a bandwidth of 1.2 GHz yields

$$\sigma_w^2 = 1.38 \cdot 10^{-23} \, \text{J/K} \cdot 290 \, \text{K} \cdot 1.2 \, \text{GHz} = 4.8 \, \text{pW}. \tag{6.2}$$

The FOV of the radars is simulated as a rectangle as seen in Figure 5.6, where the red dashed line represents the simulated FOV and the blue shaded area represents the typical FOV of a real-world radar.

From (**??**), the SINR is calculated as

$$\text{SINR} = \frac{P_r}{P_I + P_N}, \tag{6.3}$$

Parameter	Value
Radar centres	$[0\ 0]^\top$ m, $[20\ 0]^\top$ m, $[40\ 0]^\top$ m
#Transmitters, N_T	2
#Receivers, N_R	4
Pulse repetition frequency	10 Hz
Maximum range, R_{max}	50 m
Maximum velocity, v_{max}	10 m/s
RCS of target, σ	$0.03\,\text{m}^2$
RCS model	Swerling 0
Noise power, σ_w^2	4.8 pW
Gain of antenna	1
Bandwidth	1.2 GHz
Power of transmitted signals	1 MW
#Samples, N_s	128
Chirp rate	9.994 THz/s
Sampling rate, f_s	10 GHz
Carrier frequencies	77 GHz, 78.2 GHz, 79.4 GHz
# Basis functions, N_B	80
Initial mean of $\mathbf{\Gamma}^{1:N_{\text{radar}}}$, $\boldsymbol{\mu}_{C,\text{init}}$	0
Initial precision of $\mathbf{\Gamma}^{1:N_{\text{radar}}}$, $\mathbf{\Lambda}_{C,\text{init}}$	10^6
Backwards smoothing steps	100
Monte Carlo iterations	5

Table 6.1. Settings used for simulation.

where P_r, P_I, and P_N is the power of the target signal, the clutter signal, and the noise signal, respectively. The power of the signal is written as

$$P_r = |A\alpha|^2 \tilde{S}^\dagger \tilde{S} = A^2 |\alpha|^2, \tag{6.4}$$

where $\tilde{S}$ is the received signal without the path loss and A is the amplitude of the signal. The power of the clutter signal is calculated as

$$P_I = (\boldsymbol{M\Gamma})^\dagger \boldsymbol{M\Gamma}. \tag{6.5}$$

The power of the noise signal is written as

$$P_N = \mathbb{E}\left[N^\dagger N\right], \tag{6.6}$$

where the noise is generated as

$$N = \sqrt{\frac{\sigma_w^2}{2}}(\mathcal{N}(0,1) + i\mathcal{N}(0,1)). \tag{6.7}$$

Thus,

$$P_N = \mathbb{E}\left[\frac{\sigma_w^2}{2}\left(2\mathcal{N}(0,1)^2\right)\right] = \sigma_w^2 \mathbb{E}\left[\mathcal{N}(0,1)^2\right] = \sigma_w^2. \tag{6.8}$$

6.2 Simulation Results

The implementation of Algorithm 1 is tested using two different trajectories. The two trajectories can be seen in Figure 6.1. Trajectory (A) is a vertical linear motion, where the target moves at a speed of $5\,\mathrm{m/s}$ away from the radars. This trajectory consists of 80 samples. Trajectory (B) is an S motion consisting of 29 samples. When changing direction, the circle segments are separated by a linear motion where the target comes to a full stop with a constant deceleration of $5\,\mathrm{m/s^2}$. After the full stop, the target will accelerate with a constant acceleration of $5\,\mathrm{m/s^2}$.

First, Algorithm 1 is tested part wise, meaning that the MRBLaT algorithm and clutter tracking algorithm is tested separately and then combined. Thus, it is assured that each part of the algorithm works as intended before combining them.

6.2.1 Multiple Radar Bayesian Localisation and Tracking

The MRBLaT algorithm is tested both on trajectories in Figure 6.1. For both trajectories, MRBLaT will be tested in two scenarios: CF1T and C1T. The latter scenario is chosen to see how the algorithm performs in an environment it is not designed for and to showcase the need for clutter tracking.

One Target in a Clutter-Free Environment

The results for simulating one target in a clutter-free environment based on trajectory (A) and trajectory (B) are now presented. For trajectory (A), the starting position is in $[20\ 5]^\top\mathrm{m}$, where

$$r_1^{(1)} = 20.6\,\mathrm{m}, \qquad r_1^{(2)} = 5\,\mathrm{m}, \qquad r_1^{(3)} = 20.6\,\mathrm{m}, \tag{6.9}$$

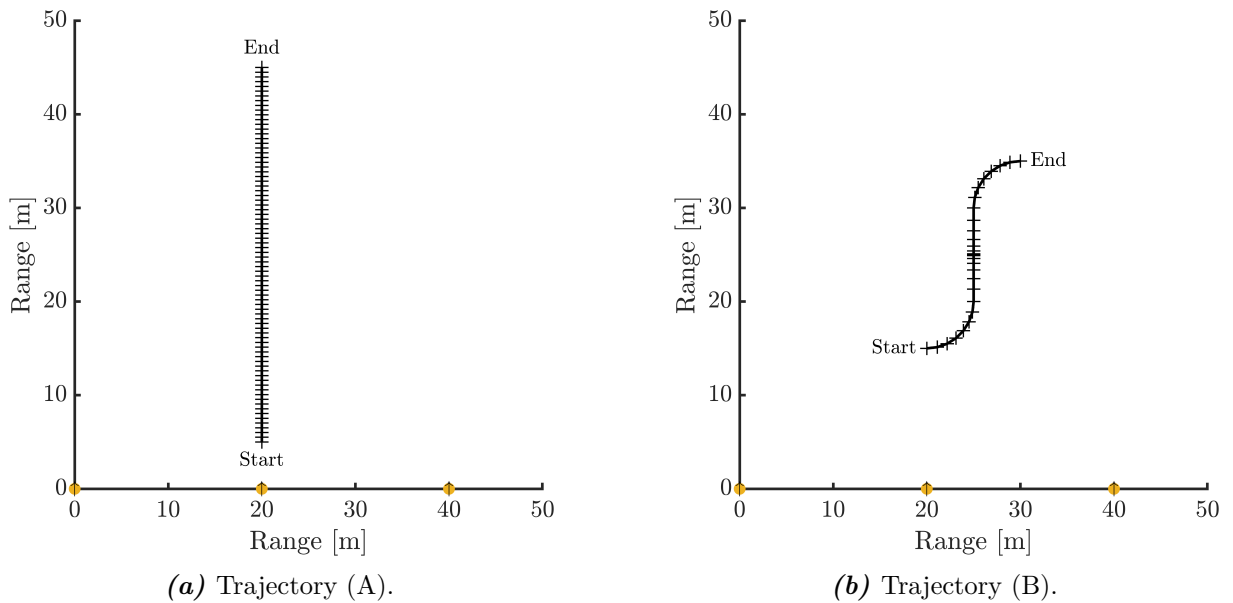*(a)* Trajectory (A).   *(b)* Trajectory (B).

Figure 6.1. Two different trajectories of a target. The yellow dots represents the radars positions and the arrow represents the boresight direction. The discretised positions are marked with +.

and,

$$\theta_1^{(1)} = 1.3 \, \text{rad}, \qquad \theta_1^{(2)} = 0 \, \text{rad}, \qquad \theta_1^{(3)} = -1.3 \, \text{rad}. \tag{6.10}$$

The received signal at this position for each radar is seen in Figure 6.2, where a peak in signal strength is observed at the correct range for each of the radars. The angle estimates in this position can be seen in Figure 6.3. Once again, it is seen that there is a peak in the ground truth.
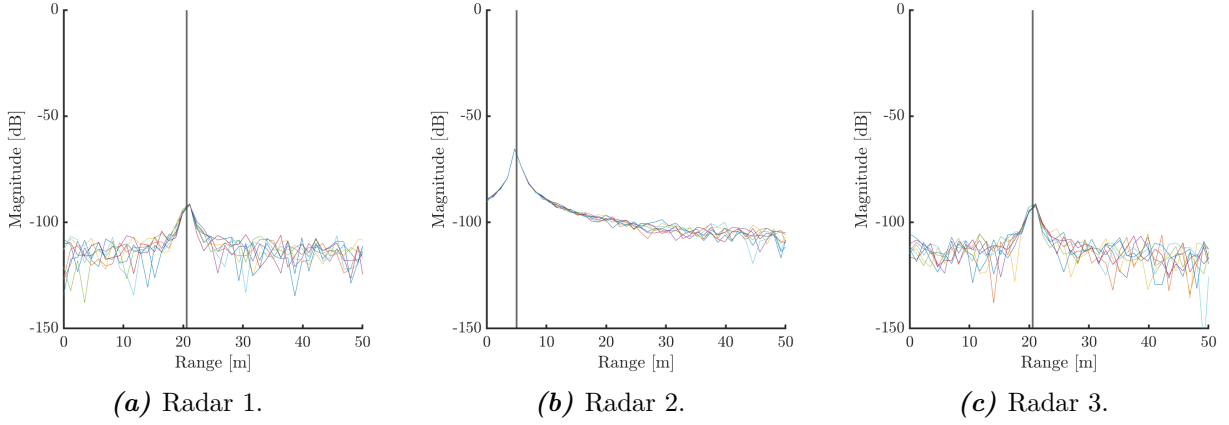

(a) Radar 1.   *(b)* Radar 2.   *(c)* Radar 3.

Figure 6.2. $\left| Z_1^{(k)} \right|$. Target is at $[x_n \ y_n]^\top = [20 \ 5]^\top \text{m}$. The black vertical line represents the ground truth range in local coordinates.

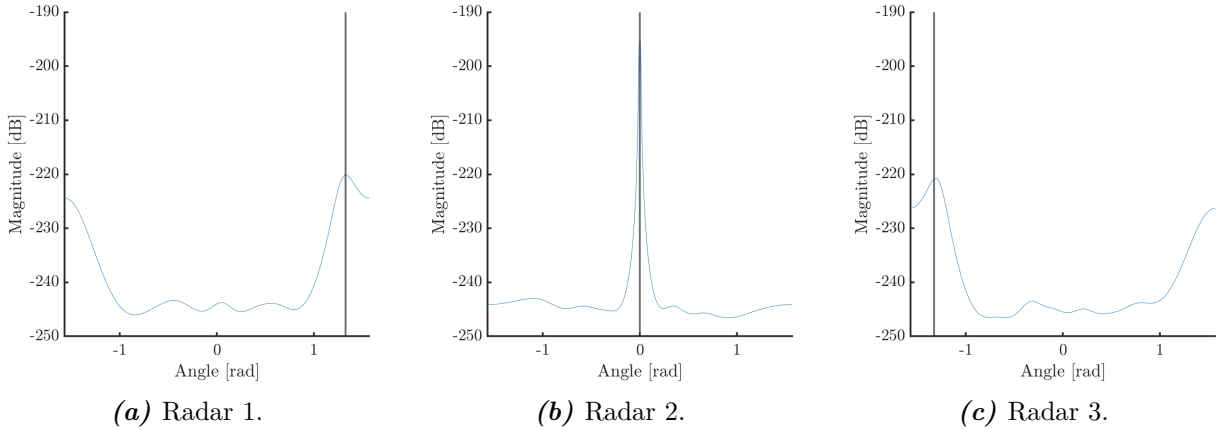*(a)* Radar 1.   *(b)* Radar 2.   *(c)* Radar 3.

Figure 6.3. Angle estimate using the Capon beamformer. Target is at $[20 \ 5]^\top \text{m}$. The black vertical line represents the ground truth range in local coordinates.

The results from running the MRBLaT algorithm is seen in Figure 6.4. For both trajectories, the MRBLaT algorithm estimate the position within $1 \, \text{m}$ as seen in Figure 6.5. From Figure 6.5a, the error of the estimated position increases when the target gets further away from the radars. Note that figures of $\left| S(\phi_1)^\dagger Z_1^{(k)} \right|$ and the KL divergence in this position for each radar is shown in Section D.1.
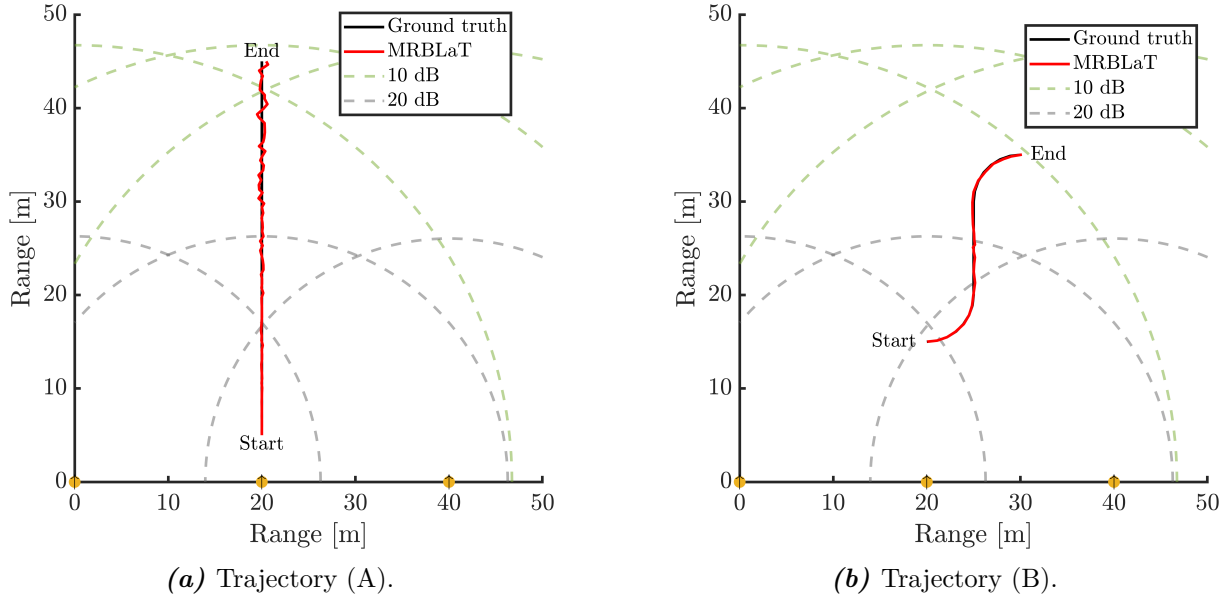
(a) Trajectory (A).

(b) Trajectory (B).

Figure 6.4. Track estimates. The yellow dots represents the radars position and the arrow represents the boresight direction.

(a) Trajectory (A).
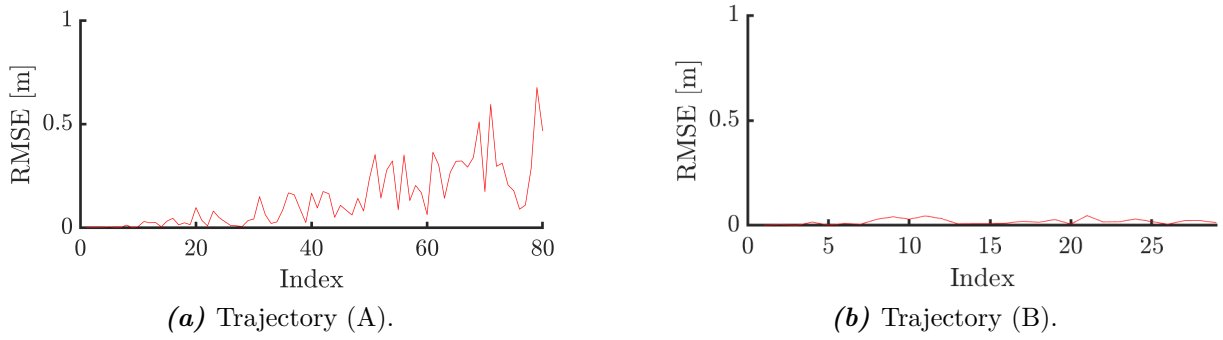

(b) Trajectory (B).

Figure 6.5. RMSE based on 5 Monte Carlo simulations.

The end position of trajectory (A) is at $[20\ 45]^\top$ m. In this position, the received signal and angle estimate is seen in Figure 6.6 and Figure 6.7, respectively. Comparing Figure 6.6 with Figure 6.2, the target signal is much less noticeable. However, it is still possible to estimate the position within less than $1\,\mathrm{m}$ of the true position. Note that figures of $\left|S(\boldsymbol{\phi}_{80})^\dagger \boldsymbol{Z}_{80}^{(k)}\right|$ and the KL divergence in this position for each radar is shown in Section D.1.

(a) Radar 1.

(b) Radar 2.

(c) Radar 3.

Figure 6.6. $\left|\boldsymbol{Z}_{80}^{(k)}\right|$. Target is at $[20\ 45]^\top$ m. The black vertical line represents the ground truth range in local coordinates.

(a) Radar 1.   *(b)* Radar 2.   *(c)* Radar 3.
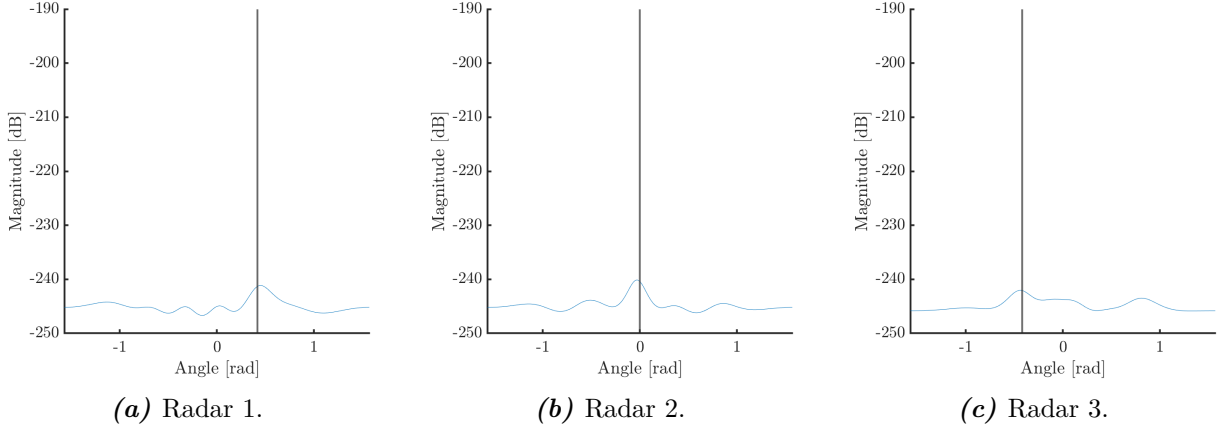
Figure 6.7. Angle estimate using the Capon beamformer. Target is at $[20\ 45]^\top$m. The black vertical line represents the ground truth range in local coordinates.

One Target in a Clutter Environment

The MRBLaT algorithm is tested in the C1T scenario, where $\boldsymbol{\Gamma}^{(k)} \sim \mathcal{N}^C(\boldsymbol{\mu}_C = 0, \boldsymbol{\Lambda}_C = 10^6)$. This yields the signals shown in Figure 6.8 and Figure 6.9. For $n = 1$ and $n = 80$ the target signal is not visible which results in a bad performance of the MRBLaT algorithm. This is seen in Figure 6.10 and Figure 6.11.

(a) Radar 1.   *(b)* Radar 2.   *(c)* Radar 3.
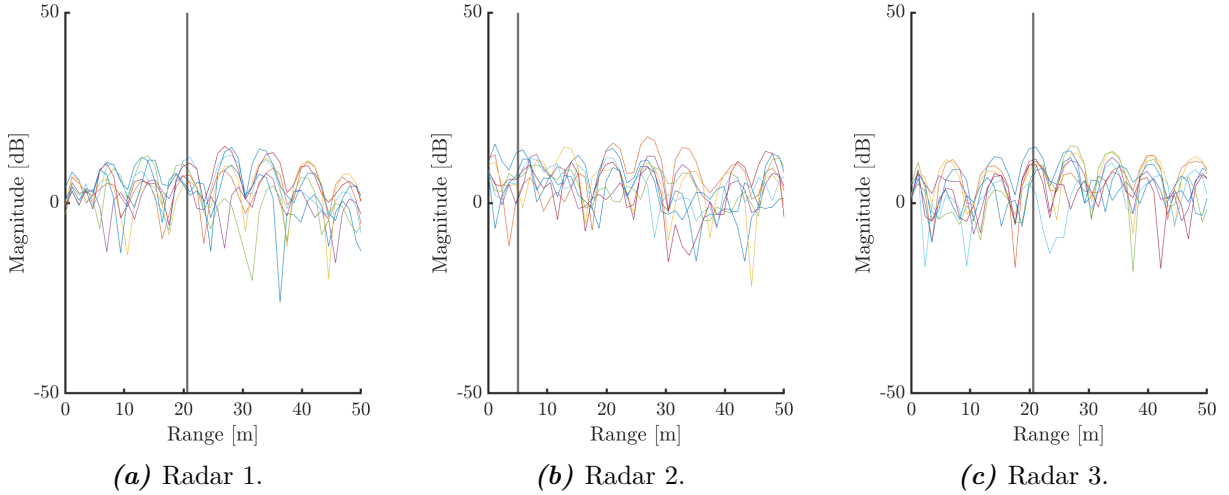
Figure 6.8. $\left|\boldsymbol{Z}_1^{(k)}\right|$. Target is at $[20\ 5]^\top$m. The black vertical line represents the ground truth range in local coordinates.
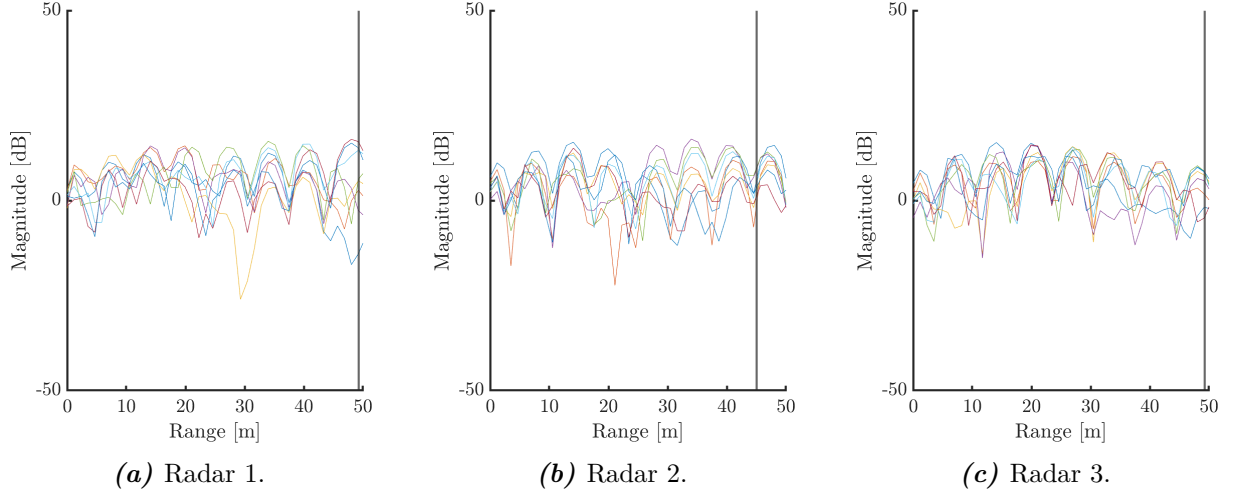
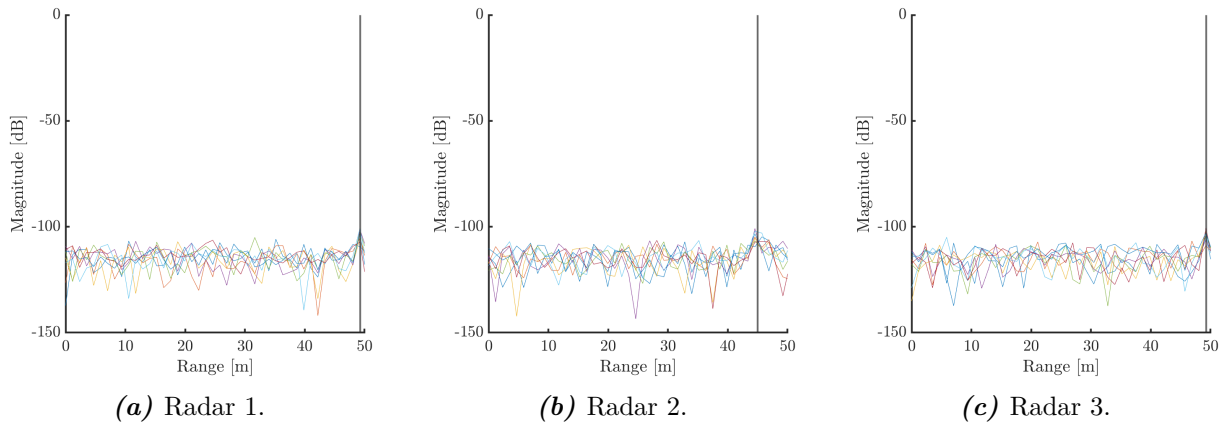***Figure 6.9.*** $\left| \boldsymbol{Z}_{80}^{(k)} \right|$. Target is at $[20 \ 45]^{\top}$m. The black vertical line represents the ground truth range in local coordinates.
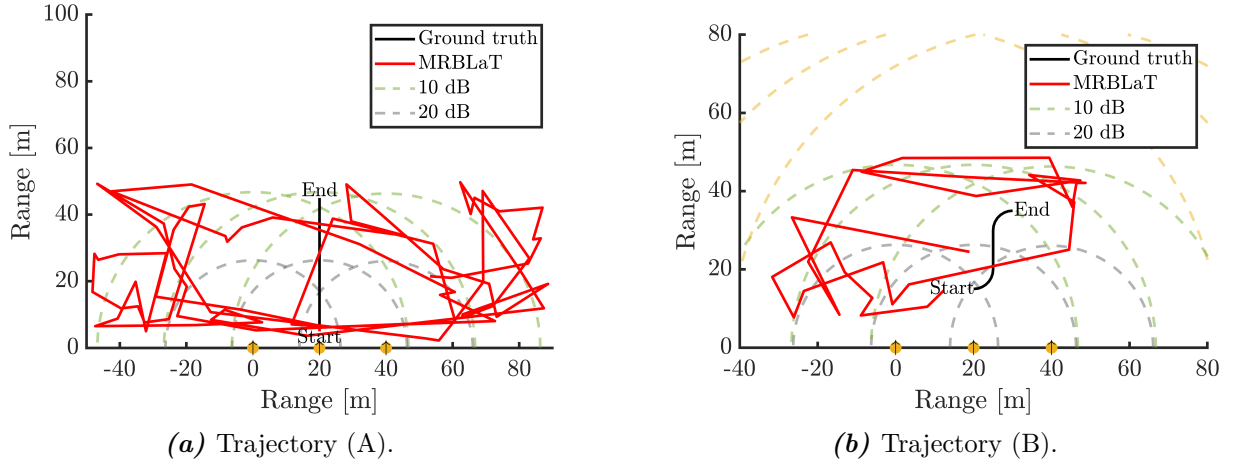

Figure 6.10. Track estimates. The yellow dots represents the radars position and the arrow represents the boresight direction.
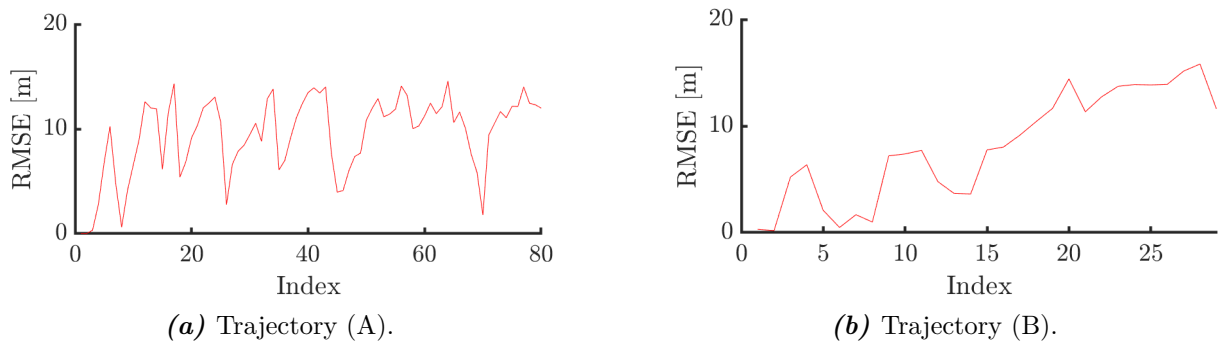
Figure 6.11. RMSE based on 5 Monte Carlo simulations.

6.3 Clutter Tracking

The clutter tracking algorithm is tested in the C0T scenario by letting $\boldsymbol{\Gamma}_n^{(k)} \sim \mathcal{N}^C(\boldsymbol{\mu}_C = 0, \boldsymbol{\Lambda}_C = 10^6)$, where $N_B = 80$ and $\boldsymbol{\Gamma}_n^{(k)}$ follows the Markov chain with $\kappa = 0.169$ based on [Westerkam et al., 2023]. The clutter tracking algorithm is only tested for $N_{\text{radar}} = 1$ since the procedure would be the same for all radars. Thus, the superscript (k) is dropped.

Now, $\mathbf{\Gamma}_n$ are estimated using Algorithm 1. Figure 6.12 shows the clutter fields based on the $\mathbf{\Gamma}_n$ and $\hat{\bar{\mathbf{\Gamma}}}_n$ for $n = 160$, where the two clutter fields are very similar.
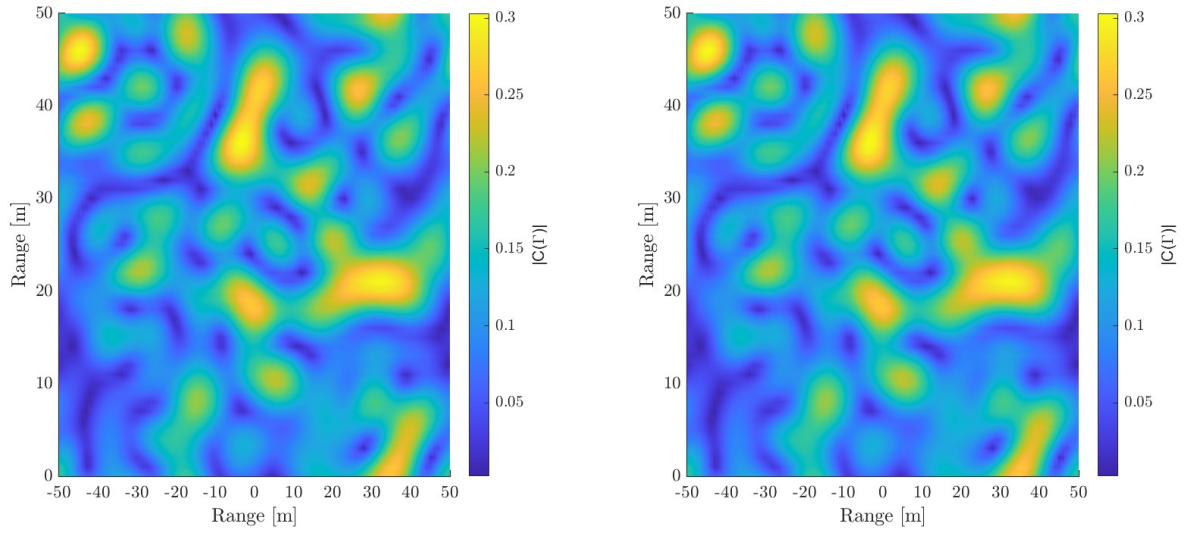
(a) Ground truth clutter field.   *(b)* Estimated clutter field.

Figure 6.12. Ground truth and estimated clutter field for $n = 160$.

In Figure 6.13, $\mathbf{\Gamma}_n$ and $\hat{\bar{\mathbf{\Gamma}}}_n$ are compared visually. For each time step n, Figure 6.14 shows this error between $\mathbf{\Gamma}_n$ and $\hat{\bar{\mathbf{\Gamma}}}_n$ calculated as

$$\mathcal{O}(\mathbf{\Gamma}_n, \hat{\bar{\mathbf{\Gamma}}}_n) = \left\| \mathbf{\Gamma}_n - \hat{\bar{\mathbf{\Gamma}}}_n \right\|^2. \tag{6.11}$$

Figure 6.13. $\mathbf{\Gamma}_n$ plotted against $\hat{\mathbf{\Gamma}}_n$ for $n = 80$. The diagonal line shows where the values ideally should lie.
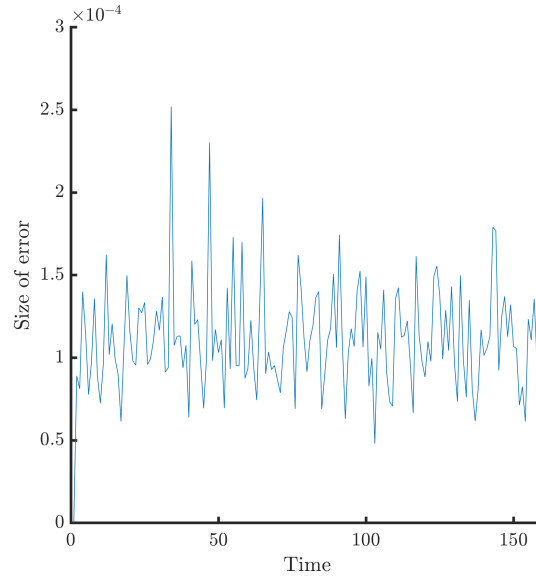
Figure 6.14. Error between $\mathbf{\Gamma}$ and $\widehat{\overline{\mathbf{\Gamma}}}$, calculated as in (6.11). This was calculated with 80 basis functions.

In Figure 6.15 it is seen that, as $n \to N$, where $N = 160$, then $\widehat{\overline{\boldsymbol{\mu}}}_C \to \boldsymbol{\mu}_C = 0$, which is the underlying mean for the clutter field. The same be said for the precision matrix $\widehat{\overline{\mathbf{\Lambda}}}_C$ as seen in ?? where $\widehat{\overline{\mathbf{\Lambda}}}_C \to \mathbf{\Lambda}_C$ as $n \to N$.
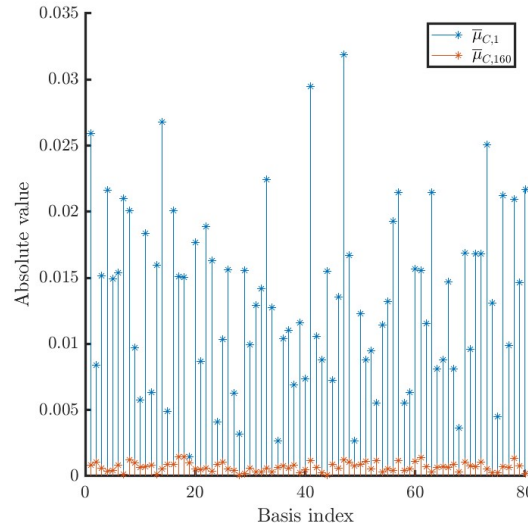
Figure 6.15. $\widehat{\overline{\boldsymbol{\mu}}}_C$ for the first and last time step.

The true signal $\boldsymbol{Z}_n$ is compared with the estimated signal $\boldsymbol{M}\widehat{\overline{\mathbf{\Gamma}}}_n$ in Figure 6.16.
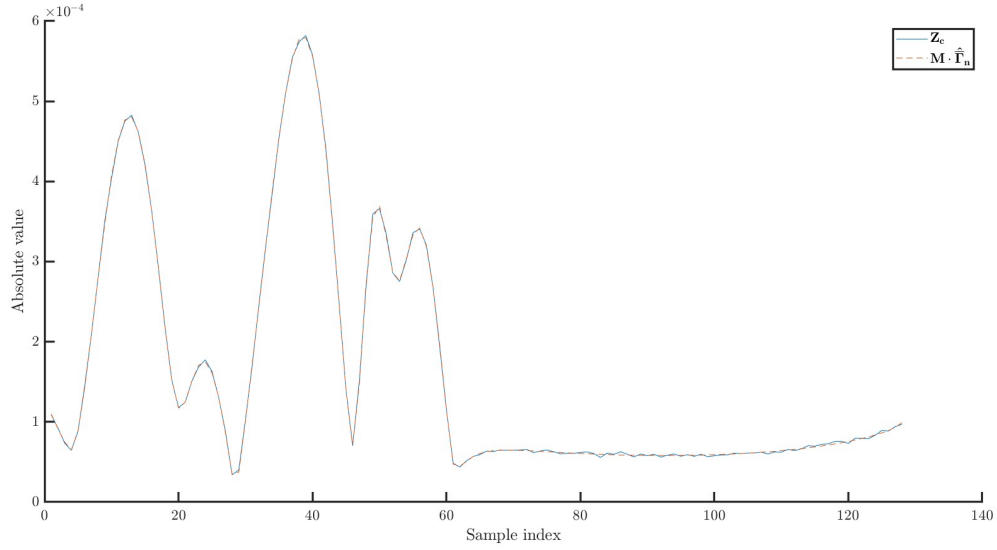
Figure 6.16. The true signal $\boldsymbol{Z}_n$ is compared with the estimated signal $\boldsymbol{M}\hat{\bar{\boldsymbol{\Gamma}}}_n$ for one transmitter-receiver pair.

When increasing the number of basis functions, $\hat{\bar{\boldsymbol{\Gamma}}}$ and $\boldsymbol{\Gamma}$ become less similar as seen in Figure 6.18. Similarly, $\hat{\bar{\boldsymbol{\Gamma}}}$ and $\boldsymbol{\Gamma}$ become more similar when decreasing the number of basis functions as seen in Figure 6.18.
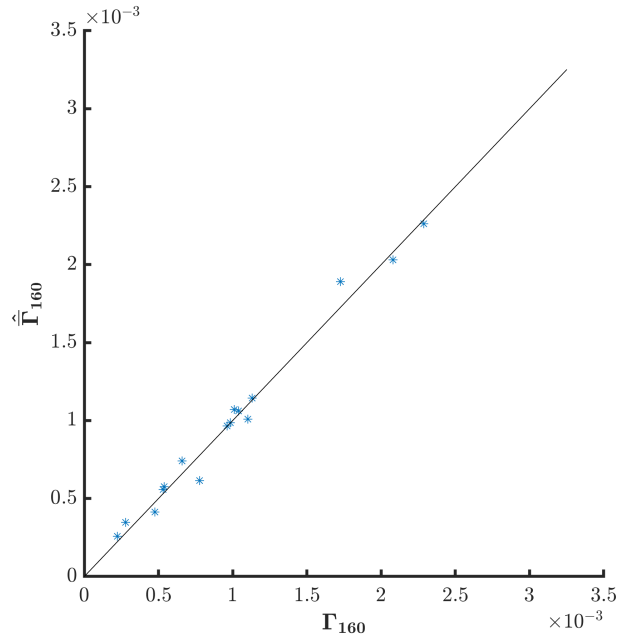
Figure 6.17. $\boldsymbol{\Gamma}_n$ plotted against $\hat{\boldsymbol{\Gamma}}_n$ for $n = 160$ and $N_B = 16$. The diagonal line shows where the values ideally should lie.
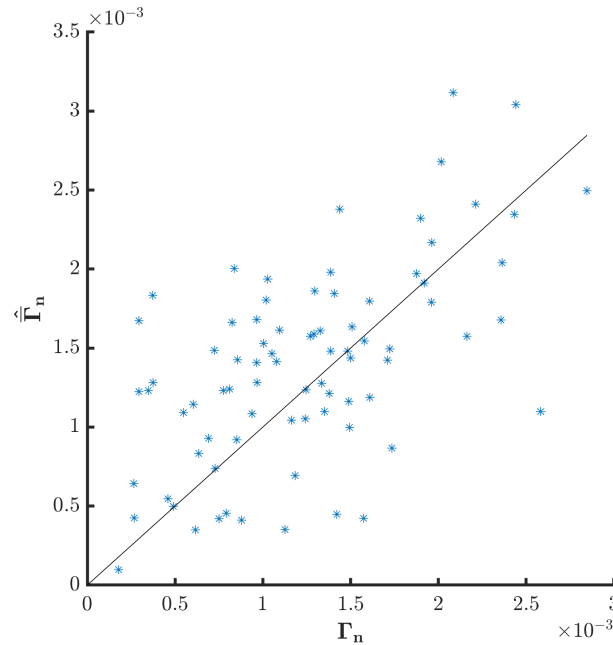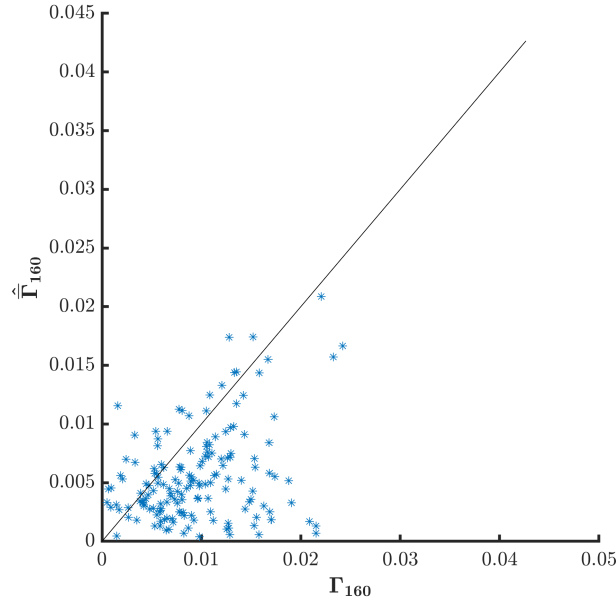
Figure 6.18. $\mathbf{\Gamma}_n$ plotted against $\hat{\mathbf{\Gamma}}_n$ for $n = 160$ and $N_B = 16$. The diagonal line shows where the values ideally should lie.

6.4   Clutter and Target Tracking

The MRBLaT algorithm and the clutter tracking algorithm function as intended, thus they are now combined. The following results focuses on target tracking.

The MRCaTBLaT algorithm is tested in the C1T scenario, where $\mathbf{\Gamma}^{(k)} \sim \mathcal{N}^C(\boldsymbol{\mu}_C = 0, \boldsymbol{\Lambda}_C = 10^6)$. This yields the signals shown in Figure 6.19 and Figure 6.20 for the first and last position in trajectory (A). This shows that it is possible to see the target signal in the total signal, but overall the clutter..

The results from running the MRCaTBLaT algorithm is shown in Figure 6.21. Here it is seen that the algorithm is able to track the target in a C1T scenario. For both trajectories, the MRCaTBLaT algorithm estimate the position within $0.05\,\mathrm{m}$ as seen in Figure 6.22.

Using $N_B = 180$ to estimate trajectory (A) gives the results in **??**.
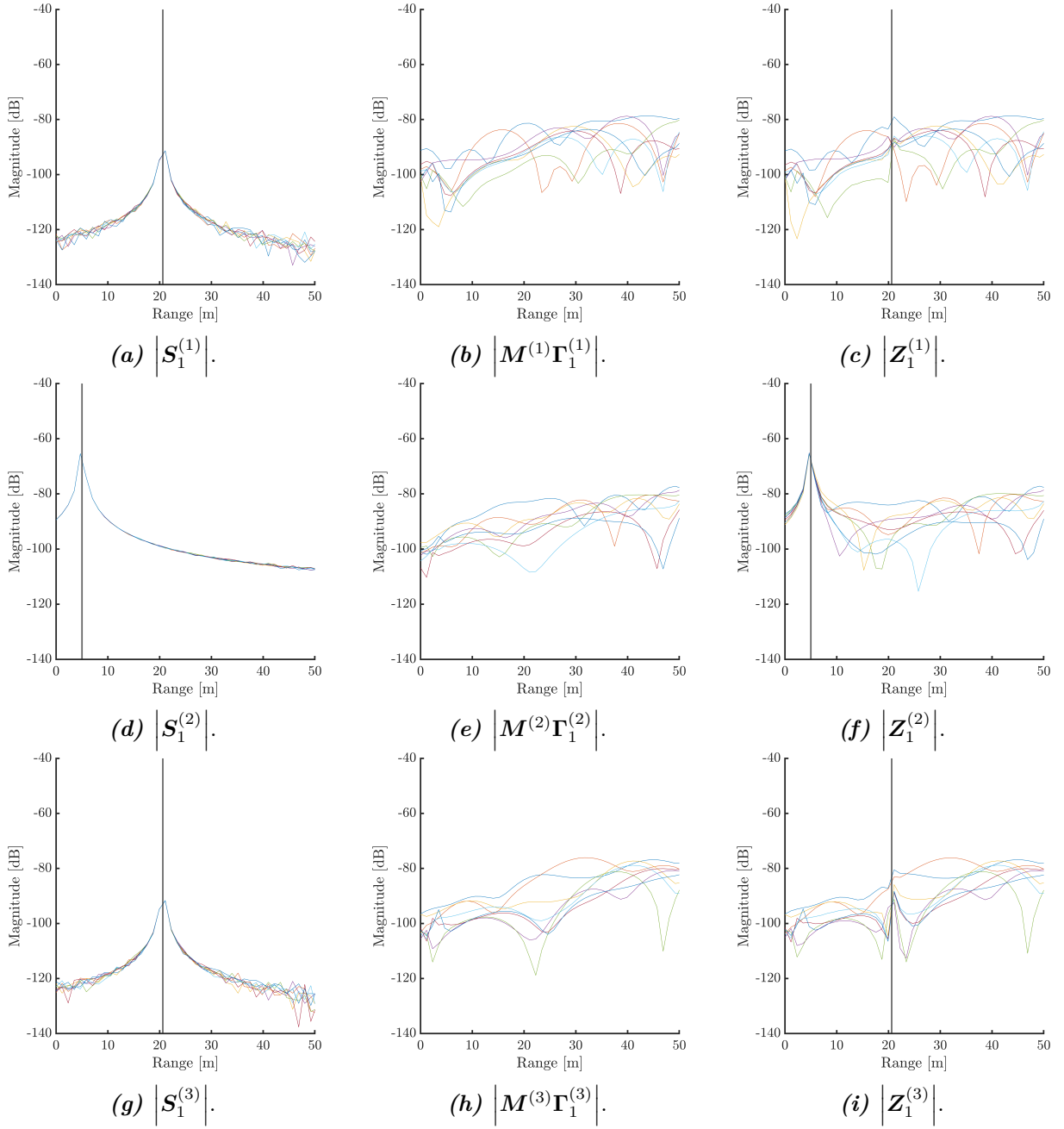
Figure 6.19. Absolute value of the target, clutter, and total signal. Target is at $[20 \; 5]^{\top}$ m. The black vertical line represents the ground truth range in local coordinates.
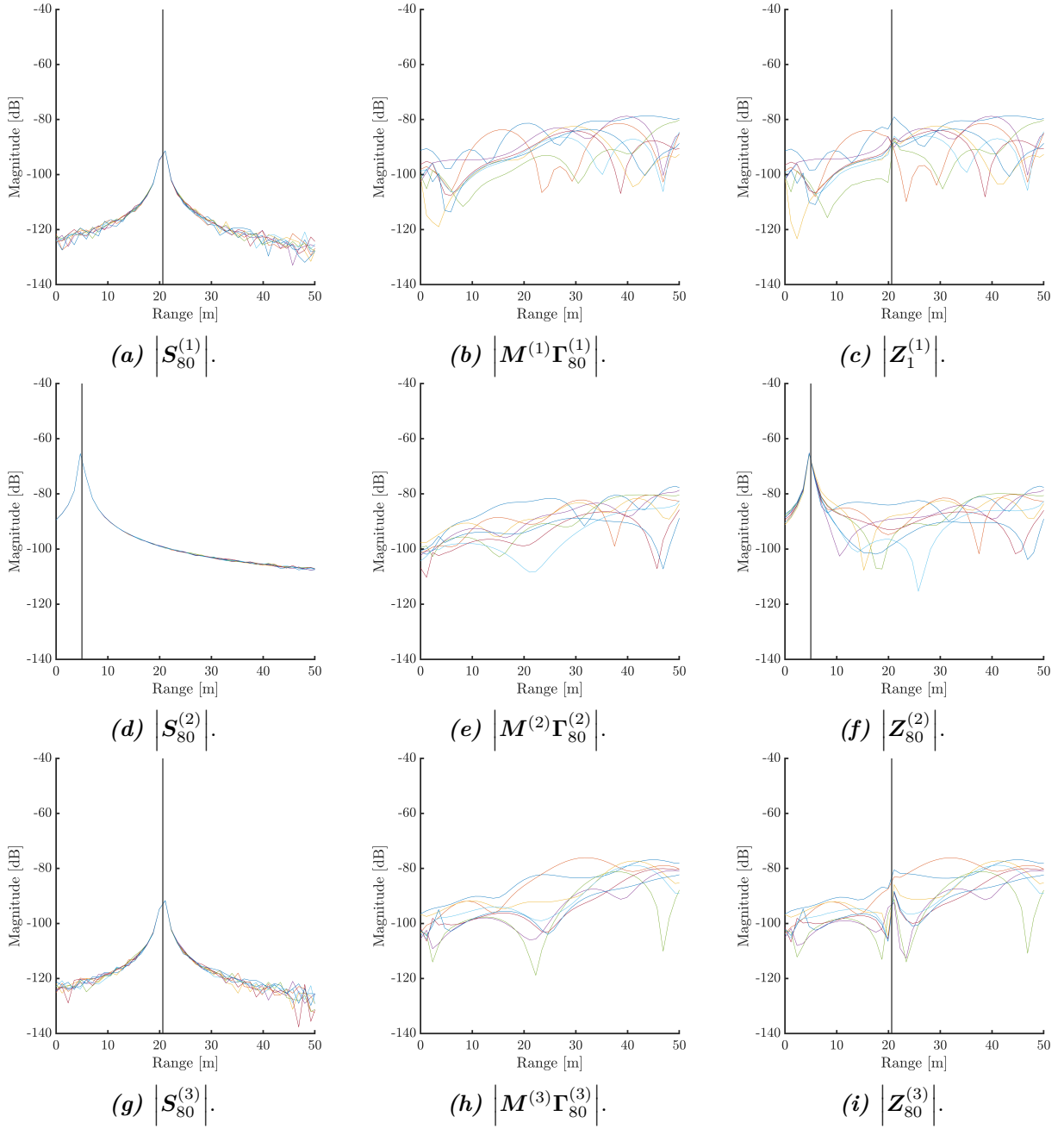
Figure 6.20. Absolute value of the target, clutter, and total signal. Target is at $[20\ 45]^\top$ m. The black vertical line represents the ground truth range in local coordinates.

(a) Trajectory (A).

(b) Trajectory (B).
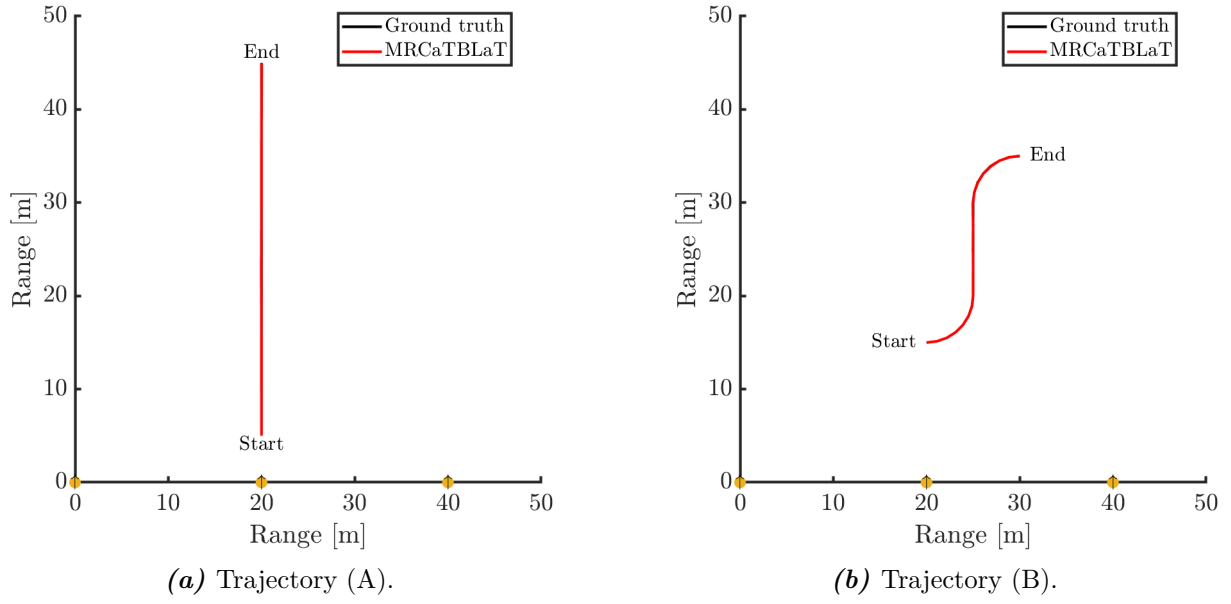
Figure 6.21. Track estimates. The yellow dots represents the radars position and the arrow represents the boresight direction.

(a) Trajectory (A) estimate. The yellow dots represents the radars position and the arrow represents the boresight direction.

(b) Trajectory (B).
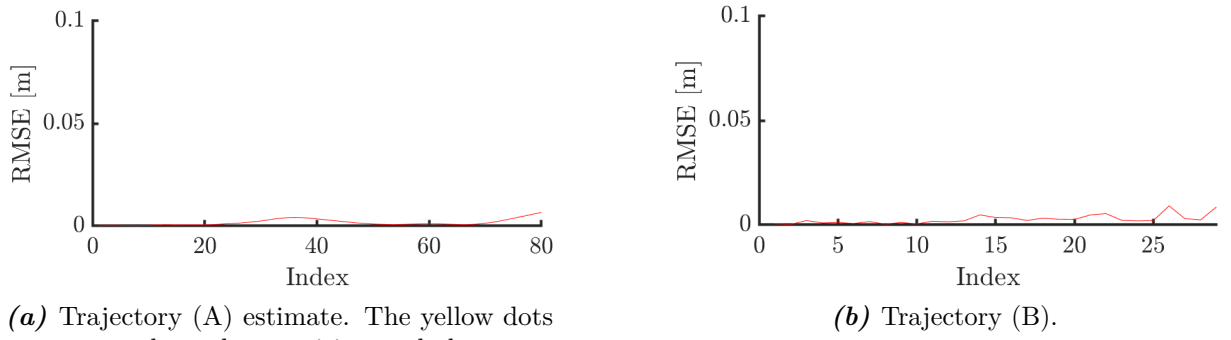
Figure 6.22. MRCaTBLaT results using $N_B = 160$.

(a) Trajectory (A).

(b) RMSE.
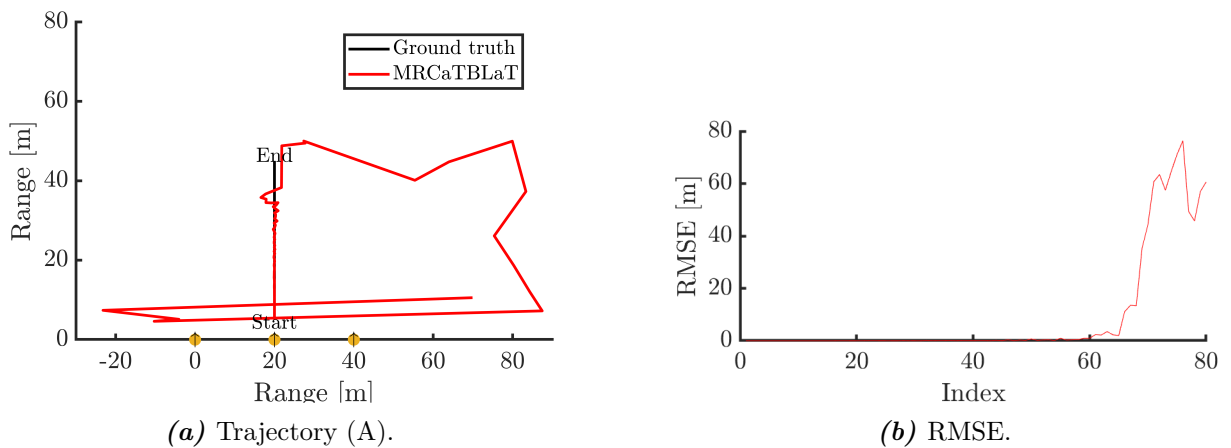
Figure 6.23. The performance on MRCaTBLaT using $N_B = 160$.

Discussion 7

The results we obtain from using the MRBLaT algorithm in the CF1T scenario are satisfactory as the ground truth and estimated tracks are similar as seen in Figure 6.4, where the RMSE of the estimations are given in Figure 6.5. The algorithm is then tested in the C1T scenario where it is no longer able to find the target as seen in Figure 6.10. Note that the RMSE shown in Figure 6.11 is not higher due to the bounds for the optimisation from (5.18).

The clutter tracking algorithm is evaluated using data from a single radar as the clutter field parameters are estimated locally. The results from this radar demonstrate how the algorithm performs. Using 80 basis functions, $\hat{\mathbf{\Gamma}}$ yields similar clutter fields and clutter signals as for $\mathbf{\Gamma}$. This is seen in Figure 6.12 and Figure 6.16. The $\hat{\mathbf{\Gamma}}$ and $\mathbf{\Gamma}$ are similar as shown in Figure 6.13 and Figure 6.14. Interestingly, $\mathbf{\Gamma}$ is estimated more precise when fewer basis functions are used, likely due to the reduced number of parameters. Note that the estimation also benefits from the clutter signal being generated using the same number of basis functions as used in the estimation process. Future work could explore how the estimation performs when applied to clutter signals generated with a significantly larger number of basis functions.

Separately, the MRBLaT algorithm and the clutter tracking algorithm both show good results, obtaining estimates close to the ground truth. The algorithms are combined to form the MRCaTBLaT algorithm. This algorithm is tested in the C1T scenario for three radars where the target parameters are estimated globally while the clutter parameters are estimated locally for each radar. Figure 6.21 shows that the combined algorithm estimates the ground truth positions almost perfectly. From Figure 6.22 the estimates are always within $0.05\,\mathrm{m}$ of the ground truth positions. Thus, the MRBLaT algorithm is actually improved by including clutter tracking.

Looking at Figure 6.19 and Figure 6.20, it is seen that the target signal is concealed by the clutter signal for radar 1 and 3, indicating that the MRCaTBLaT algorithm works in low SINR settings. Thus, the clutter tracking part of the MRCaTBLaT algorithm effectively removes the clutter signal such that the target is detected correctly. This property is indicated by Figure 6.16.

Due to time constraints, MRCaTBLaT has not been tested with varying numbers of basis functions. Initial results suggest that the number of basis functions should not be too high, as indicated in Figure 6.23. One possible reason is that the clutter field may include the target signal as a part of the estimate of $\mathbf{\Gamma}_n$. Thus, using fewer basis functions may lead to better performance in target tracking within cluttered environments.

Conclusion 8

In this project, we have developed and implemented a joint multiple radar clutter and target Bayesian localisation and tracking algorithm, MRCaTBLaT, in Cartesian coordinates with local clutter fields for each radar, with the ability to track a low RCS target in low SINR conditions. This was accomplished by deriving the signal model for a target signal and for clutter signals via random fields. Furthermore, the mean field theory was utilised in order to approximate the intractable distributions for the target and clutter signals.

The MRCaTMRBLaT algorithm was evaluated in a clutter environment with one target. We have evaluated the algorithm through simulations, where the simulated data was obtained by modelling a MIMO FMCW radar. The MRCaTBLaT algorithm has been evaluated for two different tracks, both in the low SINR environment. We have showed that the performance of the MRBLaT algorithm has been improved by including clutter tracking. This holds for the performance of MRBLaT in a clutter and clutter-free environment with one target.

8.1 Further Works
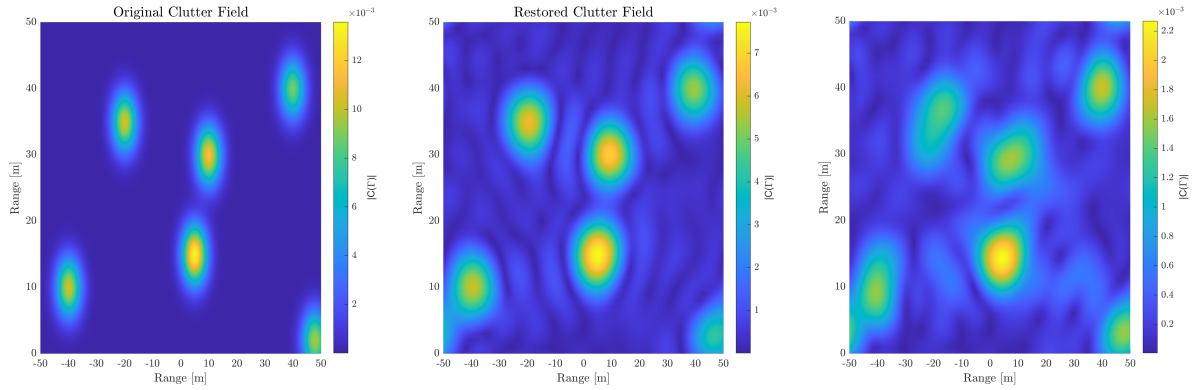
(a) The true clutter field based on 5151 basis functions. *(b)* A representation of the true clutter field using 80 basis functions. *(c)* The estimated clutter field based on $\widehat{\boldsymbol{\Gamma}}_{80}$.

Figure 8.1. Different representations of a clutter field.

An interesting extension of the current algorithm would include the ability to obtain a $\boldsymbol{Z}_{0:N}^{1:N_{\text{radar}}}$ from a clutter environment, and then be able to estimate the clutter field by using an initial $\boldsymbol{\Gamma}_0^{(k)}$ and then purely estimate all the parameters from this. The procedure would be

1. A clutter field is constructed
2. An initial $\boldsymbol{\Gamma}_{\text{init}}$ is found based on this clutter field and a complete basis is utilised.
3. From this complete basis, the signal $\boldsymbol{Z} = \boldsymbol{Z}_C + \boldsymbol{Z}_t + \boldsymbol{W}$ is generated.
4. Then a subset of $\boldsymbol{\Gamma}_{\text{init}}$ is chosen and a basis is chosen alongside it.
5. Based on this subset of $\boldsymbol{\Gamma}_{\text{init}}$, $\boldsymbol{M}$ is calculated.

6. $\boldsymbol{M}$ is then used along with $\boldsymbol{Z}$, which is based on the complete basis, to calculate $\hat{\boldsymbol{\Gamma}}_n$.

7. $\hat{\boldsymbol{\Gamma}}_n$ is then compared to $\boldsymbol{\Gamma}_{\text{init}}$, to evaluate the performance of the algorithm.

A bare-bone example of this procedure can be seen in Figure 8.1. Furthermore, it would be interesting to evaluate MRCaTBLaT on real-world data, as this would come with its own set of problems. One of these interesting problems, would be the placement of each radar, to help mitigate the interference between each individual radar, and also cover the most ground, with the least radars.

It would be interesting to have a case where the number of basis functions were equal to the number of samples in a signal. Then $\boldsymbol{M}$ would become a square matrix, which would allow for the use of the MATLAB function `inv`, instead of using the function `svds`, thus making it less computationally heavy and fast. This would be relevant, as the algorithm should run locally on smaller radars.

Bibliography

Adler, R. J. and Taylor, J. (2015). Applications of random fields and geometry foundations and case studies.

Barton, D. (1985). Land clutter models for radar design and analysis. *Proceedings of the IEEE*, 73(2):198–204.

Başar, E., Gölbaşı, B. T., Tülay, E., Aydın, S., and Başar-Eroğlu, C. (2016). Best method for analysis of brain oscillations in healthy subjects and neuropsychiatric diseases. *International Journal of Psychophysiology*, 103:22–42.

Bishop, C. M. (2006). *Pattern recognition and machine learning.* Springer.

Brooker, G. M. et al. (2005). Understanding millimetre wave fmcw radars. In *1st international Conference on Sensing Technology*, volume 1.

Capraro, C. T., Capraro, G. T., and Wicks, M. C. (2007). Knowledge aided detection and tracking. In *2007 IEEE Radar Conference*, pages 352–356. IEEE.

Døssing, S. (2025a). Mere end en tredobling: Antallet af ulovlige droneflyvninger nær lufthavne er eksploderet. *Ingeniøren.* Last visited: 03-03-2025.

Døssing, S. (2025b). Mystiske droner undrer ekspert: "For at være ærlig, ville jeg være bekymret". *Ingeniøren.* Last visited: 11-03-2025.

Grove, R. (2022). *MIMO radar Systems and Algorithms - Imperfections and Calibration.* PhD thesis, Technical University of Denmark.

Huang, D., Zhang, Z., Fang, X., He, M., Lai, H., and Mi, B. (2023). Stif: a spatial–temporal integrated framework for end-to-end micro-uav trajectory tracking and prediction with 4-d mimo radar. *IEEE Internet of Things Journal*, 10(21):18821–18836.

Hubbert, J., Dixon, M., Ellis, S., and Meymaris, G. (2009). Weather radar ground clutter. part i: Identification, modeling, and simulation. *Journal of Atmospheric and Oceanic Technology*, 26(7):1165–1180.

Jankiraman, M. (2018). *FMCW radar design.* Artech House.

Kingsley, N. and Guerci, J. R. (2022). *Radar RF Circuit Design.* Artech House.

Kingsley, S. and Quegan, S. (1992). *Understanding radar systems.* McGraw-Hill.

Kitchen, A. H. F., Brøndt, M. S. L., Jensen, M. S., Pedersen, T., and Westerkam, A. M. (2025). Distributed algorithm for cooperative joint localization and tracking using Multiple-Input Multiple-Output radars. In *2025 IEEE International Radar Conference (RADAR) (Radar 2025)*, page 6, Atlanta, USA.

Klauder, J. R., Price, A. C., Darlington, S., and Albersheim, W. J. (1960). The theory and design of chirp radars. *Bell System Technical Journal*, 39(4):745–808.

Li, B. and Chen, X. (2014). Wavelet-based numerical analysis: A review and classification. *Finite Elements in Analysis and Design*, 81:14–31.

Li, J. and Stoica, P. (2009). *MIMO radar signal processing.* John Wiley & Sons.

Lu, X., Liu, X., Zhang, Y., Li, Y., and Zuo, H. (2021). Simulation of airborne collision between a drone and an aircraft nose. *Aerospace Science and Technology*, 118:107078.

Musicki, D. and La Scala, B. (2008). Multi-target tracking in clutter without measurement assignment. *IEEE Transactions on Aerospace and Electronic Systems*, 44(3):877–896.

Niu, R., Blum, R. S., Varshney, P. K., and Drozd, A. L. (2012). Target localization and tracking in noncoherent multiple-input multiple-output radar systems. *IEEE Transactions on Aerospace and Electronic Systems*, 48(2):1466–1489.

Richards, M. A., Scheer, J., Holm, W. A., and Melvin, W. L. (2010). *Principles of Modern Radar.* SciTech Publishing.

Root, W. L. and Pitcher, T. S. (1955). On the fourier series expansion of random functions. *The Annals of mathematical statistics*, 26(2):313–318.

Sedivy, P. and Nemec, O. (2021). Drone rcs statistical behaviour. In *Proceedings of the MSG-SET-183 Specialists' Meeting on "Drone Detectability: Modelling the Relevant Signature", North Atlantic Treaty Organization (NATO), Held Virtually (via WebEx).*

Steer, M. (2019). *Microwave and RF design*, volume 4. NC State University, 3$^{\text{rd}}$ edition.

Thaysen, J. C. (2023). Der er masser af droner i Danmark, men ganske få uheld - og en helt masse regler. *Århus Stifttidende.* Last visited: 12-03-2025.

Trafikstyrelsen (2023a). *Nye vilkår for at flyve med droner efter 1. januar.* `https://www.trafikstyrelsen.dk/nyheder/2023/dec/nye-vilkaar-for-at-flyve-med-droner-efter-1-januar`. Last visited: 03-03-2025.

Trafikstyrelsen (2023b). *Overblik over dronereglerne.* `https://www.droneregler.dk/generelt-om-regler-for-droneflyvning/overblik-over-dronereglerne`. Last visited: 12-03-2025.

Westerkam, A. M., Manchón, C. N., Mogensen, P., and Pedersen, T. (2023). Bayesian joint localization and tracking algorithm using multiple-input multiple-output radar. In *2023 IEEE 9th International Workshop on Computational Advances in Multi-Sensor Adaptive Processing (CAMSAP)*, 2023 IEEE 9th International Workshop on Computational Advances in Multi-Sensor Adaptive Processing (CAMSAP). IEEE.

Westerkam, A. M., Möderl, J., Leitinger, E., and Pedersen, T. (2025). Variational message passing-based multiobject tracking for mimo-radars using raw sensor signals.

Westerkam, A. M. and Pedersen, T. (2025). Clutter tracking using variational message passing.

Witten, P. (2024). Farlig situation: Luftrummet lukket ved Aalborg Lufthavn. *Nordjyske.* Last visited: 11-03-2025.

Zepeda-Tello, R., Schomaker, M., Maringe, C., Smith, M. J., Belot, A., Rachet, B., Schnitzer, M. E., and Luque-Fernandez, M. A. (2022). The delta-method and influence function in medical statistics: a reproducible tutorial.

Zwanetski, A. and Rohling, H. (2012). Continuous wave mimo radar based on time division multiplexing. In *2012 13th International Radar Symposium*, pages 119–121. IEEE.

Øksendal, B. (2003). *Stochastic differential equations : an introduction with applications.* Universitext. Springer, Berlin, 6. ed. edition.

Random Fields

A

A.1 Properties of Random Fields

Kolmogorov's Extension Theorem is presented along with properties of orthonormal expansions of random fields.

> **Theorem A.1.1** (Kolmogorov's Extension Theorem)
> For all $t_1, \ldots, t_k \in T$, $k \in \mathbb{N}$ let $\nu_{t_1, \ldots, t_k}$ be probability measures on $\mathbb{R}^{nk}$ such that
>
> $$\nu_{t_{\sigma(1)}, \ldots, t_{\sigma(k)}}(F_1 \times \cdots \times F_k) = \nu_{t_1, \ldots, t_k}(F_{\sigma^{-1}(1)} \times \cdots \times F_\sigma^{-1}(k)) \tag{A.1}$$
>
> for all permutations σ on $\{1, 2, \ldots, k\}$ and
>
> $$\nu_{t_1, \ldots, t_k}(F_1 \times \cdots \times F_k) = \nu_{t_1, \ldots, t_k, t_{k+1}, \ldots, t_{k+m}}(F_1 \times \cdots F_k \times \mathbb{R}^n \times \cdots \times \mathbb{R}^n) \tag{A.2}$$
>
> for all $m \in \mathbb{N}$, where the set on the right hand side has a total of $k + m$ factors. Then there exists a probability space $(\Omega, \mathcal{F}, P)$ and stochastic process $\{f(t)\}$ on Ω, $f_t : \Omega \to \mathbb{R}^n$ such that
>
> $$\nu_{t_1, \ldots, t_k}(F_1 \times \cdots \times F_k) = P[f_{t_1} \in F_1, \cdots, f_{t_k} \in F_k], \tag{A.3}$$
>
> for all $t_i \in T$, $k \in \mathbb{N}$ and all Borel sets F_i.
>
> [Øksendal, 2003, Theorem 2.1.5]

Note that $\mathbb{R}^n$ is an n-dimensional euclidean space.

A.1.1 Orthonormal Expansions of Random Fields

Before presenting the properties, note that the order of summation and integration, as well as double summations, can be interchanged under the assumption of completeness of the basis and the additional assumption of finite energy. That is

$$\int_{\mathbb{R}^N} \sum_n^\infty \gamma^{(n)} \psi^{(n)}(\boldsymbol{z}) \, \mathrm{d}\boldsymbol{z} = \sum_n^\infty \int_{\mathbb{R}^N} \gamma^{(n)} \psi^{(n)}(\boldsymbol{z}) \, \mathrm{d}\boldsymbol{z}, \tag{A.4}$$

and

$$\sum_{n'}^\infty \sum_n^\infty \left(\gamma^{(n)}\right)^* \gamma^{(n')} \left(\psi^{(n)}\right)^*(\boldsymbol{z}) \psi^{(n')}(\boldsymbol{z}) = \sum_n^\infty \sum_{n'}^\infty \left(\gamma^{(n)}\right)^* \gamma^{(n')} \left(\psi^{(n)}\right)^*(\boldsymbol{z}) \psi^{(n')}(\boldsymbol{z}). \tag{A.5}$$

With this, the mean becomes

$$\mathbb{E}[C(\boldsymbol{z})] = \mathbb{E}\left[\sum_n^\infty \gamma^{(n)} \psi^{(n)}(\boldsymbol{z})\right] = \sum_n^\infty \mathbb{E}[\gamma^{(n)}] \psi^{(n)}(\boldsymbol{z}), \tag{A.6}$$

and variance

$$\text{Var}(C(\boldsymbol{z})) = \text{Var}\left(\sum_n^\infty \gamma^{(n)} \psi^{(n)}(\boldsymbol{z})\right) \tag{A.7}$$

$$= \sum_{n,n'}^\infty \text{Cov}\left(\gamma^{(n)}, \gamma^{(n')}\right) \psi^{(n)}(\boldsymbol{z}) \left(\psi^{(n')}\right)^*(\boldsymbol{z}) \tag{A.8}$$

$$= \sum_n^\infty \text{Var}\left(\gamma^{(n)}\right) \left|\psi^{(n)}(\boldsymbol{z})\right|^2 + \sum_{n \neq n'} \text{Cov}\left(\gamma^{(n)}, \gamma^{(n')}\right) \psi^{(n)}(\boldsymbol{z}) \left(\psi^{(n')}\right)^*(\boldsymbol{z}). \tag{A.9}$$

The orthogonal expansion in (3.34) has covariance function

$$\text{Cov}(C(\boldsymbol{z}_1), C(\boldsymbol{z}_2)) = \text{Cov}\left(\sum_n \gamma^{(n)} \psi^{(n)}(\boldsymbol{z}_1), \sum_{n'} \gamma^{(n)} \psi^{(n)}(\boldsymbol{z}_2)\right) \tag{A.10}$$

where $\boldsymbol{z}_1, \boldsymbol{z}_2 \in \mathbb{R}^N$. Using the bi-linearity of the covariance yields:

$$\text{Cov}(C(\boldsymbol{z}_1), C(\boldsymbol{z}_2)) = \sum_n^\infty \sum_{n'}^\infty \text{Cov}\left(\gamma^{(n)}, \gamma^{(n')}\right) \psi^{(n)}(\boldsymbol{z}_1) \left(\psi^{(n')}\right)^*(\boldsymbol{z}_2). \tag{A.11}$$

From this, the covariance of $C(\boldsymbol{z}_1)$ and $C(\boldsymbol{z}_2)$ depends on the covariance of the expansion coefficients.

The orthogonal expansion in (3.34) has autocorrelation function

$$R_C(\boldsymbol{z}_1, \boldsymbol{z}_2) = \mathbb{E}[C(\boldsymbol{z}_1) C^*(\boldsymbol{z}_2)] \tag{A.12}$$

$$= \sum_{n=1}^\infty \sum_{n'=1}^\infty \mathbb{E}\left[\gamma^{(n)} \left(\gamma^{(n')}\right)^*\right] \psi^{(n)}(\boldsymbol{z}_1) \left(\psi^{(n')}\right)^*(\boldsymbol{z}_2) \tag{A.13}$$

$$= \sum_{n=1}^\infty \sum_{n'=1}^\infty \left(\mathbb{E}\left[\gamma^{(n)}\right] \mathbb{E}\left[\left(\gamma^{(n')}\right)^*\right] + \text{Cov}\left(\gamma^{(n)}, \gamma^{(n')}\right)\right) \psi^{(n)}(\boldsymbol{z}_1) \left(\psi^{(n')}\right)^*(\boldsymbol{z}_2). \tag{A.14}$$

Note that, the covariance and autocorrelation function are equal if $\mathbb{E}[\gamma^{(n)}] = 0$ or $\mathbb{E}[\gamma^{(n')}] = 0$.

If the basis functions are orthonormal, this leads to

$$\int_{\mathbb{R}^N} |C(\boldsymbol{z})|^2 \, \mathrm{d}\boldsymbol{z} = \int \left|\sum_n^\infty \gamma^{(n)} \psi^{(n)}(\boldsymbol{z})\right|^2 \mathrm{d}\boldsymbol{z} \tag{A.15}$$

$$= \int \sum_n^\infty \sum_m^\infty \gamma^{(n)} \left(\gamma^{(m)}\right)^* \psi^{(n)}(\boldsymbol{z}) \left(\psi^{(m)}\right)^*(\boldsymbol{z}) \, \mathrm{d}\boldsymbol{z} \tag{A.16}$$

$$= \sum_n^\infty \sum_m^\infty \gamma^{(n)} \left(\gamma^{(m)}\right)^* \int_{\mathbb{R}^N} \psi^{(n)}(\boldsymbol{z}) \left(\psi^{(m)}\right)^*(\boldsymbol{z}) \, \mathrm{d}\boldsymbol{z} \tag{A.17}$$

$$= \sum_n^\infty \left|\gamma^{(n)}\right|^2. \tag{A.18}$$

Thus,

$$\mathbb{E}\left[\int_{\mathbb{R}^N} |C(\boldsymbol{z})|^2 \, \mathrm{d}\boldsymbol{z}\right] = \sum_n^\infty \mathbb{E}\left[\left|\gamma^{(n)}\right|^2\right]. \tag{A.19}$$

Derivation of Messages

B

B.1 Derivation of the Second and Third Message for the Target

Recall that the joint distribution for the network is given as

$$p(\boldsymbol{Z}_{0:N}, \boldsymbol{\phi}_{0:N}, \boldsymbol{\Gamma}_{0:N}, \boldsymbol{\Lambda}_a, \boldsymbol{\mu}_C, \boldsymbol{\Lambda}_C) = p(\boldsymbol{\phi}_0|\boldsymbol{\Lambda}_a)p(\boldsymbol{\Lambda}_a)\prod_{n=0}^{N}\left(\prod_{k=1}^{N_{\text{radar}}} p\left(\boldsymbol{Z}_n^{(k)}|\boldsymbol{\phi}_n, \boldsymbol{\Gamma}_n^{(k)}\right)\right)$$

$$\times \prod_{n'=1}^{N} p(\boldsymbol{\phi}_{n'}|\boldsymbol{\phi}_{n'-1}, \boldsymbol{\Lambda}_a)\left(\prod_{k'=1}^{N_{\text{radar}}} p\left(\boldsymbol{\Lambda}_C^{(k')}\right)p\left(\boldsymbol{\mu}_C^{(k')}\right)p\left(\boldsymbol{\Gamma}_0^{(k')}\Big|\boldsymbol{\mu}_C^{(k')}, \boldsymbol{\Lambda}_C^{(k')}\right)p\left(\boldsymbol{\Gamma}_{n'}^{(k')}\Big|\boldsymbol{\Gamma}_{n'-1}^{(k')}, \boldsymbol{\mu}_C^{k'}, \boldsymbol{\Lambda}_C^{k'}\right)\right). \tag{B.1}$$

Note that there will be some complications with $p(\boldsymbol{\phi}_0|\boldsymbol{\Lambda}_a)$, thus it is set to an improper distribution such that $p(\boldsymbol{\phi}_0|\boldsymbol{\Lambda}_a) = 1$. The messages for the target will now be derived. Assume linear motion for the target, which is described by the Markov chain

$$\boldsymbol{\phi}_n = \boldsymbol{T}\boldsymbol{\phi}_{n-1} + \boldsymbol{G}a, \quad a|\boldsymbol{\Lambda}_a \sim \mathcal{N}(a; \boldsymbol{0}, \boldsymbol{\Lambda}_a). \tag{B.2}$$

Here, $\boldsymbol{T}$ denotes the kinematic matrix in Cartesian coordinates, while $\boldsymbol{G}$ denotes the process noise matrix. They are given as

$$\boldsymbol{T} = \begin{bmatrix} 1 & 0 & \Delta t & 0 \\ 0 & 1 & 0 & \Delta t \\ 0 & 0 & 1 & 0 \\ 0 & 0 & 0 & 1 \end{bmatrix}, \quad \boldsymbol{G} = \begin{bmatrix} \frac{\Delta t^2}{2} & 0 & 0 & 0 \\ 0 & \frac{\Delta t^2}{2} & 0 & 0 \\ 0 & 0 & \Delta t & 0 \\ 0 & 0 & 0 & \Delta t \end{bmatrix}, \tag{B.3}$$

where Δt is the time interval between transmissions.

There are two surrogate functions related to the target:

$$\ln(q(\boldsymbol{\phi}_n)) = \sum_{k=1}^{N_{\text{radar}}}\left(\ln\left(p\left(\boldsymbol{Z}_n^{(k)}|\boldsymbol{\phi}_n\right)\right)\right) + \mathbb{E}_{\backslash\boldsymbol{\phi}_n}[\ln(p(\boldsymbol{\phi}_n|\boldsymbol{\phi}_{n-1}, \boldsymbol{\Lambda}_a))]$$

$$+ \mathbb{E}_{\backslash\boldsymbol{\phi}_n}[\ln(p(\boldsymbol{\phi}_{n+1}|\boldsymbol{\phi}_n, \boldsymbol{\Lambda}_a))] + \text{constant} \tag{B.4}$$

$$\ln(q(\boldsymbol{\Lambda}_a)) = \sum_{n=1}^{N}\mathbb{E}_{\backslash\boldsymbol{\Lambda}_a}[\ln(p(\boldsymbol{\phi}_n|\boldsymbol{\phi}_{n-1}, \boldsymbol{\Lambda}_a))] + \ln(p(\boldsymbol{\Lambda}_a)) + \text{constant}. \tag{B.5}$$

First (B.4) is examined, where the first term is calculated in Section 4.2.2. Thus the second term is looked upon. Note that $\boldsymbol{\phi}_n|\boldsymbol{\phi}_{n-1}, \boldsymbol{\Lambda}_a$ is Gaussian, meaning

$$\boldsymbol{\phi}_n|\boldsymbol{\phi}_{n-1}, \boldsymbol{\mu}_a, \boldsymbol{\Lambda}_a \sim \mathcal{N}\left(\boldsymbol{T}\boldsymbol{\phi}_{n-1} + \boldsymbol{G}\boldsymbol{\mu}_a, (\boldsymbol{G}^\top\boldsymbol{\Lambda}_a^{-1}\boldsymbol{G})^{-1}\right) = p(\boldsymbol{\phi}_n|\boldsymbol{\phi}_{n-1}, \boldsymbol{\mu}_a, \boldsymbol{\Lambda}_a). \tag{B.6}$$

Thus, the natural logarithm of the probability density function is written as

$$\ln(p(\boldsymbol{\phi}_n|\boldsymbol{\phi}_{n-1}, \boldsymbol{\mu}_a, \boldsymbol{\Lambda}_a)) \tag{B.7}$$

$$= \ln\left(\frac{\sqrt{\det(\boldsymbol{\Lambda}_a)}}{2\pi} \exp\left(-\frac{1}{2}(\boldsymbol{\phi}_n - \boldsymbol{T}\boldsymbol{\phi}_{n-1} - \boldsymbol{G}\boldsymbol{\mu}_a)^\top \left(\boldsymbol{G}^\top \boldsymbol{\Lambda}_a^{-1} \boldsymbol{G}\right)^{-1} (\boldsymbol{\phi}_n - \boldsymbol{T}\boldsymbol{\phi}_{n-1} - \boldsymbol{G}\boldsymbol{\mu}_a)\right)\right) \tag{B.8}$$

$$\propto -(\boldsymbol{\phi}_n - \boldsymbol{T}\boldsymbol{\phi}_{n-1} - \boldsymbol{G}\boldsymbol{\mu}_a)^\top \underbrace{\left(\boldsymbol{G}^\top \boldsymbol{\Lambda}_a^{-1} \boldsymbol{G}\right)^{-1}}_{\widetilde{\boldsymbol{\Lambda}}} (\boldsymbol{\phi}_n - \boldsymbol{T}\boldsymbol{\phi}_{n-1} - \boldsymbol{G}\boldsymbol{\mu}_a) + \text{constant}(\boldsymbol{\Lambda}_a). \tag{B.9}$$

By letting $\boldsymbol{\eta} = \boldsymbol{\phi}_n - \boldsymbol{G}\boldsymbol{\mu}_a$, the expression becomes

$$\ln(p(\boldsymbol{\phi}_n|\boldsymbol{\phi}_{n-1}, \boldsymbol{\mu}_a, \boldsymbol{\Lambda}_a)) \tag{B.10}$$

$$\propto -(\boldsymbol{\eta} - \boldsymbol{T}\boldsymbol{\phi}_{n-1})^\top \widetilde{\boldsymbol{\Lambda}}(\boldsymbol{\eta} - \boldsymbol{T}\boldsymbol{\phi}_{n-1}) + \text{constant}(\boldsymbol{\Lambda}_a) \tag{B.11}$$

$$= -(\boldsymbol{T}^{-1}\boldsymbol{\eta} - \boldsymbol{\phi}_{n-1})^\top \underbrace{\boldsymbol{T}^\top \tilde{\boldsymbol{\Lambda}} \boldsymbol{T}}_{\check{\boldsymbol{\Lambda}}} (\boldsymbol{T}^{-1}\boldsymbol{\eta} - \boldsymbol{\phi}_{n-1}) + \text{constant}(\boldsymbol{\Lambda}_a) \tag{B.12}$$

$$= -(\boldsymbol{T}^{-1}\boldsymbol{\eta})^\top \check{\boldsymbol{\Lambda}} \boldsymbol{T}^{-1}\boldsymbol{\eta} + (\boldsymbol{T}^{-1}\boldsymbol{\eta})^\top \check{\boldsymbol{\Lambda}} \boldsymbol{\phi}_{n-1} + \boldsymbol{\phi}_{n-1}^\top \check{\boldsymbol{\Lambda}} \boldsymbol{T}^{-1}\boldsymbol{\eta} - \boldsymbol{\phi}_{n-1}^\top \check{\boldsymbol{\Lambda}} \boldsymbol{\phi}_{n-1} + \text{constant}(\boldsymbol{\Lambda}_a). \tag{B.13}$$

The expectation is taken on both sides of (B.13) with respect to $\boldsymbol{\phi}_{n-1}$:

$$\mathop{\mathbb{E}}_{\boldsymbol{\phi}_{n-1}}\left[\ln(p(\boldsymbol{\phi}_n|\boldsymbol{\phi}_{n-1}, \boldsymbol{\mu}_a, \boldsymbol{\Lambda}_a))\right] \tag{B.14}$$

$$\propto \mathop{\mathbb{E}}_{\boldsymbol{\phi}_{n-1}}\left[-(\boldsymbol{T}^{-1}\boldsymbol{\eta})^\top \check{\boldsymbol{\Lambda}} \boldsymbol{T}^{-1}\boldsymbol{\eta} + (\boldsymbol{T}^{-1}\boldsymbol{\eta})^\top \check{\boldsymbol{\Lambda}} \boldsymbol{\phi}_{n-1} + \boldsymbol{\phi}_{n-1}^\top \check{\boldsymbol{\Lambda}} \boldsymbol{T}^{-1}\boldsymbol{\eta} - \boldsymbol{\phi}_{n-1}^\top \check{\boldsymbol{\Lambda}} \boldsymbol{\phi}_{n-1}\right] + \text{constant}(\boldsymbol{\Lambda}_a) \tag{B.15}$$

$$= -(\boldsymbol{T}^{-1}\boldsymbol{\eta})^\top \check{\boldsymbol{\Lambda}} \boldsymbol{T}^{-1}\boldsymbol{\eta} + (\boldsymbol{T}^{-1}\boldsymbol{\eta})^\top \check{\boldsymbol{\Lambda}} \mathop{\mathbb{E}}_{\boldsymbol{\phi}_{n-1}}[\boldsymbol{\phi}_{n-1}] + \mathop{\mathbb{E}}_{\boldsymbol{\phi}_{n-1}}\left[\boldsymbol{\phi}_{n-1}^\top\right] \check{\boldsymbol{\Lambda}} \boldsymbol{T}^{-1}\boldsymbol{\eta} + \text{constant}(\boldsymbol{\Lambda}_a), \tag{B.16}$$

since $\mathop{\mathbb{E}}_{\boldsymbol{\phi}_{n-1}}[\boldsymbol{\phi}_{n-1}^\top \check{\boldsymbol{\Lambda}} \boldsymbol{\phi}_{n-1}] = \text{constant}$. By denoting $\mathop{\mathbb{E}}_{\boldsymbol{\phi}_{n-1}}[\boldsymbol{\phi}_{n-1}] = \boldsymbol{\mu}_{\boldsymbol{\phi}_{n-1}}$, (B.16) is written as

$$\mathop{\mathbb{E}}_{\boldsymbol{\phi}_{n-1}}\left[\ln(p(\boldsymbol{\phi}_n|\boldsymbol{\phi}_{n-1}, \boldsymbol{\mu}_a, \boldsymbol{\Lambda}_a))\right] \tag{B.17}$$

$$\propto -\left(\boldsymbol{T}^{-1}\boldsymbol{\eta}\right)^\top \check{\boldsymbol{\Lambda}} \boldsymbol{T}^{-1}\boldsymbol{\eta} + \left(\boldsymbol{T}^{-1}\boldsymbol{\eta}\right)^\top \check{\boldsymbol{\Lambda}} \boldsymbol{\mu}_{\boldsymbol{\phi}_{n-1}} + \boldsymbol{\mu}_{\boldsymbol{\phi}_{n-1}}^\top \check{\boldsymbol{\Lambda}} \boldsymbol{T}^{-1}\boldsymbol{\eta} + \text{constant}(\boldsymbol{\Lambda}_a) \tag{B.18}$$

$$= -\left(\boldsymbol{T}^{-1}\boldsymbol{\eta} - \boldsymbol{\mu}_{\boldsymbol{\phi}_{n-1}}\right)^\top \check{\boldsymbol{\Lambda}} \left(\boldsymbol{T}^{-1}\boldsymbol{\eta} - \boldsymbol{\mu}_{\boldsymbol{\phi}_{n-1}}\right) + \text{constant}(\boldsymbol{\Lambda}_a) \tag{B.19}$$

$$= -\left(\boldsymbol{\eta} - \boldsymbol{T}\boldsymbol{\mu}_{\boldsymbol{\phi}_{n-1}}\right)^\top \widetilde{\boldsymbol{\Lambda}}\left(\boldsymbol{\eta} - \boldsymbol{T}\boldsymbol{\mu}_{\boldsymbol{\phi}_{n-1}}\right) + \text{constant}(\boldsymbol{\Lambda}_a) \tag{B.20}$$

$$= -\left(\boldsymbol{\phi}_n - \boldsymbol{T}\boldsymbol{\mu}_{\boldsymbol{\phi}_{n-1}} - \boldsymbol{G}\boldsymbol{\mu}_a\right)^\top \widetilde{\boldsymbol{\Lambda}}\left(\boldsymbol{\phi}_n - \boldsymbol{T}\boldsymbol{\mu}_{\boldsymbol{\phi}_{n-1}} - \boldsymbol{G}\boldsymbol{\mu}_a\right) + \text{constant}(\boldsymbol{\Lambda}_a) \tag{B.21}$$

Here, the first term is recognised as the exponent in a multivariate normal distribution in $\boldsymbol{\phi}_n$ with mean $\boldsymbol{T}\boldsymbol{\mu}_{\boldsymbol{\phi}_{n-1}} + \boldsymbol{G}\boldsymbol{\mu}_a$ and precision matrix $\widetilde{\boldsymbol{\Lambda}} = (\boldsymbol{G}^\top \boldsymbol{\Lambda}_a^{-1} \boldsymbol{G})^{-1}$. Thus the message is

$$\varepsilon^{(\boldsymbol{\phi}_{n-1} \to \boldsymbol{\phi}_n)} = \mathcal{N}^C\left(\overline{\varepsilon}^{(\boldsymbol{\phi}_{n-1} \to \boldsymbol{\phi}_n)}, \overline{\overline{\varepsilon}}^{(\boldsymbol{\phi}_{n-1} \to \boldsymbol{\phi}_n)}\right), \tag{B.22}$$

where

$$\overline{\varepsilon}^{(\boldsymbol{\phi}_{n-1} \to \boldsymbol{\phi}_n)} = \boldsymbol{T}\boldsymbol{\mu}_{\boldsymbol{\phi}_{n-1}} + \boldsymbol{G}\boldsymbol{\mu}_a, \tag{B.23}$$

$$\overline{\overline{\varepsilon}}^{(\boldsymbol{\phi}_{n-1} \to \boldsymbol{\phi}_n)} = \left(\boldsymbol{G}^\top \boldsymbol{\Lambda}_a^{-1} \boldsymbol{G}\right)^{-1}. \tag{B.24}$$

The same is done for the message $\varepsilon^{(\phi_{n+1} \to \phi_n)}$, thus

$$\varepsilon^{(\phi_{n+1} \to \phi_n)} = \mathcal{N}^C\big(\overline{\varepsilon}^{(\phi_{n+1} \to \phi_n)}, \overline{\overline{\varepsilon}}^{(\phi_{n+1} \to \phi_n)}\big), \tag{B.25}$$

where

$$\overline{\varepsilon}^{(\phi_{n+1} \to \phi_n)} = \boldsymbol{T}\boldsymbol{\mu}_{\phi_{n-1}} + \boldsymbol{G}\boldsymbol{\mu_a}, \tag{B.26}$$

$$\overline{\overline{\varepsilon}}^{(\phi_{n+1} \to \phi_n)} = \big(\boldsymbol{G}^\top \boldsymbol{\Lambda_a}^{-1} \boldsymbol{G}\big)^{-1}. \tag{B.27}$$

B.2 Derivation of Expectations using the Delta Method

First, $\boldsymbol{S}_n(\boldsymbol{\phi}_n)$ is approximated by a first-order Taylor expansion around $\overline{\boldsymbol{\phi}}_n$ such that

$$\boldsymbol{S}_n(\boldsymbol{\phi}_n) \approx \boldsymbol{S}_n(\overline{\boldsymbol{\phi}}_n) + \frac{\mathrm{d}\boldsymbol{S}_n(\overline{\boldsymbol{\phi}}_n)}{\mathrm{d}\boldsymbol{\phi}_n}(\boldsymbol{\phi}_n - \overline{\boldsymbol{\phi}}_n), \tag{B.28}$$

where $\boldsymbol{\phi}_n$ follows a distribution with mean $\overline{\boldsymbol{\phi}}$ and covariance $\overline{\overline{\boldsymbol{\phi}}}$. Taking the expectation of (B.28) yields

$$\mathbb{E}_{\boldsymbol{\phi}_n}[\boldsymbol{S}_n(\boldsymbol{\phi}_n)] \approx \boldsymbol{S}_n(\overline{\boldsymbol{\phi}}_n) + \frac{\mathrm{d}\boldsymbol{S}_n(\overline{\boldsymbol{\phi}}_n)}{\mathrm{d}\boldsymbol{\phi}_n}\underbrace{\Big(\mathbb{E}_{\boldsymbol{\phi}_n}[\boldsymbol{\phi}_n] - \overline{\boldsymbol{\phi}}_n\Big)}_{=0} = \boldsymbol{S}_n(\overline{\boldsymbol{\phi}}_n). \tag{B.29}$$

Thus,

$$\mathbb{E}_{\boldsymbol{\phi}_n}\Big[\boldsymbol{S}_n(\boldsymbol{\phi}_n)\boldsymbol{S}_n(\boldsymbol{\phi}_n)^\dagger\Big]$$

$$\approx \mathbb{E}_{\boldsymbol{\phi}_n}\left[\left(\boldsymbol{S}_n(\overline{\boldsymbol{\phi}}_n) + \frac{\mathrm{d}\boldsymbol{S}_n(\overline{\boldsymbol{\phi}}_n)}{\mathrm{d}\boldsymbol{\phi}_n}(\boldsymbol{\phi}_n - \overline{\boldsymbol{\phi}}_n)\right)\left(\big(\boldsymbol{S}_n(\overline{\boldsymbol{\phi}}_n) + \frac{\mathrm{d}\boldsymbol{S}_n(\overline{\boldsymbol{\phi}}_n)}{\mathrm{d}\boldsymbol{\phi}_n}(\boldsymbol{\phi}_n - \overline{\boldsymbol{\phi}}_n)\big)^\dagger\right)\right] \tag{B.30}$$

$$\approx \boldsymbol{S}_n(\overline{\boldsymbol{\phi}}_n)\boldsymbol{S}_n(\overline{\boldsymbol{\phi}}_n)^\dagger + \frac{\mathrm{d}\boldsymbol{S}_n(\overline{\boldsymbol{\phi}}_n)}{\mathrm{d}\boldsymbol{\phi}_n}\underbrace{\Big(\mathbb{E}_{\boldsymbol{\phi}_n}[\boldsymbol{\phi}_n] - \overline{\boldsymbol{\phi}}_n\Big)}_{=0}\boldsymbol{S}_n(\overline{\boldsymbol{\phi}}_n)^\dagger$$

$$+ \boldsymbol{S}_n(\overline{\boldsymbol{\phi}}_n)\frac{\mathrm{d}\boldsymbol{S}_n(\overline{\boldsymbol{\phi}}_n)}{\mathrm{d}\boldsymbol{\phi}_n}\underbrace{\Big(\mathbb{E}_{\boldsymbol{\phi}_n}[\boldsymbol{\phi}_n] - \overline{\boldsymbol{\phi}}_n\Big)}_{=0} + \mathbb{E}_{\boldsymbol{\phi}_n}\left[\frac{\mathrm{d}\boldsymbol{S}_n(\overline{\boldsymbol{\phi}}_n)}{\mathrm{d}\boldsymbol{\phi}_n}(\boldsymbol{\phi}_n - \overline{\boldsymbol{\phi}}_n)(\boldsymbol{\phi}_n - \overline{\boldsymbol{\phi}}_n)^\dagger\frac{\mathrm{d}\boldsymbol{S}_n(\overline{\boldsymbol{\phi}}_n)}{\mathrm{d}\boldsymbol{\phi}_n}^\dagger\right]. \tag{B.31}$$

The last term in (B.31) is rewritten as

$$\mathbb{E}_{\boldsymbol{\phi}_n}\left[\frac{\mathrm{d}\boldsymbol{S}_n(\overline{\boldsymbol{\phi}}_n)}{\mathrm{d}\boldsymbol{\phi}_n}(\boldsymbol{\phi}_n - \overline{\boldsymbol{\phi}}_n)(\boldsymbol{\phi}_n - \overline{\boldsymbol{\phi}}_n)^\dagger\frac{\mathrm{d}\boldsymbol{S}_n(\overline{\boldsymbol{\phi}}_n)}{\mathrm{d}\boldsymbol{\phi}_n}^\dagger\right] = \frac{\mathrm{d}\boldsymbol{S}_n(\overline{\boldsymbol{\phi}}_n)}{\mathrm{d}\boldsymbol{\phi}_n}\underbrace{\mathbb{E}_{\boldsymbol{\phi}_n}\Big[(\boldsymbol{\phi}_n - \overline{\boldsymbol{\phi}}_n)(\boldsymbol{\phi}_n - \overline{\boldsymbol{\phi}}_n)^\dagger\Big]}_{\overline{\overline{\boldsymbol{\phi}}}_n}\frac{\mathrm{d}\boldsymbol{S}_n(\overline{\boldsymbol{\phi}}_n)}{\mathrm{d}\boldsymbol{\phi}_n}^\dagger \tag{B.32}$$

$$= \frac{\mathrm{d}\boldsymbol{S}_n(\overline{\boldsymbol{\phi}}_n)}{\mathrm{d}\boldsymbol{\phi}_n}\overline{\overline{\boldsymbol{\phi}}}_n\frac{\mathrm{d}\boldsymbol{S}_n(\overline{\boldsymbol{\phi}}_n)}{\mathrm{d}\boldsymbol{\phi}_n}^\dagger \tag{B.33}$$

$$= \nabla_{\boldsymbol{\phi}_n}\boldsymbol{S}_n(\overline{\boldsymbol{\phi}}_n)\overline{\overline{\boldsymbol{\phi}}}_n\nabla_{\boldsymbol{\phi}_n}\boldsymbol{S}_n(\overline{\boldsymbol{\phi}}_n)^\dagger, \tag{B.34}$$

where $\nabla_{\boldsymbol{\phi}_n}\boldsymbol{S}_n(\overline{\boldsymbol{\phi}}_n)$ is the Jacobian of $\boldsymbol{S}_n$ evaluated in $\overline{\boldsymbol{\phi}}_n$. Inserting (B.34) into (B.31) then yields

$$\mathbb{E}_{\boldsymbol{\phi}_n}\Big[\boldsymbol{S}_n(\boldsymbol{\phi}_n)\boldsymbol{S}_n(\boldsymbol{\phi}_n)^\dagger\Big] \approx \boldsymbol{S}_n(\overline{\boldsymbol{\phi}}_n)\boldsymbol{S}_n(\overline{\boldsymbol{\phi}}_n)^\dagger + \nabla_{\boldsymbol{\phi}_n}\boldsymbol{S}_n(\overline{\boldsymbol{\phi}}_n)\overline{\overline{\boldsymbol{\phi}}}_n\nabla_{\boldsymbol{\phi}_n}\boldsymbol{S}_n(\overline{\boldsymbol{\phi}}_n)^\dagger. \tag{B.35}$$

Results used for Implementation of the Signal Model

<div style="text-align: right">C</div>

C.1   Rewriting a Geometric Series

It is known that a finite geometric series can be written as

$$\sum_{h=0}^{N_s-1} \chi^h = \frac{1-\chi^{N_s}}{1-\chi}. \tag{C.1}$$

By multiplying (C.1) with 1, it can be written as

$$\sum_{h=0}^{N_s-1} \chi^h = \frac{1-\chi^{N_s}}{1-\chi} \cdot \frac{\chi^{-\frac{1}{2}}}{\chi^{-\frac{1}{2}}} \tag{C.2}$$

$$= \frac{\chi^{-\frac{1}{2}} - \chi^{N_s-\frac{1}{2}}}{\chi^{-\frac{1}{2}} - \chi^{\frac{1}{2}}} \tag{C.3}$$

$$= \frac{\chi^{-\frac{1}{2}} - \chi^{\frac{2N_s-1}{2}}}{\chi^{-\frac{1}{2}} - \chi^{\frac{1}{2}}} \tag{C.4}$$

$$= \chi^{\frac{N_s-1}{2}} \frac{\chi^{-\frac{N_s}{2}} - \chi^{\frac{N_s}{2}}}{\chi^{-\frac{1}{2}} - \chi^{\frac{1}{2}}}. \tag{C.5}$$

Using $\chi = \mathrm{e}^{i\nu}$, (C.5) becomes

$$\sum_{h=0}^{N_s-1} \mathrm{e}^{i\nu h} = \mathrm{e}^{\frac{i\nu(N_s-1)}{2}} \frac{\mathrm{e}^{-\frac{i\nu N_s}{2}} - \mathrm{e}^{\frac{i\nu N_s}{2}}}{\mathrm{e}^{-\frac{i\nu}{2}} - \mathrm{e}^{\frac{i\nu}{2}}}. \tag{C.6}$$

Applying Euler's formula then yields

$$\sum_{h=0}^{N_s-1} \mathrm{e}^{i\nu h} = \mathrm{e}^{i(N_s-1)\frac{\nu}{2}} \frac{\sin\left(\frac{N_s\nu}{2}\right)}{\sin\left(\frac{\nu}{2}\right)}. \tag{C.7}$$

C.2   Structure of $M^{(k)}$

All the $N_T N_R N_s$ vectors $\boldsymbol{B}^{(m,j,k)}[h'] = \mathcal{F}_{h\to h'}\{(\boldsymbol{\beta}^{(m,j,k)})^*[h]\} \in \mathbb{C}^{N_B}$ are organised in $\boldsymbol{M}^{(k)}$ in the following way

$$\boldsymbol{M}^{(k)} = \begin{bmatrix} B_1^{(1,1,k)}[1] & B_2^{(1,1,k)}[1] & \cdots & B_{N_B}^{(1,1,k)}[1] \\ B_1^{(1,1,k)}[2] & B_2^{(1,1,k)}[2] & \cdots & B_{N_B}^{(1,1,k)}[2] \\ \vdots & & & \\ B_1^{(1,1,k)}[N_s] & B_2^{(1,1,k)}[N_s] & \cdots & B_{N_B}^{(1,1,k)}[N_s] \\ B_1^{(2,1,k)}[1] & B_2^{(2,1,k)}[1] & \cdots & B_{N_B}^{(2,1,k)}[1] \\ B_1^{(2,1,k)}[2] & B_2^{(2,1,k)}[2] & \cdots & B_{N_B}^{(2,1,k)}[2] \\ \vdots & & & \\ B_1^{(2,1,k)}[N_s] & B_2^{(2,1,k)}[N_s] & \cdots & B_{N_B}^{(2,1,k)}[N_s] \\ \vdots & & & \\ B_1^{(N_T,1,k)}[1] & B_2^{(N_T,1,k)}[1] & \cdots & B_{N_B}^{(N_T,1,k)}[1] \\ B_1^{(N_T,1,k)}[2] & B_2^{(N_T,1,k)}[2] & \cdots & B_{N_B}^{(N_T,1,k)}[2] \\ \vdots & & & \\ B_1^{(N_T,1,k)}[N_s] & B_2^{(N_T,1,k)}[N_s] & \cdots & B_{N_B}^{(N_T,1,k)}[N_s] \\ B_1^{(1,2,k)}[1] & B_2^{(1,2,k)}[1] & \cdots & B_{N_B}^{(1,2,k)}[1] \\ B_1^{(1,2,k)}[2] & B_2^{(1,2,k)}[2] & \cdots & B_{N_B}^{(1,2,k)}[2] \\ \vdots & & & \\ B_1^{(1,2,k)}[N_s] & B_2^{(1,2,k)}[N_s] & \cdots & B_{N_B}^{(1,2,k)}[N_s] \\ \vdots & & & \\ B_1^{(N_T,N_R,k)}[N_s] & B_2^{(N_T,N_R,k)}[N_s] & \cdots & B_{N_B}^{(N_T,N_R,k)}[N_s] \end{bmatrix}. \tag{C.8}$$

Additional Results D
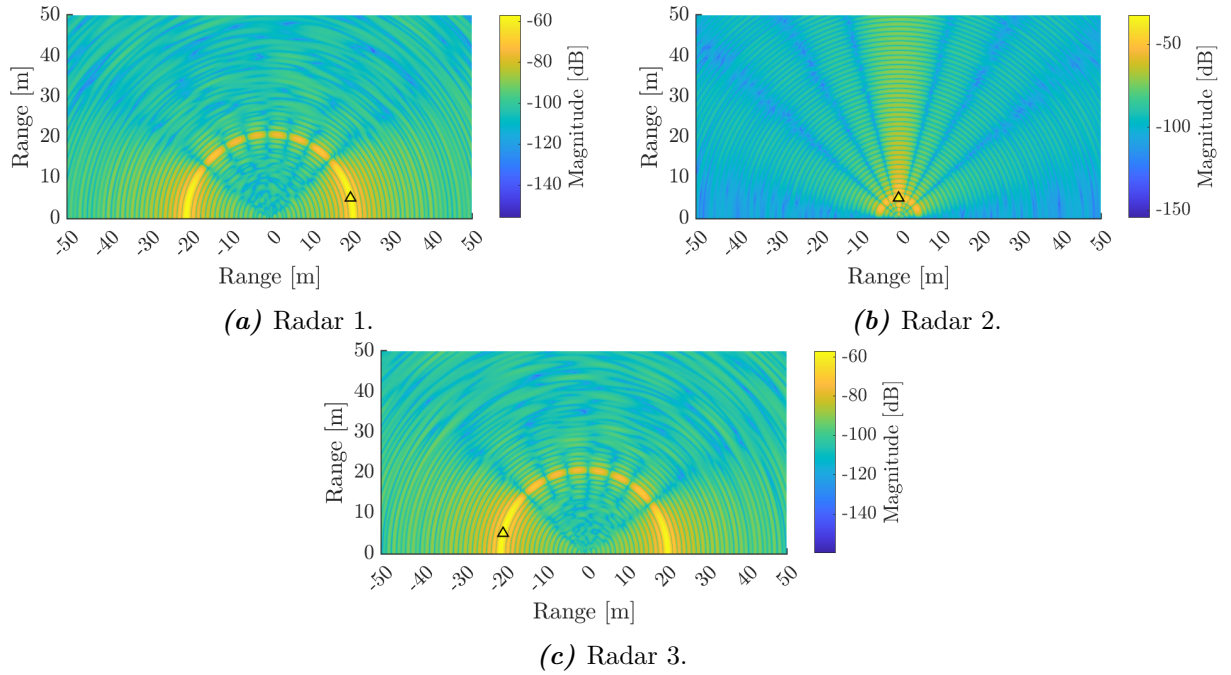
D.1   Multiple Radar Bayesian Localisation and Tracking

(a) Radar 1.

(b) Radar 2.

(c) Radar 3.

Figure D.1. $\left| S(\phi_1)^\dagger Z_1^{(k)} \right|$ where ϕ_1 is varied across a grid. Target is at $[20\ 5]^\top$m. The ground truth position is marked with a triangle.
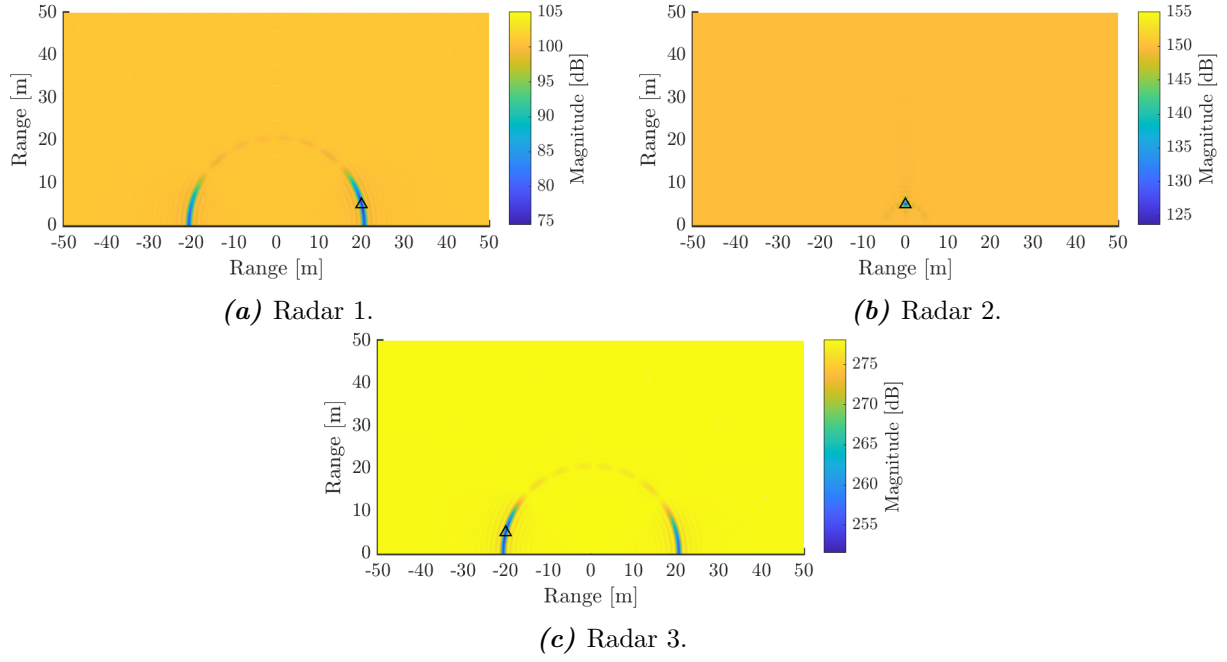
(a) Radar 1.

(b) Radar 2.

(c) Radar 3.

Figure D.2. Illustration of the KL divergence in (4.50) with respect to the mean. The target is at $[20\ 5]^{\top}$m. The ground truth position is marked with a triangle.
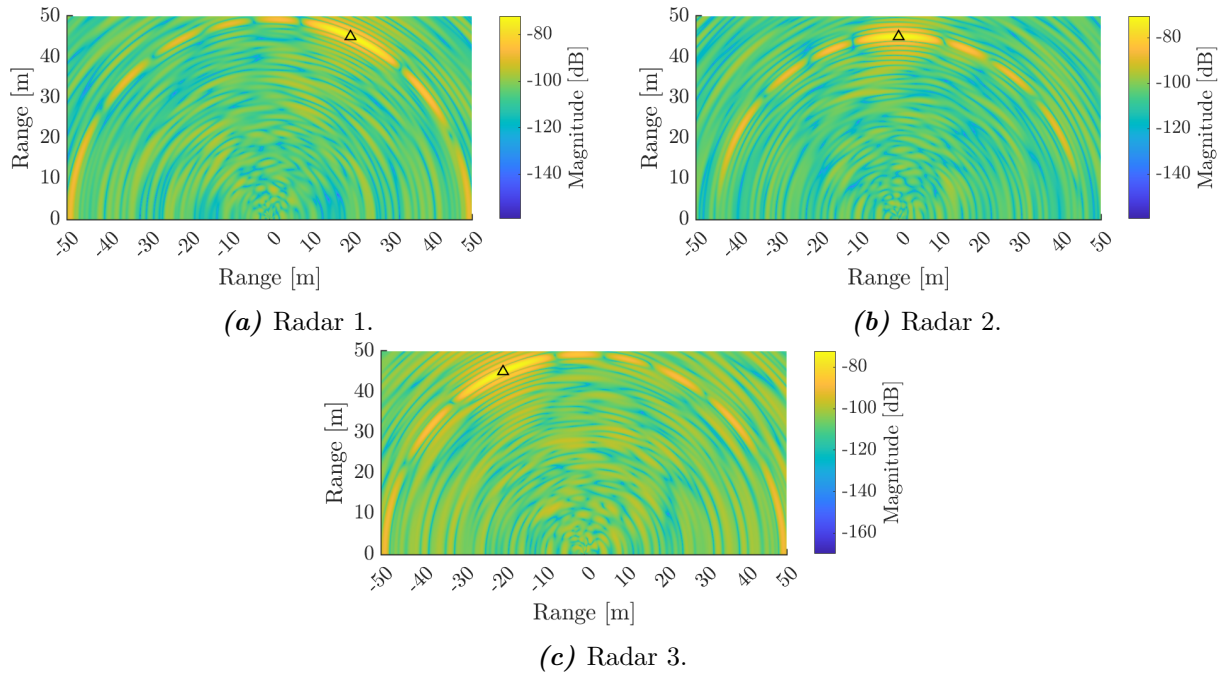

(a) Radar 1.

(b) Radar 2.

(c) Radar 3.

Figure D.3. $\left| S(\phi_1)^{\dagger} \boldsymbol{Z}_{80}^{(k)} \right|$ where ϕ_1 is varied across a grid. Target is at $[20\ 45]^{\top}$m. The ground truth position is marked with a triangle.

(a) Radar 1.
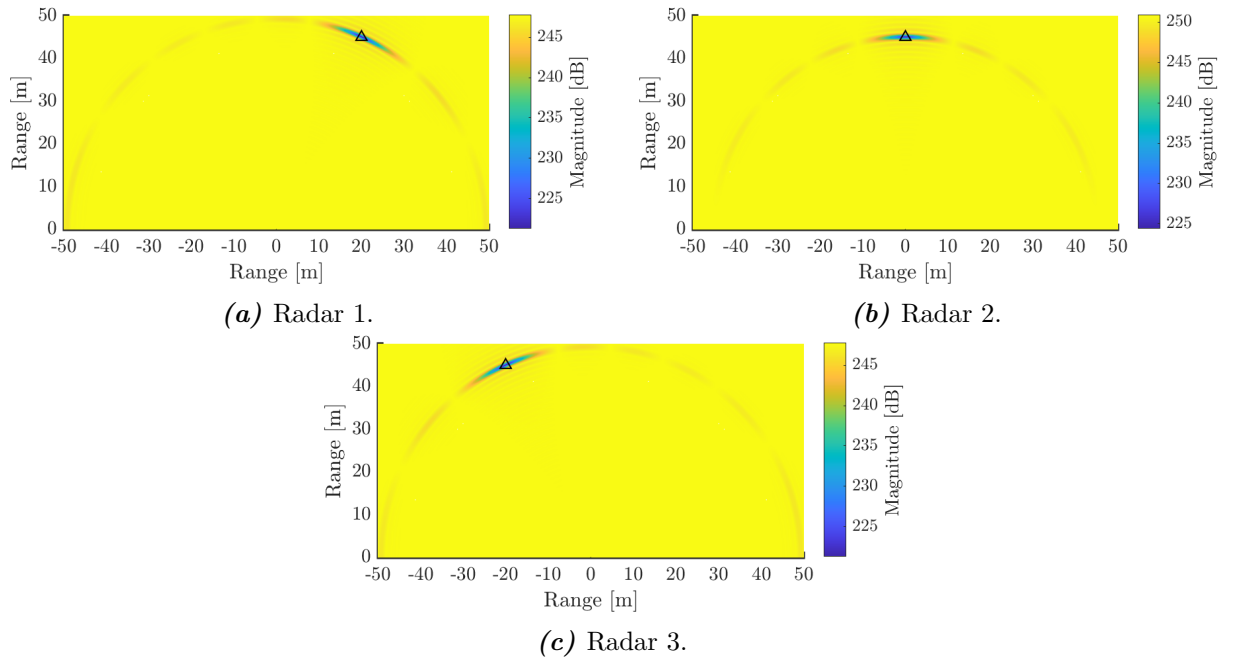

(b) Radar 2.

(c) Radar 3.

Figure D.4. Illustration of the KL divergence in (4.50) with respect to the mean. The target is at $[20\ 45]^\top$ m. The ground truth position is marked with a triangle.